INFLUENCE OF VARYING WIND SPEEDS, INSTALLATION HEIGHTS, ORIENTATION AND TILT ANGLES ON SOLAR PV MODULES AND DESIGN OF AUTOMATED PV SURFACE CLEANING SYSTEM

MARTIN NDETO PAUL

DOCTOR OF PHILOSOPHY

(Energy Technology)

JOMO KENYATTA UNIVERSITY

OF

AGRICULTURE AND TECHNOLOGY

2024

Influence of Varying Wind Speeds, Installation Heights, Orientation and Tilt Angles on Solar PV Modules and Design of Automated PV Surface Cleaning System

Martin Ndeto Paul

A Thesis Submitted in Partial Fulfillment of the Requirements for the Degree of Doctor of Philosophy in Energy Technology of the Jomo Kenyatta University of Agriculture and Technology

2024

DECLARATION

This thesis is my original work and has not been presented for a degree in any other university.

Signature: …… Date: ……

Martin Ndeto Paul

This thesis has been submitted for examination with our approval as University Supervisors:

Signature: ……. Date: ……...

Prof. Robert Kinyua, PhD

JKUAT, Kenya

Signature: ……. Date: ……...

Dr. David Wekesa, PhD

Multimedia University, Kenya

Signature: ……. Date: ……...

Dr. Francis Njoka, PhD

Kenyatta University, Kenya

DEDICATION

This study is dedicated to my spouse Gladys, daughter Quinn, son Ian and family members Richard, Maureen and Japheth.

ACKNOWLEDGEMENT

First, my gratitude goes to Jomo Kenyatta University of Agriculture and Technology for offering me a vacancy to undertake the Doctorate degree. My sincere appreciation also goes to my supervisors Prof. Robert Kinyua, Department of Physics, Jomo Kenyatta University of Agriculture and Technology, Dr. David Wekesa, Department of Physics, Multimedia University of Kenya and Dr. Francis Njoka, Department of Energy, Gas & Petroleum Engineering, Kenyatta University (KU) for research guidance and support through corrections and giving useful pieces of advice with the aim of making this study complete.

Secondly, I am also grateful to Jomo Kenyatta University of Agriculture and Technology (JKUAT) Physics laboratory, Multimedia University of Kenya Renewable Energy Research Consortium (MMU-RERC) and International Centre for Research in Agro-forestry (ICRAF) laboratories for providing research facilities. I would also like to thank the Higher Education Loan's Board (HELB) for Postgraduate Scholarship awarded (Grant. No. HELB/PS/2022/19) towards successful completion of this work.

My sincere appreciation goes to my wife Gladys, daughter Quinn, son Ian and family members Richard, Maureen and Japheth for being patient and understanding in the course of this study. To all my friends and everyone who, without mentioning names has contributed to make this study a success, receive my appreciation.

TABLE OF CONTENTS

LIST OF TABLES

LIST OF FIGURES

LIST OF APPENDICES

LIST OF SYMBOLS

Symbol	Description	Units
Å	Hamaker's constant	J
$\boldsymbol{\varepsilon}$	Dielectric constant	-
$\boldsymbol{\varepsilon_0}$	Permittivity of free space	-
$\boldsymbol{F_{mc}}$	Pressure differential force between air and water meniscus	N
$\boldsymbol{F_{st}}$	Surface tension force	N
$\boldsymbol{I}$	Output current	A
$\boldsymbol{I_d}$	Diffusion current	A
$\boldsymbol{I_{Rp}}$	Current losses	A
$\boldsymbol{I_{SC}}$	Short circuit current	A
$\boldsymbol{J_{MPP}}$	Maximum current density	A/m^2
$\boldsymbol{J_{SC}}$	Short circuit current density	A/m^2
$\boldsymbol{m_n}$	Subsequent masses	kg
$\boldsymbol{m_o}$	Mass before exposure	kg
$\boldsymbol{N_a}$	Avogadro's number	$Atom.mol^{-1}$
$\boldsymbol{\eta}$	Conversion efficiency	%
$\boldsymbol{C_{Ref}}$	Reference element	mg/kg
$\boldsymbol{C_x}$	Element concentration	mg/kg
$\boldsymbol{P_{max}}$	Peak power	W
$\boldsymbol{R}$	Radius	m
$\boldsymbol{R_H}$	Relative humidity	%
$\boldsymbol{SL_\varphi}$	Soiling factor	-
$\boldsymbol{T}$	Absolute temperature	^oC
$\boldsymbol{T_C}$	Temperature coefficient	^oC
$\boldsymbol{V_{MPP}}$	Voltage at maximum power point	V
$\boldsymbol{V_{OC}}$	Open circuit voltage	V
$\boldsymbol{Z}$	Particle separation distance	m
$\boldsymbol{\gamma}$	Surface tension	N/m
$\boldsymbol{\rho_0}$	Density of dust particle	kg/m^3

ACRONYMS AND ABBREVIATIONS

AfSIS	Africa Soil Information Service
Al	Aluminium
APE	Average Photon Energy
As	Arsenic
ASAL	Arid and Semi-Arid region
a-Si	Amorphous silicon PV module
Ba	Barium
BART	Bayesian Additive Regression Tree
Br	Bromine
Ca	Calcium
CBK	Central Bank of Kenya
Cd	Cadmium
Cl	Chlorine
Co	Cobalt
Cr	Chromium
Cu	Copper
C_n	Costs
DC	Direct Current
DGHI	Daily Global Horizontal solar Irradiance
DOD	Depth of Discharge
EDXRF	Energy Dispersive X- ray Fluorescence
EF	Enrichment Factor
EM	Electromagnetic
Fe	Iron
EPRA	Energy and Petroleum Regulatory Authority
FI_n	Future Income
Ga	Gallium
GHGs	Green House Gases
GPS	Global Positioning System
Hg	Mercury

ICRAF	International Centre for Research in Agro-forestry
IR	Infra-red
ISIS	International Soil Information System
ISRIC	International Soil Reference and Information Centre
K	Potassium
KEBS	Kenya Bureau of Standards
KMD	Kenya Meteorological Department
KPLC	Kenya Power and Lighting Company
Mg	Magnesium
MIR	Mid Infrared
Mn	Manganese
MPPT	Maximum Power Point Tracking
m-Si	Mono-crystalline silicon PV module
Na	Sodium
Ni	Nickel
NPV	Net Present Value
O&M	Operation and Maintenance costs
Pb	Lead
PC	Principal Component
PCA	Principal Component Analysis
PLS	Partial Least Squares
PI	Profitability Index
p-Si	Poly-crystalline silicon PV module
PV	Photovoltaic
PV_n	Present Value
PXRF	Portable X- ray Fluorescence
Rb	Rubidium
RF	Random Forest
S	Sulphur
Sb	Antimony
Sc	Scandium

SC	Small Commercial
Se	Selenium
SHS	Solar Home Systems
Si	Silicon
SOC	Soil Organic Carbon
Sr	Strontium
S_n	Savings
STC	Standard Testing Conditions
Ti	Titanium
TMOT	Typical Module Operating Temperatures.
V	Vanadium
XGB	Extreme Gradient Boosted Trees
XRF	X- ray Fluorescence
Zn	Zinc
Zr	Zirconium

ABSTRACT

Solar photovoltaic (PV) is one of the emerging technologies widely acknowledged as a potential solution to energy poverty. This is because of its high reliability, long life, and automatic operation with minimal maintenance requirements, despite its low conversion efficiency and high capital costs. Studies have been conducted on mechanisms of improving the power conversion efficiencies (η) of field deployed PV modules which tend to degrade with time. For instance, dust, dust accumulation, shadowing, birds dropping, water droplets, and wind speeds have been independently investigated. Much focus is laid on the effect of dust accumulation, with little attention on correlation between wind speeds, relative humidity and module orientation on dust deposition rates and characteristics, on PV modules which form the basis of soiling. This study looked at how wind profiles, relative humidity, and module placement affected dust deposition on the surfaces of photovoltaic modules, and thus their overall performance in an outdoor setup. The analysis of dust deposits on five photovoltaic (PV) systems installed at five study sites within Machakos County was done. The selection of the study sites was informed by the environmental conditions, location, topography and the soil types. The effect of module installation height, tilt angle, and orientation on the rate of dust deposition on the surfaces of PV modules was investigated. As a result, the effect of various dust categories on P_{max} and η was quantified. During the study, the rate of dust deposition was noted and the elemental concentration of the dust deposits identified and used to classify the dust into biogenic, geogenic and anthropogenic origin. Effect of the dust deposits on the performance of mono-crystalline silicon (m-Si) solar modules exposed to ambient conditions was investigated. Correlation between adhesive forces of the dust deposits to the resuspension forces required to naturally dislodge the adhered dust particles on PV surfaces was probed. Thereafter, an automated scalable PV module cleaning system utilizing air and water jets fitted in a bi-directional motor was fabricated and tested on a dusty module. Solar PV modules installed at the five study sites showed a monthly average decrease in η of 2.60%, 3.48%, 8.1%, 5.5%, and 2.76% at sites 1, 2, 3, 4 and 5, respectively. Similarly, leeward-facing module surfaces exhibited higher deposition rates as compared to the windward facing modules in southerly winds. In addition, sites with traces of anthropogenic particles on dust samples collected from PV surfaces show a greater decrease in efficiency, while sites with biogenic and geogenic particles show minimal effects. An abundance of anthropogenic dust particles, combined with a mild tilt and leeward orientation, resulted in a faster degradation rate of maximum power and efficiency. Similarly, the monthly modules peak power (P_{max}) degradation rate was observed to be higher (8.8%) for sites experiencing a higher temperature coefficient (T_c) for V_{MPP} due to temperature effects of soiling, lower wind speeds, and a higher relative humidity. Lower deposition rates were observed in locations with higher wind speeds and a higher module tilt angle, resulting in a lower effect on the reduction of current and voltage parameters. Similarly, the average wind speeds at each site were insufficient for complete particulate resuspension of small particles (less than 500 µm) adhering to the PV module surface. As a result, dust accumulations on the surface of PV modules had a significant negative impact on current and voltage

parameters. Therefore, an automated self-cleaning system was designed, fabricated and tested based on the study findings to counter-act the effects of soiling observed on the PV modules. The study findings revealed a 12.26% increase in η of the dusty solar PV module after cleaning using the automated system as compared to its performance before exposure to dust. From the study findings and existing challenge of inability to incorporate self-cleaning mechanism at the design stage of solar PV modules, we recommend incorporation of the automated self-cleaning model in the design of PV module frames. This is contrary to the existence of the automated self-cleaning system as a separate entity incorporated at the installation stage. This remedy provides a tailor-made solution to soiling hence averting the deleterious effects of soiling on PV modules.

CHAPTER ONE

INTRODUCTION

1.1 Background

Solar photovoltaics (PV) is one of the greatest renewable energy alternatives for supplying green energy to the ever-growing population and industrial growth due to its high reliability, long life, autonomous operation, and low maintenance requirements. Solar PV has some unique characteristics, such as modularity and quick deployment lead times, which make it a good technology for alleviating energy poverty, particularly through the deployment of off-grid Solar Home Systems (SHS) and mini-grids in rural areas. Similarly, photovoltaic technology is presented as a potential energy source for reducing the rise in Greenhouse Gases (GHGs) emission. This is attributable to abundance, emission-free, and limitless nature of solar energy (Mustafa *et al.*, 2020). Despite the enormous advances made in solar energy, photovoltaic technology is still not widely utilized as a primary energy source. This is as a result of their low power conversion efficiency (less than 30%) and the constant degradation of the optimal operation points brought about by shading and other environmental conditions (Memiche *et al*., 2020). Despite the simplicity of conversion, ambient weather conditions have a significant impact on PV technology. Cell temperature, irradiance change, maximum power point tracking (MPPT), and geomagnetic field are among the parameters that have been conclusively identified to affect the performance of PV modules when used outdoors (Ndeto *et al*., 2020).

The adoption of PV technology is seriously hindered by low power conversion efficiency, which gets worse when exposed to ambient conditions. For instance, Fountoukis *et al.,* (2018) discovered that dust deposits have negative impacts on the functionality of PV modules in desert environments, thus lowering the overall conversion efficiencies of PV modules. In PV modules, the creation of electron-hole pairs is restricted due to a reduction in photon energy brought about by dust deposits, which causes a drop in photocurrent (Syafiq et al., 2018). Rising industrial activity, number of vehicles on the road, and population, have a big impact on dust's

constituents (Kazem *et al.,* 2021). According to Jiang *et al*., (2018), the impact of different dust particle sizes, content, and the ideal wind speeds needed for effective cleaning was deemed obscure and inconclusive.

For determination of ideal module location for efficient self-cleaning mechanisms and increase in conversion efficiency, analysis of shading and deterioration of existing PV modules caused by different weather conditions, particularly wind and relative humidity is paramount (Rahman *et al*., 2015; Wang *et al*., 2019). According to Lu *et. al.*, (2018), upwind PV systems had higher dust deposition rates than downwind installations. Moreover, the geometric mean diameters of wind-blown sediments grew exponentially as wind speed increased (Wang *et al.*, 2019). Although the rates of wind-blown sediments and dust deposition have been examined, it is unclear how module installation height, tilt angle, and orientation affect the patterns of deposition with regard to wind direction (upwind and downwind). The relevance of harsh soiling on overall PV module performance as determined by relative humidity and wind speeds is thus highlighted by this study.

In a similar manner, the strength of the adhesive forces holding dust particles to the surface of outdoor PV modules under various environmental conditions is evaluated. The ideal wind speeds needed to provide enough lift and drag forces for full dust particle resuspension from the PV surfaces are investigated. Also, the impact of dust deposits on crystalline silicon solar cells as well as the rate of current and voltage parameter degradation are determined. Finally, an automated self-cleaning model for dusty PV modules was designed, fabricated and tested in an outdoor setup.

1.2 Statement of the problem

According to the World Energy Outlook, by 2030, low-emission electricity sources will likely surpass the consumption of fossil fuels. Among low polluters, renewable energy sources are more common than alternative energy sources. When compared to wind, hydropower, and geothermal energy, solar energy is thought to be more enticing among renewables due to its abundance and limitlessness nature. Despite the enormous advancements in solar cells technology, its share in global energy mix is still low. This is as a result of the modules' low conversion efficiency (less than 30%)

and the unabated erosion of their ideal functioning points owing to shading and other environmental factors (Jiang *et al.*, 2017; Luque *et al.*, 2018).

The performance of a PV module in outdoor conditions is substantially different from what is anticipated from laboratory measurements. For instance, how well a PV module function is influenced by the sun's position, solar irradiation intensity, temperature, and the load demand. The performance of PV systems has been demonstrated to be impacted by environmental factors such as dust accumulation, water droplets, bird droppings, and partial system shadowing (Mustafa *et al.*, 2020). Previous research studies have identified dust as one of the key factors contributing to poor performance of installed PV systems hence low uptake. For instance, Wang *et al.,* (2019) demonstrated that dust emission efficiency increased with wind speeds, but it was unclear how wind speed affected the ratio of vertical to horizontal dust flux. Moreover, it was unclear and inconclusive how different dust particle sizes, compositions, and ideal wind speeds affected self-cleaning mechanisms (Jiang *et al*., 2017). Similarly, dust, a key component of soiling, contributes immensely to the decline of the solar cells conversion efficiency and depends on various parameters namely; module siting, anthropogenic activities, surrounding crustal soil profile, wind profile and ground cover among others. Dust obstructs incident radiation falling on PV surfaces leading to reduced photo current. High capital costs coupled with low conversion efficiency which degrades further upon exposure to dust and other environmental conditions greatly hinders widespread uptake of PV technology.

Due to these drawbacks, it is necessary to research on mitigation measures on effect of dust on performance of PV modules. This can be achieved by first identifying the ideal wind speeds, module siting, and dust composition at various module heights and their potential sources with the ultimate goal of identifying the ideal orientation for minimal dust effect. Similarly, the study findings inform on the design of an automated self-cleaning PV system.

1.3 Justification

Making wise investment decisions in solar PV systems requires knowledge of the technological risks relating to the operational effectiveness and dependability of field

deployed systems, including aging and deterioration of PV modules. In order to maximize the performance of PV modules, it is essential to understand how they operate in an outdoor setting. Ambient conditions and the mounting techniques employed are two of the most crucial factors affecting a PV system's operation and efficiency. Solar PV uptake in Kenya has seen a 41.84% leap to an installed capacity of 367.5 MW over the past year (EPRA, 2024). This represents 2.04% of the total estimated potential.

As the world embarks on measures to curb the rising effects of global warming, the uptake of solar PV technology needs to be beefed up due to its huge unexploited potential. PV systems' inherent low η, which requires a substantial upfront investment, has been a significant disadvantage despite the technology's recent surge in research interest. Moreover, the efficiency of PV panels operating in ambient settings is further reduced by external factors such as temperature, soiling, and shade (Ngwashi & Tsafack, 2023). This calls for improved PV module η leading to reduced active area per kilo watt of electric power generated. Similarly, field deployed PV system ought to be optimized and cleaned regularly with the aim of reducing the degradation rates.

In readiness to the attainment of Vision 2030 in seven years' time, accelerated research and development in solar PV need to be done with the aim of bridging the gap between the installed and estimated potential. The results of this research may inform on the contribution of wind profiles, relative humidity, and module placement on dust deposition on the surfaces of photovoltaic modules, and thus their overall performance in an outdoor setup. Similarly, design and fabrication of an automated self-cleaning model may mitigate on the effects of dust deposits hence improved η.

1.4 Objectives

1.4.1 Main Objective

To determine and quantify the composition and effect of dust deposits on mono-crystalline silicon solar modules under varying wind speeds, relative humidity,

installation height and orientation, hence design a self-powered, automated and scalable solar PV surface cleaning system.

1.4.2 Specific Objectives

i. To determine site specific irradiation, wind speeds and direction, modules installation height, tilt angle and orientation for the selected sites.
ii. To assess and determine the rate of dust accumulation hence its effect on the current and voltage parameters of m-Si solar modules in five selected sites.
iii. To determine the effect of module height, tilt angle and orientation in southerly winds to the overall dust deposition patterns.
iv. To examine and characterize the composition of the accumulated dust particles on PV modules at site specific inclination and azimuth angle and subsequent effect on the conversion efficiency of m-Si PV modules in the selected sites.
v. To design, test and perform economic analysis of a model for self-cleaning mechanism using denser medium in conjunction with air and simulated field conditions.

1.5 Research questions

The research questions which guided this study were;

1. What are the ambient conditions (irradiance, wind speeds and direction) and existing module placement in the selected sites?

2. What is the rate of dust built-up on the PV module surface and how is it impacted by varying wind speeds across the study sites and consequently, its effect on the current and voltage parameters?

3. How does the variation in installed module height, tilt and orientation in southerly winds affect the particle deposition patterns of the wind-blown sediments?

4. What is the elemental composition of the dust accumulated on the surfaces of the PV study modules in the five selected sites and their effect on the conversion efficiency of the modules (m-Si PV module)?

5. To what extend does the designed automated self-cleaning model improve the performance of the degraded dusty modules and how economical is it compared to conventional cleaning methods?

1.6 Scope of the Study

This research investigated the composition and effects of dust deposits on the performance of a mono-crystalline silicon (m-Si) solar module. The study identified and characterized the composition of the accumulated dust particles on PV module surfaces at site specific inclination and azimuth angles and subsequent effect on the conversion efficiency of m-Si PV module in the selected sites. Effect of module siting in southerly winds to the overall dust deposition patterns was also investigated. Particulate specific ideal wind speeds for effective wind cleaning under different module heights and tilt angles was examined in the chosen sites in Machakos County.

This study used the models validated by Besson *et al.* (2017), Pelt *et al*. (2003), and Wang *et al.* (2019) to calculate the rates of dust deposition and the aggregate size distribution of wind-blown sediments on PV modules. The wind speeds for the distribution of wind-blown sediments' particulate matter and particle morphology were determined. At a specific module height, the modules' contribution to the self-cleaning mechanism and their orientation in relation to the wind direction were also determined. In order to find the appropriate wind speeds for self-cleaning systems, the association between wind speeds, dust composition, and resuspension rates was determined and examined. Based on the study's findings, the examined factors helped in the design and fabrication of an automated self-cleaning model best suited for outdoor installations. The experimental tests were conducted to determine the extend at which the designed automated self-cleaning model improved the performance of the degraded dusty modules.

1.7 Limitations

Due to concerns about the security of the measuring devices that would be placed in the field, the study was limited to PV systems used by the Machakos County government for solar water projects. The effects of dust accumulations on solitary PV modules installed below 3.7 m were also not studied because of the possibility of vandalism and interference of the field setups installed at a lower height. On the other hand, large-scale commercial solar PV projects may be able to apply the methodology employed in the study of how wind profiles, relative humidity, and module location impact dust deposition on photovoltaic module surfaces and efficiency.

CHAPTER TWO

LITERATURE REVIEW

2.1 Introduction

This chapter covers the fundamentals of solar cell operation, as well as the various solar cell technologies, their performance indices, and the variables that influence performance. In a similar vein, variables influencing PV module performance are also discussed, along with potential remedies. The mechanisms that adhere dust particles to photovoltaic surfaces are examined, and potential methods for cleaning the surfaces to loosen the particles are also highlighted. A synopsis of the shortcomings of earlier studies on solar cells degradation from dust deposits is also provided.

2.2 Theoretical Principles

2.2.1 Operating principles of a solar cell

A solar cell is a semiconductor device that converts sunlight into electrical energy via the photovoltaic effect, which is both a physical and chemical phenomenon (Bagher, 2015). A solar cell operates similarly to a p-n junction semiconductor, which generates a direct current (DC) when exposed to light energy. This is accomplished by generating diffusion and drift currents across the junction for direct and reverse polarization as a result of electron-hole pair excitation and separation (Pandey & Singh, 2016). Solar cells are the building blocks of photovoltaic (PV) modules (solar modules), and their operation necessitates four fundamental principles: light absorption, electron-hole pair generation, separation of charge carriers of opposing types, and finally separate extraction of the carriers to an external circuit (Bagher, 2015). An electrical circuit of an ideal solar cell, according to Pandey *et al* (2016), can be equated to a current source connected in parallel to a diode. Figure 2.1 shows a schematic diagram for the equivalent solar cell circuit.

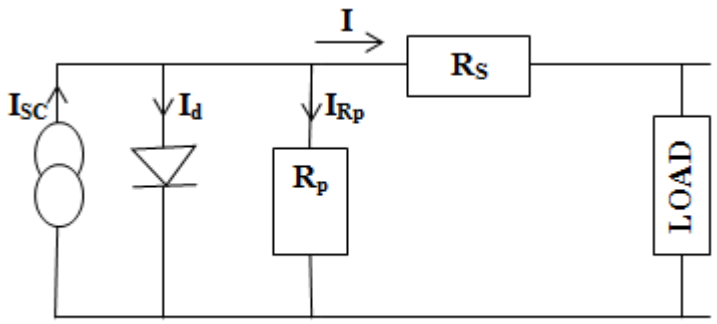

Figure 2.1: Equivalent solar cell circuit

From Figure 2.1 the solar cells output current ***I*** can be calculated based on the solar cell equivalent circuit as;

$$\boldsymbol{I = I_{SC} - I_d - I_{Rp}} \qquad 2.1a$$

where $\boldsymbol{I_{SC}}$ is the short circuit current generated by irradiation, $\boldsymbol{I_d}$ and $\boldsymbol{I_{Rp}}$ represent the diffusion current of the internal diode and current lost due to the resistance in the cell respectively. Considering the characteristics of the solar cell as a p-n junction diode, the output current of the solar cell can be rewritten as (Pandey & Singh, 2016);

$$\boldsymbol{I = I_{SC} - I_0}(e^{\frac{q(V_0+IR_S)}{AKT}} - 1) - \frac{(V_0 + \boldsymbol{I}R_S)}{R_P} \qquad 2.1b$$

where, ***I*** and $\boldsymbol{I_0}$ refer to the output current and reverse saturation current of the diode respectively. V_0 refers to the voltage of the solar cell, q is the charge of an electron, A is the ideality factor of the diode, K is the Boltzmann's constant, T is the temperature in Kelvin, R_S and R_P represents the internal series and parallel resistance respectively.

The solar cell conversion efficiency, η is calculated by the ratio of power at maximum power point, P_{max} to the input irradiance (***E***, in W/m^2) under STC and the surface area of the solar cell, ($\boldsymbol{A_C}$ in m^2) (Pandey *et al.*, 2016);

$$\eta = \frac{P_{max}}{(E \times A_C)} \qquad 2.2$$

But maximum power point is calculated as (Meral & Din, 2010);

$$P_{max} = V_{MPP} \times \ I_{MPP} \quad (2.3)$$

where V_{MPP} and I_{MPP} represent voltage and current at maximum power point.

2.2.2 Types of solar cells

The main function of a solar PV cell is to convert solar radiation, also known as the photovoltaic effect, from pure light into electrical energy. Photovoltaic cells are manufactured employing a variety of technologies, including material modification with varying photoelectric conversion efficiencies in the cell components. Photovoltaic technologies can be categorized into four main groups as a result of the development of numerous unconventional manufacturing techniques for producing functional solar cells. The first-generation PV technologies use crystalline silicon cells (c-Si), which are further classified into four categories based on how the silicon wafers are made and the type of silicon used. These are mono-crystalline, polycrystalline, multi-crystalline and III-V single junction solar cells. A summary of the different types of the solar cells is presented in Figure 2.2 (Pastuszak & Węgierek, 2022).

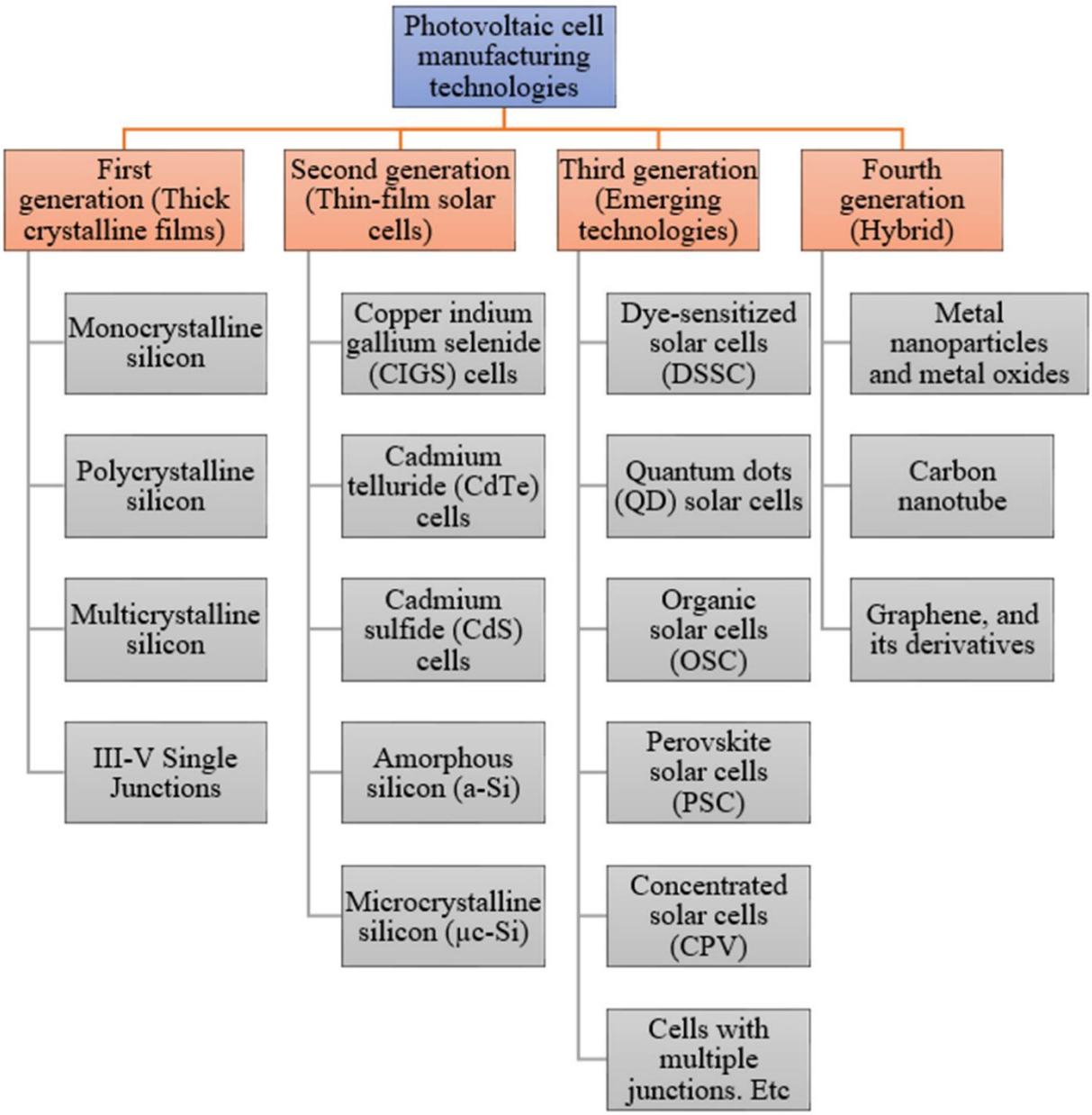

Figure 2.2: Solar Cell Technologies (Pastuszak & Węgierek, 2022)

The creation of second-generation solar cells involves the advancement of first-generation photovoltaic cell technology along with thin-film photovoltaic cell technology, which led to the development of microcrystalline silicon (µc-Si) and amorphous silicon (a-Si), copper indium gallium selenide (CIGS), and cadmium telluride/cadmium sulfide (CdTe/CdS) photovoltaic cells.

Due to the high production costs of first-generation PV technologies, as well as the toxicity and limited availability of materials for second-generation, third-generation PV technology emerged. This generation of solar cells differs from previous generations in that it does not rely on the p-n junction design used in previous generations. Nano-materials, silicon wafers, solar inks incorporating conventional printing press technologies, organic dyes, and conductive plates are among the new materials used in this generation of solar cells. Dye Sensitized Solar Cells (DSSC), Perovskite Cells, and Organic Photovoltaic Solar Cells are examples of these solar cells (OPV) (Marques *et al.*, 2022). Similarly, Quantum Dots Solar cells which are few nanometer-sized nano-crystals with tunable optical properties are being explored and tested for solar cells (Özönder *et al*., 2023). The cost of manufacturing perovskite solar panels is lower since they may be made with low-cost materials and simple construction methods. Since perovskites are sensitive to heat and humidity, they also have the best power conversion efficiency, but their large-scale manufacture is hampered by their susceptibility to environmental deterioration. Similar to organic solar cells, which are among the least expensive forms of energy, they are also lightweight, semitransparent, and ecologically benign. Nevertheless, they are not very stable and have a limited lifespan. Durability, high efficiency, and tunability are features of quantum dot-based solar cells (QDSSC). On the other hand, certain QDSSC kinds, including quantum dots of cadmium selenide (CdSe), are extremely poisonous and dangerous for the environment (Rehman et al., 2023).

Despite the development of new PV technologies, silicon solar cells account for more than 80% of global production (Quansah & Adaramola, 2018). This technology's modules have a long history of dependability, with guarantees lasting 20-25 years, which is unusual among products. Silicon, on the other hand, is a common component of the Earth's crust and exists in the form of non-toxic silicon dioxide (quartz sand). Fourth-generation solar cells, which are more affordable, include flexible architectures, and provide the high stability of nanomaterials, incorporate all the advantages of earlier generations of solar cells. Due to their capacity to combine inorganic and organic elements, they are also known as hybrid solar cells. Typically, they consist of graphene and its derivatives, carbon nanotubes,

metal oxides, and metal nanoparticles (Pastuszak & Węgierek, 2022). Due to widespread use in Solar Home Systems (SHSs), off-grid and grid-tied power production in most developing countries, this study focused on mono-crystalline silicon solar cells.

2.2.3 Solar Cells Conversion Efficiencies

Solar-cell efficiency is the percentage of solar radiation that a solar cell can use to generate electricity using photovoltaics. The solar cell efficiency in a photovoltaic system, along with temperature and latitude, influences the system's annual energy output. Since typical photovoltaic systems only have one p–n junction, they are subject to a lower efficiency limit that Shockley and Queisser refer to as the "ultimate efficiency". Photons whose energy is less than the absorber material's band gap are unable to produce an electron-hole pair, meaning that their energy cannot be transformed into useful output and will only produce heat if they are absorbed. Only a small portion of the energy above the band gap in photons may be transformed into usable output. The surplus energy above the band gap that is absorbed by a photon with higher energy is transformed into the kinetic energy of the carrier combination. As the kinetic energy of the carriers slows to equilibrium velocity, the surplus kinetic energy is transformed into heat through phonon interactions. Shockley–Queisser limit of 33.16% is the greatest theoretical efficiency for conventional single-junction cells with appropriate band gap for solar spectrum. Multiple band gap absorber materials in solar cells increase efficiency by breaking the light spectrum into smaller bins, each of which has a greater thermodynamic efficiency limit (Rühle, 2016). Figure 2.3 presents a summary of solar cells conversion efficiencies.

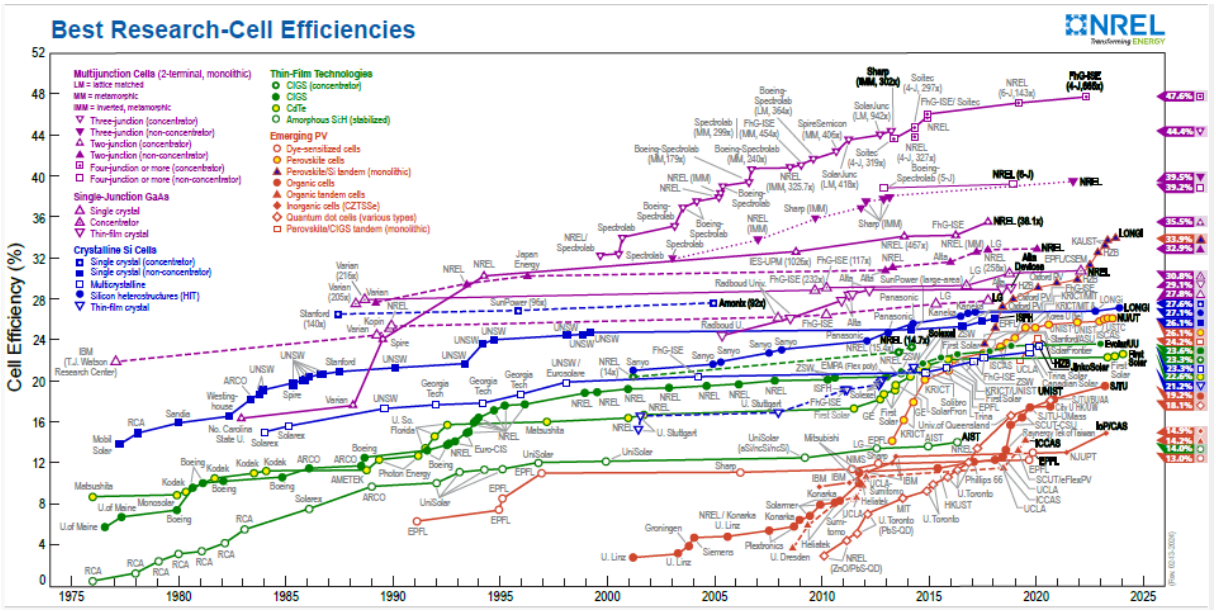

Figure 2.3: Best Research-Cell Efficiency Chart (NREL, 2024)

Observe in Figure 2.3 that the efficiencies of Si solar cells are low; they are less than 30%, with the best value being 27.6% for mono-crystalline Si- solar cells. This demonstrates that a solar irradiance of 1000 W/m^2 is converted to less than 300 W/m^2. As a result, more aperture area is required for the generation of 1 kW of electric power, resulting in an increase in production cost.

The fraction of incident photon energy converted to electrical energy by solar cells is directly proportional to the fraction of incident radiation absorbed by the solar cells. Several factors contribute to incident radiation obstruction, resulting in lower PV module conversion efficiency. Cell temperature, irradiance variation, Maximum Power Point Tracking (MPPT), and energy conversion efficiency are all important factors in determining the performance of solar cells. Module siting, which includes geographical location, module orientation, and inclination, is critical in aligning the active module surface with the solar path. Similarly, environmental factors such as dust accumulation, shadow, water droplets, snow, and bird droppings refract or tint the aperture area of a PV module. These conditions actively participate in the degeneration of electron-hole pairs by reducing incident radiation (Mustafa *et al.*, 2020). The performance of field-installed PV modules degrades as exposure time

increases. Cell temperature, soiling, shading, and the earth's magnetic field all hasten the rate of degradation (Ndeto *et al.*, 2020).

2.2.4 Shading Effect on PV Modules

PV system performance is primarily determined by geographic location (latitude and local solar insolation patterns), installation design, and environmental factors. Among the environmental factors, shadowing dictates the performance of PV modules. Shadowing indicates that photons are being obstructed from reaching the photovoltaic cells. Electrical mismatch conditions on PV modules can occur when solar cells are subjected to non-uniform irradiance or are partially shaded, or when differences between solar cells are inherent in the manufacturing process (Abdelaziz *et al*., 2021). Shadowing is a common occurrence, particularly on field deployed PV systems. Managing the shadow possibility is difficult for designers because partial shadowing can appear from a variety of sources, such as surrounding buildings, trees, antennas, poles, and accumulation of dirt or dust.

The accumulation of dust and other minute particles on PV modules is known as soiling. It is one of the most important factors influencing PV performance. The power loss caused by dust, snow, dirt, and other particles on the PV module surface is referred to as soiling loss. Pollution, bird droppings, lichen growth, wind-borne particulate matter, agricultural activities, construction work, and pedestrian and vehicular movements are all sources of soiling (Shaju & Chacko, 2018). Soiling causes two types of shading: soft shading and hard shading. The accumulation of smog in the air is referred to as soft shading. Hard shading, on the other hand, refers to dust accumulation on the PV module, which results in less incident solar radiation reaching the solar cells (Maghami *et al.*, 2016; Schill *et al*., 2015). Natural dust properties, such as optical, size, geometry, and electrostatic deposition patterns, which include hard shading, have received less attention and documentation (Mustafa *et al.*, 2020).

The ability of the glass covers to transmit radiation to the solar cells is critical to the performance of the PV module. The accumulation of dust on the surface of PV modules is one of the causes of gradual degradation of transmittance. For instance, in

a series-connected string of cells, same current flows through all of the cells. When one or more cells are shaded, the maximum permissible current decreases, resulting in a decrease in output power. Furthermore, shaded cells can overheat, resulting in hotspots and permanent PV module damage. Shading on a single photovoltaic cell can cause the photovoltaic module to fail (Shaju & Chacko, 2018). Shaded solar cells become extremely resistive, impairing the performance of other exposed solar cells (Syafiq *et al.*, 2018). According to previous studies, shading has a significant impact on current parameters and is dependent on the number of cells shaded (Maghami *et al.*, 2016).

2.2.5 Dust Characterization

Dust, the main component of PV soiling, has different properties depending on its source. Dust is classified into three types: geogenic, biogenic, and anthropogenic (Alnasser *et al*., 2020). Geogenic particles are natural particles that form as a result of erosion, sandstorms, forest fires, and volcanic activity. Pollen, a seasonal allergen, as well as transformation products of natural semi-volatiles such as isoprene and terpenes, are examples of biogenic particles or bio-aerosols. Finally, anthropogenic particles are produced as a result of combustion, metallurgy, and bulk and filter dust handling. Anthropogenic particles are made up of adsorbed chemicals, bio-contaminants, or condensed gases (Kazem *et al.*, 2021). PV modules exposed to different types of dust but with similar spectral irradiance would perform differently.

The properties of dust particles are affected by both particle formation and post-particle processes. Fine and coarse mode particles, for example, have different chemical compositions and sources, and are transported and removed via different mechanisms (Kazem *et al.*, 2021; Saradhi *et al.*, 2014). Combustion processes emit a cluster of particles containing various trace elements found in fuel or lubricants used in motor vehicles. Because of their ultra-thin nature and low susceptibility to chemical transformation, these particles travel over long distances in the atmosphere. Mechanical processes, on the other hand, such as mining, mineral processing, quarrying, grinding, dust resuspension, and so on, produce particles that are predominantly composed of crustal elements (Rahman *et al.*, 2021). Table 2.1

summarizes some common sources of emissions in terms of the characteristic elements emitted.

Table 2.1: Characteristic Elements Corresponding to Different Sources of Emission

Emission source	Characteristic elements emitted
(a) Road transport	
Motor vehicle emission	- Br, Pb, Ba, Mn, Cl, Zn, V, Ni, Se, Sb, As
Engine wear	- Fe, Al
Tyre wear	- Zn
Road side dust	- Earth Crust, Al, Si, K, Ca, Ti, Fe, Zn
(b) Industrial facilities	
Oil powered power plants	- V, Ni
Coal combustion	- Se, As, Cr, Ca, Cu, Al, S, P, Ga
Oil refineries	- V
Non-Ferrous metal smelter	- As, Sb, Cu, Zn, Pb, Cd, Hg
Iron and Steel mills	- Zn, Pb
Copper refinery	- Cu, Zn
(c) Small combustion	
Refuse incineration	- Zn, Sb, Cu, Cd, Hg, K, Pb
Wood smoke	- Ca, Na, K, Fe, Br, Cl, Cu, Zn
(d) Mining and material processing	- Al, Mg, K, Sc, Fe, Mn
(e) Re-suspended soil	- Si, V, Cr, Al, Ca, Mg, Fe, Ti, Sr, Mn, Sc

Source: (Schwela et al., 2002)

The nature of the source and the surrounding environment can cause a suite of elements and their concentrations to change over time (Schwela *et al.*, 2002). Powering modern engines at maximum power (while maintaining fuel economy), for example, necessitates intervening measures such as improved engine design and transmission. The petroleum industry is matching efforts to provide fuel and lube to desired performance levels, resulting in the need for additives (Calabokis *et al.*, 2022). Fuel additives are a dynamic and ever-changing process that results in newer additional trace elements in motor vehicle emissions (Hanum *et al.*, 2018). As a result, elements present in road transport emissions may vary in the future depending

on the fuel and lubricants used (Calabokis *et al.*, 2022). This study's characterization of emission sources was based on Table 2.2.

2.2.6 Enrichment Factor (*EF*)

The Enrichment Factor (*EF*) is a criterion for differentiating between anthropogenic and natural sources of elements in a sample based on their ratio to the primary component in the background soil composition (Rahman *et al.*, 2021). Metal *EF* (Me) can be calculated using a common element found in the earth's crust as a reference. In most cases, aluminium (Al) or iron (Fe) are used as normalizers, with the element concentration in the crust serving as the background. The enrichment factor is mathematically defined as (Vanegas *et al.*, 2021);

$$EF = \frac{(C_x / C_{ref})_{Sample}}{(C_x / C_{ref})_{Background}} \qquad 2.4$$

where C_x represents the element concentration and C_{ref} refers to the reference element (Al or Fe) concentration. *Sample* represents the dust samples collected at the study sites and *Background* refers to site specific crust elements from the soil sample. The enrichment factors are classified according to the ranges presented in Table 2.2 (Vanegas *et al*., 2021).

Table 2.2: Enrichment Factor Ranges and Classifications

Range	Classification
EF < 2	Minimal or normal enrichment
2 ≤ EF < 5	Moderate enrichment
5 ≤ EF < 20	Significant enrichment
20 ≤ EF < 40	Very high enrichment
EF ≥ 40	Extremely high enrichment

Effects of anthropogenic influence on the dust deposits are identified by significant enrichment (EF ≥ 5) of Zn, Cu, Ni, Sr, Zr, Rb or Pb in the dust samples, otherwise no significant anthropogenic contribution on the deposits. Similarly, biogenic sources are identified by abundance of K, P, S, Cl, Zn or Br. On the other hand, geogenic

origin are identified by high loading factors of Al, Si, Ca, Ti, Mn or Fe which comprise of crustal elements (Vanegas *et al.*, 2021).

2.2.7 The Evolution of Natural Dust and its Deposition Characteristics on PV Modules

The majority of hard shading on PV modules is caused by dust deposits. The patterns of dust deposition on PV modules are highly dependent on module orientation in relation to wind direction and module tilt. Dust aerosols are naturally emitted by saltation bombardment, which causes sand blasting; the release of dust aerosols from saltating dust aggregates or those impacted by saltators. Wind speeds exceeding the fluid threshold for saltation; the threshold wind speed above which dust emission occurs, cause the emission of dust aerosols from either soil aggregates or saltating dust aggregates. Mineral dust aerosols are removed from the atmosphere by either dry deposition or wet deposition after emission (Kok *et al.,* 2012). The combined action of gravity settling with turbulent diffusion in the atmosphere boundary layer and molecular diffusion in the laminar sub-layer near the surface causes dry deposition. In contrast, wet deposition involves both in-cloud and below-cloud scavenging. In-cloud scavenging occurs when dust particles serve as cloud condensation, whereas below-cloud scavenging occurs when raindrops collect dust aerosols (Gray, 2011; Stovern *et al*., 2016). Gravity separation completely controls coarse particle deposition in low wind speed conditions (sedimentation). In windy conditions, turbulent eddies accelerate particles to the surface, resulting in an additional inertial deposition rate to the sedimentation rate (Figgis *et al.,* 2018).

2.2.8 Adhesive Forces and Particle Resuspension

Particulate resuspension is a treatment for hard shading. Even though large particles require lower resuspension velocities than smaller ones, natural methods such as wind can effectively clean them. Wind velocities ranging from 0.23 m/s to 57.56 m/s are considered ideal for particle resuspension and are dependent on particle diameter (Lu & Zhao, 2018). Wind speeds and relative humidity both have an equal impact on particle rebound and resuspension (Figgis *et al.,* 2018). Particles detach from a wind-blown surface in a rolling motion when the moment established by aerodynamic drag

on the particle overcomes the moment established by adhesion forces (Henry & Minier, 2014).

Theoretical and experimental studies of the forces that govern the mechanism of bonding between dust and PV surfaces reveal four distinct forces of attraction. The main forces involved in particle adhesion on PV surfaces are capillary, Van der Waal, electrostatic, and gravitational forces. Capillary forces predominate in higher humidity, whereas Van der Waal forces predominate in low humidity. Furthermore, surface roughness from clean glass to coated glass has no effect on adhesive forces (Isaifan *et al.*, 2019).

The capillary forces are made up of two forces: surface tension, $\boldsymbol{F}_{st}$, and the force due to the difference in pressure between the air and water meniscus, $\boldsymbol{F}_{mc}$, which is present in a particle adhered to a flat surface. The capillary forces between a spherical particle and a flat surface can be calculated from Eqn. 2.5 (Moutinho *et al.*, 2017);

$$F = 4\pi R\gamma \cos\theta \left[1 - \frac{z}{2r\cos\theta}\right] \qquad 2.5$$

where R is the radius of the spherical dust particle, γ is the surface tension, z is the particle separation distance (0.4 nm), θ is the contact angle between the surface and the sides of the water droplets (Figure 2.2) and r is the equilibrium radius of meniscus given by Eqn. 2.6 (Moutinho *et al*., 2017; Tan *et al*., 2014);

$$r = -\frac{V\gamma}{N_a kT\, ln\, R_H} \qquad 2.6$$

where V is the molar volume of the liquid (for water $V = 18.03\, ml.mol^{-1}$), N_a is Avogadro's number ($6.022 \times 10^{23}\ atom.mol^{-1}$) and k is the Boltzmann's constant ($1.38 \times 10^{-23}\ m^2 kgs^{-2}K^{-1}$), T is the absolute temperature and R_H is the relative humidity.

Van der Waal forces (dry adhesive forces) operate in dry, electrically neutral environments. They hold sway over dust particles and solid surfaces. Eqn. 2.7 gives

the Van der Waal force between a spherical particle and a flat surface (Tan *et al*., 2014);

$$F_{VDW} = \frac{\text{Å}R}{6z^2} \qquad 2.7$$

where Å is the Hamaker's constant and *R* is the particle's radius. For smooth surfaces and particle edges, z takes a value in the range of 0.35 to 0.40 nm (Quan *et al*., 2016).

Suspended dust particles in the air acquire electric charges as a result of collisions, creating an attraction force through the induction of opposite charges to the surfaces on which they settle. Electric charges can be generated through frictional contact in non-conductive materials such as glass, a phenomenon known as tribo-electrification. Eqn. 2.8 gives the magnitude of the interaction force caused by this charge distribution (Tan *et al*., 2014);

$$F_{electrostatic} = \frac{q^2}{16\pi\varepsilon\varepsilon_o R^2} \qquad 2.8$$

where q represents the charge of the dust particles, ε is the dielectric constant of the medium between the dust particles and the adhesive surface (for air $\varepsilon = 1$) and ε_o is the permittivity of free space (air). Similarly, the gravitational force acting on suspended dust particles is given by Eqn. 2.9 (Isaifan *et al.*, 2019);

$$F_{gravity} = \frac{4\pi R^3 \rho_o g}{3} \qquad 2.9$$

where ρ_o is the density of the particles.

Previous research on adhesive forces revealed that capillary force accounted for 98% of particle-surface attraction, with Van der Waal forces accounting for 2% (Isaifan *et al.*, 2019; Tan *et al.*, 2014). Gravity and electrostatic forces are negligible because of the small radius of the dust particles and the relatively high humidity, which eliminates the possibility of coulomb forces (Quan *et al.*, 2016).

The adhesive force exerted on dust particles deposited on PV surfaces is highly dependent on the sum of capillary and Van der Waal forces. Eqn. 2.10 gives the net force $F_{Resultant}$ acting on the dust deposits (Isaifan *et al.*, 2019);

$$F_{Resultant} = 4\pi R\gamma \cos\theta \left[1 - \frac{z}{2r\cos\theta}\right] + \frac{\text{Å}R}{6z^2} \qquad 2.10$$

Assuming the dust particles are perfect spheres and taking a 2-dimensional view of the particle-surface interface, the contact angle θ depend on the surface tilt angle $\propto$ and the angle between the horizontal and the spherical particle β as shown in Figure 2.4. Thus (Simsek *et al.*, 2021);

$$tan(\theta) = -\frac{d}{dx}(R^2 - x^2)^{\frac{1}{2}} \qquad 2.11$$

where $\theta = \alpha + \beta$ and x is an arbitrary horizonal distance from the point of contact of the spherical dust particle with the PV surface to a tangent drawn perpendicular to the horizontal and incident on the spherical surface of the particle.

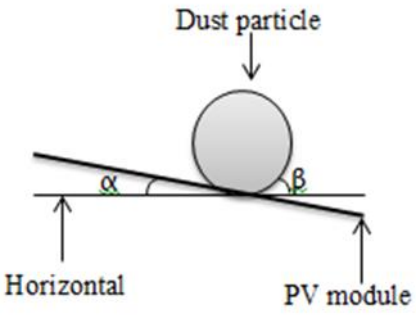

Figure 2.4: Dust Molecule Orientation with Respect to PV Module and Horizontal Surface.

Assuming a maximum contact angle given by $\tan\theta \approx 1$ due to the presence of adhesive forces and the state of equilibrium of the particles, then the approximate angle of contact between a spherical particle and the PV surface θ will be equivalent to 45^o. Replacing Eqn. 2.6 with Eqn. 2.10 and taking $\theta = 45^o$ we have (Traub, 2012);

$$F_{Resultant} = 2\sqrt{2}\,\pi R\left[\gamma + \frac{zN_a kT\,ln\,R_H\sqrt{2}}{2V} + \frac{\text{Å}}{24\pi z^2}\right] \qquad 2.12a$$

Taking V (for water) $= 18.03\,ml.mol^{-1}$), $N_a = 6.022 \times 10^{23}\,atom.mol^{-1}$, $k = 1.38 \times 10^{-23}\,m^2 kgs^{-2}$and $z = 4.00 \times 10^{-10}\,m$ (for smooth surfaces) and substituting for the constants in Eqn. 2.12a, a more simplified Eqn. 2.12b is generated given by (Moutinho *et al.*, 2017; Tan *et al*., 2014);

$$F_{Resultant} = 2\sqrt{2}\,\pi R\left[\gamma + \alpha T\,ln\,R_H + \beta\text{Å}\right] \qquad 2.12b$$

where $\alpha = \frac{zN_a k\sqrt{2}}{2V} = 1.304 \times 10^{-4}\,atom.kg.s^{-2}K^{-1}$, $\beta = \frac{1}{24\pi z^2} = 8.289 \times 10^{16}\,m^{-2}$.To completely remove settled dust particles from the surface of a PV module, a counter-acting force equal to the adhesive force is required. A fluid generates a counter-acting force on dust deposits on PV module surfaces exposed to ambient conditions (wind or rain water). The drag force, $\boldsymbol{F}_{Drag}$, and the lift force, $\boldsymbol{F}_{Lift}$, acts as counter-acting forces to adhesive forces in a steady viscous flow. Lift force is perpendicular to fluid velocity, whereas drag force is parallel to the flow. In a free stream $\boldsymbol{F}_{Drag}$ and $\boldsymbol{F}_{Lift}$ can be computed from Eqns. 2.13a and 2.13b (Rastello *et al.*, 2011);

$$F_{Drag} = 2\pi\rho V^2 R^2 C_D \qquad 2.13a$$

$$F_{Lift} = 2\pi\rho V^2 R^2 C_L \qquad 2.13b$$

where ρ is the fluid density, V is the velocity of the fluid and C_D and C_L represents drag and lift force coefficients, respectively. Equating Eqn. 2.12b to Eqns. 2.13a and 2.13b, the approximate fluid velocity V ideal for particulate resuspension from the surface of the PV module would be given by (Moutinho *et al*., 2017; Quan *et al*., 2016);

$$V = \sqrt{\frac{\sqrt{2}\left[\gamma + \alpha T\,ln\,R_H + \beta\text{Å}\right]}{\rho R(C_D + C_L)}} \qquad 2.14$$

where the variables carry their initial meaning defined earlier. Therefore, the optimal wind velocity required for self-cleaning is a factor of absolute temperature *T*, relative humidity R_H, radius *R* and the density ρ of the air.

2.2.9 Solar PV Module's Surface Cleaning Mechanisms

Cleaning must be done on a regular basis to preserve PV performance since dirt buildup impedes the PV module's capacity to convert light into power. One possible source of cleaning agents for PV modules has been discussed, namely ambient wind. Studies on the possible function of ambient wind speeds in self-cleaning processes suggest that while smaller resuspension velocities are required for large particles, wind may be able to clean them more successfully than small particles (Jiang *et al.*, 2018). Cleaning methods are broadly classified as natural cleaning, mechanical cleaning, self-cleaning coating, and electrostatic removal method (Luque *et al.*, 2018). Natural cleaning entails using natural forces to remove dust, such as wind power, gravity, and the scour of rain water. Brushes, vibrating, and ultrasonic driving are used in mechanical methods to remove dust from the module's surface. Cleaning PV modules by hand is a labor-intensive and time taking process that can also lead to surface cracking from harsh brushing, which further deteriorates PV performance. Furthermore, because manual cleaning is ineffective at removing very small particles, researches are advocating for self-cleaning PV panel surface cleaning techniques, such as PV surface coating, electrostatic, and mechanical methods (Syafiq *et al.*, 2018).

Protecting substrates from external influences can be achieved by applying coatings, which change surface qualities such as adhesion, wettability, corrosion resistance, and wear resistance. Low surface energy materials such as silanes, silicones, nanoparticles, and polymers are employed for hydrophobic surfaces due to their water-repellent characteristics (Al-Badra *et al.*, 2020; Syafiq *et al., 2018).* High surface energy materials with good wettability properties are needed to develop highly hydrophilic surfaces. Super hydrophobic surfaces self-clean by utilizing ambient air or rolling droplets, which lowers pollutants through photocatalysis. The coating technique provides a low-maintenance, low-energy, and eco-friendly means

of achieving natural self-cleaning properties (Al-Badra *et al.*, 2020; Thongsuwan *et al.*, 2022). Hydrophobized meshes are used to cover PV cell surfaces because hydrophilizing PV cell surfaces decreases optical transmittance. This reduces the hydrophobized coating's coverage area over the cell surfaces. Rolling droplets, according to study results, decrease dust from hydrophobic mesh-laid photovoltaic cell surfaces without leaving droplet fluid residues on the surfaces, therefore lessening the effect of reduced optical transmittance (Yilbas *et al.*, 2021). Nevertheless, using a vibrating system with coatings can improve solar cells' performance even though the effects of vibration on them are still unknown. The frequency of dust removal from the surface of a solar module is decreased from four times per month for an uncoated module to two times per month for a coated module, despite the fact that the coating does not repel dust (Al-Badra *et al.*, 2020). Though many academics have suggested coating techniques, these models still have certain drawbacks when it comes to cleaning solar modules and concentrators. For example, water (or rain) and UV light radiation (wavelength less than 380 nm) are essential for photoactive coatings to activate the surface. Similarly, the surface durability of super-hydrophobic coatings cannot endure prolonged outdoor exposure beyond a few months (Syafiq *et al.*, 2018).

When particles of the same polarity re-suspend in the air, the attraction force intensifies the density of the dust deposition (Al-Salaymeh *et al.*, 2023). To address the issue of dust accumulation on PV modules, researchers recommend using an electrostatic ionizer. By using air ionizers to neutralize the static electricity on products, equipment, and surfaces, electrostatic cleaning techniques eliminate the accumulation of static charges on non-conductors on surfaces. Positive and negative ions from the air ionizers are released into the environment and attract other ions with the opposite polarity that are present on a charged surface (Al-Salaymeh *et al.*, 2023; Yosri *et al.*, 2018). The concept behind electrostatic cleaning is that high-voltage polyphase waveforms at various frequencies are produced by a process that needs an AC voltage to transport dust particles over the surface of the solar panel. Charged particles are kept from leaving the solar panel's surface and follow the electric fields when the right frequency and amplitude requirements are satisfied

(Syafiq *et al.*, 2018). Despite its seeming promise, electrostatic cleaning is not without its difficulties. The electrostatic method requires power to produce triboelectric charging and dielectric forces on parallel electrodes, commonly wire and copper electrodes, in order to repel dust at low pressure. Similarly, large-scale photovoltaic panels cannot be supported by electrostatic cleaning, nor is it useful on wet days (Al-Salaymeh *et al.*, 2023; Ngwashi & Tsafack, 2023; Syafiq *et al*., 2018).

Mechanical cleaning methods are difficult and labor-intensive because most solar power plants have an array of modules mounted high above the ground or on roofs, which puts both human and module safety at risk. A mop or wipers with the proper support structures must be used by the operator to physically clean the surface during the cleaning procedure (Rane, 2019). Using a vacuum cleaner helps lessen the chance of damaged PV modules. A vacuum cleaner can clean the PV surface fully, except for the corners of the modules, which require hand cleaning. In order to collect dust and debris from the PV surfaces, the vacuum suction cleaner works by using an air pump to generate a partial vacuum. The electrical supply powers the vacuum cleaner's motor, which generates suction pressure. But since the operator will inevitably come into contact with the vacuum cleaner physically, proper training is required. Dust buildup and scratches eventually cause the sun's insolation to be absorbed inefficiently (Hudedmani *et al*., 2017).

When compared to alternative mechanical methods, air-blowing from an air conditioning system has a number of benefits, including cleaning the PV module, cooling it, and leaving no micro-scratches on its surfaces. Power is needed for mechanical techniques to move wipers, spray nozzles, and cleaning robots on photovoltaic panels. Similarly, certain cleaning systems use a lot of energy to clear dust and other material from solar panels. In addition, the cleaning system's input power requirements may exceed the actual output power generated by the solar PV modules, which could cause performance problems and raise doubts about the system's financial sustainability (Jaiganesh *et al*., 2022). The fact that regular maintenance is impossible for manual cleaning systems due to high labor costs is another drawback.

2.2.10 Normalizing Equations for Output Parameters

Variation in ambient conditions necessitates the need to normalize key parameters in determining PV module performance. For example, the variation in solar irradiance and ambient temperature over time complicates the modalities of PV module comparison across different study sites. Similarly, the extent of soiling on PV module performance must be referenced to a point, hence the need for the soiling loss factor, SL_{φ}. The soiling loss factor, SL_{φ}, is calculated by comparing the output parameters of a dusty module to those of a regularly cleaned one using Eqn. 2.15 (Hachicha *et al*., 2019);

$$SL_{\varphi} = \left\{\frac{\varphi_{clean} - \varphi_{dusty}}{\varphi_{clean}}\right\} - \Phi_{Ref} \qquad 2.15$$

where φ_{clean} represents the electrical parameters at a referenced clean condition, φ_{dusty} is the electrical parameters of the same module exposed to dust and Φ_{Ref} represents degradation rate of site-specific reference module installed beside the study modules but cleaned regularly. The degradation rate, Φ_{Ref}, is determined through the calculation of the degradation factor of the electrical parameters of the reference solar module over the study period. Eqn. 2.15 represents a modified soiling loss factor equation discussed by Lin *et al.* (2020). The modification is intended to isolate the effect of soiling on the PV modules.

The variance in power, η_P, current, η_I and voltage, η_V from soiled to clean conditions can respectively be obtained from Eqns. 2.16 to 2.18 (Hachicha *et al*., 2019);

$$\eta_P = \left(\frac{P_{shade} - P_{max}}{P_{max}}\right) \times 100\% \qquad 2.16$$

$$\eta_I = \left(\frac{I_{shade} - I_{MPP}}{I_{MPP}}\right) \times 100\% \qquad 2.17$$

$$\eta_V = \left(\frac{V_{shade} - V_{MPP}}{V_{MPP}}\right) \times 100\% \qquad 2.18$$

where P_{max}, I_{MPP} and V_{MPP} represents the maximum power, current and voltage at maximum power of a clean PV module and P_{shade} , I_{shade} and V_{shade} represents the

maximum power, current and voltage at maximum power of the same PV module under soiled conditions (Ramgolam & Soyjaudah, 2018). The temperature effect on the voltage parameters at P_{max} are quantified and normalized by the temperature coefficient T_C of V_{MPP} ($T_{C,V_{MPP}}$) from Eqn. 2.19 (Ndeto *et al.*, 2020);

$$T_{C,V_{MPP}} = \left(\frac{\frac{V_{MPP_1} - V_{MPP_2}}{V_{MPP_2}}}{T_1 - T_2} \right) \qquad 2.19$$

where V_{MPP_1} and V_{MPP_2} are the PV module's voltage at maximum power point immediately after exposure to sunlight and after taking the I-V characteristic measurements, respectively, and T_1 and T_2 are the PV module's temperature at V_{MPP_1} and V_{MPP_2} in degree Celsius (^oC), respectively.

2.3 Previous Works Relevant to Study

The ability of the glass cover to transmit radiation to the solar cells greatly influences the performance of a PV module. The accumulation of dust on the surface of PV modules is one of the causes of gradual degradation of transmittance. Elminir *et al*. (2006) investigated the rate at which desert dust degrades the output parameters of unattended PV modules. The reduction in transmission of the normal glass cover was found to be strongly dependent on the dust deposition density, tilt angle, and surface orientation with respect to the wind direction. Further examination revealed that the dust deposition density ranged from 15.84 g/m^2 to 4.48 g/m^2, corresponding to a 52.54% to 12.38% decrease in normal glass transmittance. A significant decrease in glass transmittance was observed at a tilt angle of 15^o and an orientation of 45^o degrees from the north (Elminir *et al*., 2006) although the correlation between dust deposits and relative humidity was missing.

Mani *et al.* (2010) acknowledged that the installation of PV system for optimum performance is primarily dictated by its geographic (latitude and available solar insolation), location and installation design (tilt, orientation and altitude). In addition to these conditions, there are other factors determining the system performance. Among these factors, dust is lesser acknowledged factor that significantly affects the

performance of the PV module (Mani & Pillai, 2010). Similarly, Mani *et al.* (2010) proposed additional research on determining the properties (optical, size, geometry, and electrostatic deposition behavior) of natural dust. This is because most experimental studies focused on the accumulation of simulated artificial dust, biological and electro-chemical properties of dust on their deposition behavior for various environmental conditions. These environmental conditions included vegetation type, built environment, and climates. An optimization study for various geographical and climatic conditions was also proposed, taking into account optimum fixed tilt, altitude, and orientation for solar gain, prevalent wind pattern, and minimum dust accumulation (Mani & Pillai, 2010).

Due to heavy soiling on the module's glass surface, Schill *et al.* (2015) discovered a significant decrease in PV module efficiency. These tests were conducted on Gran Canary Island, located in the Atlantic Ocean west of Morocco. The module's efficiency had dropped to 20% of its initial values within 5 months of the study. During the study period, a light rain caused partial shading of solar cells in the module's lower cell rows. This was due to the fact that the rain water did not completely wash away the dust, which accumulated in the lower area of the inclined modules (Schill *et al.*, 2015).

Maghami *et al*. (2016) distinguished two types of shading: soft shading and hard shading. Soft shading was defined by materials such as smog accumulation in the air, whereas hard shading was defined by dust accumulation in the PV module, which blocked the light rays incident on the PV module. Soft shading had an effect on the current of the PV module, but the voltage remained constant. In the case of hard shading, the performance of the PV module was determined by whether all or some of the cells were shaded. This type of shading was found to reduce voltage in general. The study concluded that the amount of dust accumulated on the surface of the PV module affected the overall energy delivered by the module. Further investigation revealed that the soil accumulated on the solar panels was characterized by two parameters: dust property and local environment although the characterization of dust property in relation to soiling effect was not done (Maghami *et al.*, 2016).

In a study conducted in Santiago, Chile, Besson *et al.* (2017) investigated the seasonality of soil accumulated on a PV module. The study's findings, which quantified the various temporal soiling losses that occurred during the study, demonstrated that soiling rates are seasonal. In the absence of rain, soiling rate values during the winter months were as low as 0.83%/day; in the summer, they were closer to 0.19%/day. The findings were used to construct a yearly soiling trend that may help reduce uncertainty in the estimation of energy yield. The seasonal soiling phenomena was associated with the year-round variation in particulate matter in the air, with wintertime concentrations of $PM_{2.5}$ and PM_{10} being noticeably higher than summertime levels. To evaluate and quantify this relationship, additional research is required (Besson *et al.*, 2017).

Based on 44 months of data, Tabatabaei *et al*. (2017) found an average degradation rate of 0.923%/year for 23 PV systems installed in a house in the Netherlands, with a minimum rate of 0.305%/year and a maximum rate of 1.348%/year. The rate of degradation was found to be faster on panels located near growing trees (growing trees makes longer shadows overtime). More research on field PV systems and the performance of domestic PV modules was suggested for future work (Tabatabaei *et al.*, 2017).

Jiang *et al.* (2017) used the particle resuspension method to investigate the wind cleaning process on deposited particles on the PV surface. The study's findings revealed that large particles could be effectively cleaned by wind due to the particles' low required resuspension velocity when compared to small particles. The minimum required shear velocity for particle resuspension was discovered to range from 0.23 m/s to 57.56 m/s for various particle sizes and increased with particle diameter (Jiang *et al.*, 2017). The study's limitation was that the analysis of dust particle resuspension was done on a horizontal flat surface, whereas PV modules in the field are optimized through a specific tilt angle and orientation. Furthermore, the limitation of having unclear deductions on the relationship between the free stream velocity and the actual velocity on inclined flat PV modules was acknowledged (Jiang *et al.*, 2017).

Lu *et al*. (2018) investigated the deposition of dust particles on PV modules. Dust deposition rates were significantly higher for upwind PV installations compared to downwind installations, and this was further influenced by PV installation angle. When the PV modules were more horizontal to the ground, dust deposition was greater. Peak deposition rates were also observed to be 14.28%, 13.53%, 6.79%, and 9.73% for tilt angles of 25^{o}, 40^{o}, 140^{o}, and 155^{o}, respectively, with maximum deposition rates appearing for dust particles with a diameter of 150 μm. A further observation revealed that the majority of the dust deposited on the solar PV modules was caused by a significant gravitational effect on large particles. When the dust particle size increased, the rate of deposition increased at first, then decreased. The orientation of upwind PV systems had an additional effect on the increased rate of dust deposition (Lu & Zhao, 2018). In addition, Lu *et al*. (2018) discovered that the diameters of dust particles and the angles at which PV panels were installed had a significant impact on solar PV efficiency. PV efficiency reduction ratios of 36.17%, 35.04%, 19.03%, and 25.86% were observed for cases of $\theta = 25^{o}$, 40^{o}, 140^{o}, and 155^{o}, respectively. It was also suggested that a study on dust deposition and related experimental studies be conducted to validate and supplement the findings (Lu & Zhao, 2018).

Wang *et al*. (2019) investigated the change in aggregate size distribution of wind-blown sediments with wind speed for loamy, sandy, and sandy loam soils in Northern China's Bashang District. With increasing wind speeds, the geometric mean diameter of sediments increased exponentially. It was also noted that field measurements confirming the effect of wind speed on the particle size distribution of wind-blown sediments were insufficient, and thus an analysis of the soil aggregate size distribution of wind sediments required wind speed consideration (Wang *et al.*, 2019).

Finally, Isaifan *et al*. (2019) presented a theoretical and experimental investigation of the adhesion forces that govern the mechanisms of bonding between dust and PV surfaces. Capillary, van der Waal, electrostatic, and gravitational forces were the four fundamental adhesive forces studied. Under relatively high humidity, capillary force dominated with 98% of the total forces, whereas van der Waal forces dominated

under dry conditions. The adhesive forces were not significantly reduced when the surface roughness was increased from clean glass to coated glass (Isaifan *et al.*, 2019).

2.4 Summary of Research Gaps

Some existing gaps have been identified from the previous researches on the effect of wind speeds on dust deposition patterns and its effect on PV modules. For instance, the correlation between the effects of wind speed on aggregate size distribution of wind-blown sediments and dust particle resuspension on optimized modules is inadequately discussed. Similarly, the effect of altitude, geographical location, module siting and climatic conditions on dust particle deposition and accumulation appears blurred (Jiang *et al.*, 2018; Lu & Zhao, 2018; Mani & Pillai, 2010; Wang *et al.*, 2019). Furthermore, the effect of the different types of dust (i.e., geogenic, biogenic and anthropogenic) on PV output parameters has been scantly and inconclusively discussed. Taking advantage of the aforementioned gaps, this research sought to determine the effect of wind speeds on particulate distribution of wind-blown sediments, dust composition on installed PV modules, module altitude, orientation and wind direction. Similarly, the effects of the various categories of dust on PV modules were also scrutinized. The viability of ambient wind speeds naturally fully dislodging adhered dust particles from the PV module surfaces were also investigated. The study's findings aided in analyzing the performance of silicon mono-crystalline PV modules under shading conditions in varying wind speeds, installation height, and optimal tilt angle. In addition, the study finding aided in the design and testing of an automated self-powered cleaning model for cleaning the dusty PV module surfaces.

CHAPTER THREE

MATERIALS AND METHODS

3.1.Introduction

This chapter discusses the methods that were used to collect, analyze, and present data. The outdoor experimental setups at Typical Module Operating Temperatures (TMOT) and the data acquisition procedures are discussed. The performance of a mono-crystalline silicon PV module (m-Si) under soiling conditions with varying wind speeds and relative humidity is investigated. Similarly, an outdoor experimental setup is presented for analyzing aeolian dust distribution, elemental concentration, characteristics, and their effects on the performance of crystalline silicon solar cells in five different locations. The design, fabrication and operation procedures for an automated self-cleaning model for cleaning dusty PV modules are discussed.

3.2.Research Design

This research employed inferential study design where quantitative research method was used in actualizing the research objectives. Experimental and correlational approaches in research were used in data collection and analysis, respectively. The research comprised of preliminary data collection for a period of three months where the study equipment were mounted and a test-run performed. Concurrently, a feasibility research study of five sites based on location, background soil type and proximity to different sources of ambient dust in Machakos County was conducted. Machakos County presents a perfect representation of the climatic conditions and soil types found in Kenya hence the choice. Thereafter, outdoor experimental studies on sampled solar PV systems installed in Machakos County as well as a conceptual analysis of the results were done. The obtained results were subjected to a quantitative analysis to determine the performance of mono-crystalline silicon PV modules under shading conditions in Machakos County at varying wind speeds, installation heights, and optimal tilting. Finally, the research findings aided in the design, fabrication and testing of automated PV surface self-cleaning system.

3.3.Study Area

The field setups and experiments were stationed in five selected sites in Machakos County while the laboratory setups were done at Jomo Kenyatta University of Agriculture and Technology (JKUAT) Physics laboratory and Multimedia University of Kenya Renewable Energy Research Consortium (MMU-RERC). The collected dust samples were analyzed at the International Centre for Research in Agro-forestry (ICRAF) laboratories.

3.4.Sampling Techniques

A multistage sampling technique was used to select a sample of solar PV systems for study. The first stage of the sample approach involved determining the most recently installed and commissioned PV systems in Machakos County as part of the Solar Water Project (SWP) spearheaded by the Machakos County Government. Following that, Machakos County was divided into clusters (sub-counties), with a sample of PV systems assessed in each. The second stage included selecting a proportionate sample from the total number of installed solar PV systems depending on the size of the installed system in terms of yield (CM/HR), with at least one representative from each sub-county whenever it was applicable.

Machakos County is divided into eight sub-counties: Masinga, Yatta, Kangundo, Matungulu, Kathiani, Mavoko, Machakos Town, and Mwala. Wards are part of these sub-counties. According to the Machakos County Government's annual report (2018), 24 solar water projects were installed and commissioned for use on November 13th, 2018 in various sub-counties. Table 3.1 summarizes the installed PV systems and their locations.

Table 3.1: Installed PV systems for SWP in Machakos County (Annual Report, 2018)

Sub-County	Borehole	Ward	Location	Yield (Cm/Hr)	Latitude	Longitude
Machakos Town	Kasaini BH	Mutituni	Kivutini	2.3	-1.399025	37.241084
	Mithini comm.	Mutituni	Nzoweni	8.1	-1.44948	37.249375
	School for the Blind	Muvuti	Muthini	1.8	-1.52484	37.272819
	Mikuini Sec.	Muvuti	Kivandini	2.1	-1.514767	37.322863
	Tumba	Mumbuni North	Mumbuni	3.0	-1.502873	37.262986
	Kyangala Sec.	Kalama	Kyangala	1.2	-1.62823	37.336636
Mwala	Kwelita	Mbiuni	Itikoni	2.8	-1.21972	37.401315
	Muthwani Pri.	Mbiuni	Muthwani	8.2	-1.215245	37.375195
	Yathooko	Mwala	Mwala	3.5	-1.33891	37.43444
	Ikumini	Mwala	Nguluni	1.2	-1.291623	37.48802
	Mikuyuni Sec	Kibauni	Kivandini	2.5	-1.515109	37.624198
	Kitile Sec.	Kibauni	Kitile	1.0	-1.47209	37.645793
	Wakaela Sec.	Wamunyu	Kambiti	0.9	-1.385337	37.601607
Masinga	Muthithu	Kivaa	Eendau	2.0	-0.988325	37.483656
	Kangonde Comm.	Masinga Central	Kangonde	8.5	-1.07515	37.678138
	Kathukini Mkt	Muthesya	Kathukini	3.8	-0.990521	37.410267
	Militani	Muthesya	Milaani	7.9	-0.90445	37.390986
Yatta	Mathingau	Ikombe	Mathingau	7.2	-1.2248952	37.463952
	Kalyambeu	Ikombe	Kitheuni	2.1	-1.2979533	37.813039
Kangundo	Mukunike	Kangundo West	Mukunike	2.8	-1.332009	37.276645
	Kwa Kithama		Kyevaluki	2.6	-1.388053	37.358135
Matungulu	New Ngathu	Matungulu West	Mbuni	3.5	-1.217245	37.316154
	Kiboko Sec.	Matungulu North	Kiboko	7.8	-1.097521	37.272844
Kathiani	Kalikya B	Mitaboni	Mitaboni	0.5	-1.371602	37.272097

From the data presented in Table 3.1, a proportionate sample was determined from the total PV systems installed in each sub county. A summary of the sample size is presented in Table 3.2.

Table 3.2: Installed PV Systems and Proportionate Sample Size

Sub County	Installed PV Systems	Selected Sample Size	Site Code	Yield Cm/Hr	Location
Machakos Town	6	1	Site 1	8.1	(-1.449, 37.249)
				3.0	(-1.503, 37.263)
Mwala	7	1	Site 2	8.2	(-1.215, 37.375)
				3.5	(-1.339, 37.434)
				2.5	(-1.515, 37.624)
Masinga	4			8.5	(-1.075, 37.678)
				3.8	(-0.991, 37.410)
				7.9	(-0.904, 37.391)
Yatta	2	1	Site 3	7.2	(-1.225, 37.464)
Kangundo	2	1	Site 4	2.8	(-1.332, 37.277)
Matungulu	2			3.5	(-1.217, 37.316)
		1	Site 5	7.8	(-1.098, 37.273)
Total	**24**	**5**			

Five study sites were selected from the six sub-counties listed in Table 3-2. The selection of the sites was informed by the location, soil type, pre-existing stand-alone solar PV systems which would offer support structures for the study modules and compliance to the Kenya Bureau of Standards (KEBS) guidelines. Similarly, the security of the study equipment was also a determining factor. Figure 3.1 shows the geographical location of the study sites.

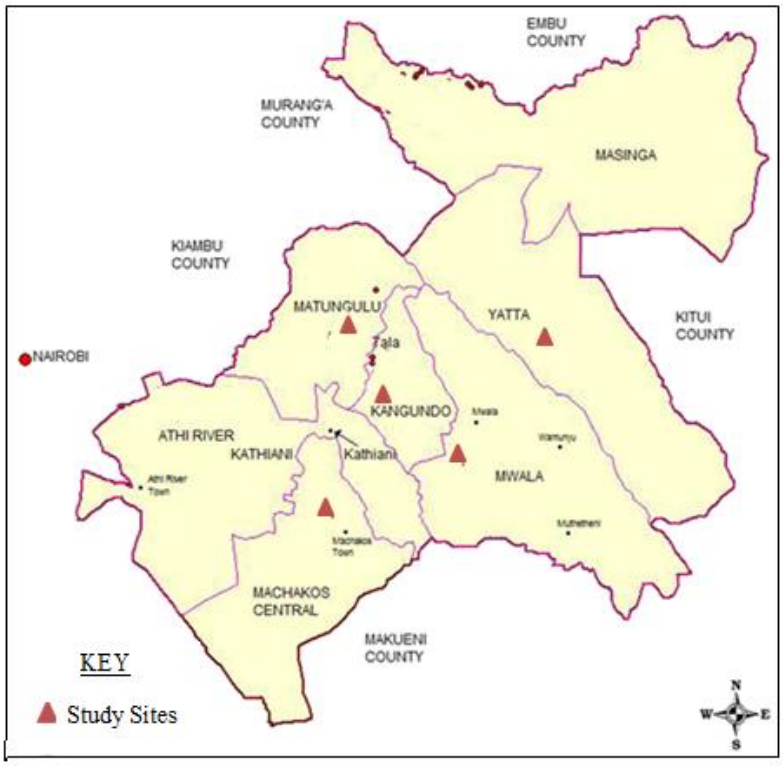

Figure 3.1: Regional Map of Machakos County, Kenya

Machakos County has five major soil types: alfisols, acrisols, ferrasols, vertisols, and andasols (Omuto, 2013). Alfisols and acrisols are brown to reddish brown in color and are classified as sandy loams to loamy sandy. They are friable and well-drained. They have low inherent fertility, low water retention capacity, low organic matter content, and high erodibility. Ferrasols are light-textured, strongly leached, permeable soils found on undulating uplands and plateaus that are relatively less prone to erosion. Vertisols, also known as black cotton soils, are low lying flat lands and plateaus with cracking clays with low water permeability and high-water holding capacity. Finally, andasols have good physical properties, are moderately fertile, and can be found on steep slopes (*Machakos District Environmental Action Plan 2009-2013*). The availability of the five soil types within the county formed the basis for the selection of the study sites.

3.5.Experimental Procedures

Experiments were carried out outdoors under ambient conditions in accordance to the International Electro-technical Commissions' standards under normalized Standard Testing Conditions (STC) and Typical Module Operating Temperatures (TMOT) (IEC TS 62257-9). According to IEC testing specifications, the Standard Test Conditions are set at 1000 W/m^2, 25 ^{o}C, A.M of 1.5, while the Typical Module Operating Temperatures are set at 50 ^{o}C (IEC, 2016). During the study period, the ambient temperatures, irradiance, wind speeds, and humidity were all measured. The module siting, which includes module installation height, tilt angle, and orientation, was varied in order to determine its contribution to dust deposition rates. Prior to data analysis and curation, the output parameters were normalized to STC and TMOT conditions due to the intermitted nature of the incident irradiation and ambient temperature. For elemental analysis, dust and soil samples collected from the research sites were submitted to the International Centre for Research in Agro-forestry (ICRAF). The samples were examined using infrared (IR) spectroscopy and portable X-ray fluorescence (PXRF), which is based on energy dispersive X-ray fluorescence (EDXRF) technology and uses X-ray tubes as the excitation source.

3.5.1 Site Specific Irradiation, Wind Speeds and Direction, Module Installation Height, Tilt Angle and Orientation

The outdoor experiments were conducted at five existing solar PV installation sites in Machakos County, Kenya. The study sites were chosen based on environmental conditions, location, topography, soil type, and output yield, resulting in a more conclusive site comparison between PV modules under similar ambient conditions. In the selected study sites, a preliminary study of the ambient conditions was carried out. The study sites' Global Positioning System (GPS) coordinates were identified and used to map the study sites. Over a seven-year period, GPS coordinates were used to retrieve site-specific average monthly Global Horizontal Insolation (GHI) data from the European Commission Joint Research Center's PVGIS-5 geo-temporal irradiation databases (PVGIS-CMAF and PVGIS-SARAH) (2010-2017).

The existing PV system siting conditions on which the study experiments would be based were analyzed. Eqn. 3.1 was used to calculate the module height (h) from Figure 3.2, where the dimensions were measured with a tape measure with an accuracy of ± 0.1 and the tilt angle (α) was determined using a TRI-SEN PV analyzer with an accuracy of ± 0.01. A survey of pre-existing ground mounted solar PV systems and their compliance with Kenya Bureau of Standards (KEBS) installation guidelines, which advocate for a minimum installation height of 1.5 m for ground mount PV systems, informed the variation in module installation height. Figure 3.2 illustrates the installation design of the ground mounted solar PV system.

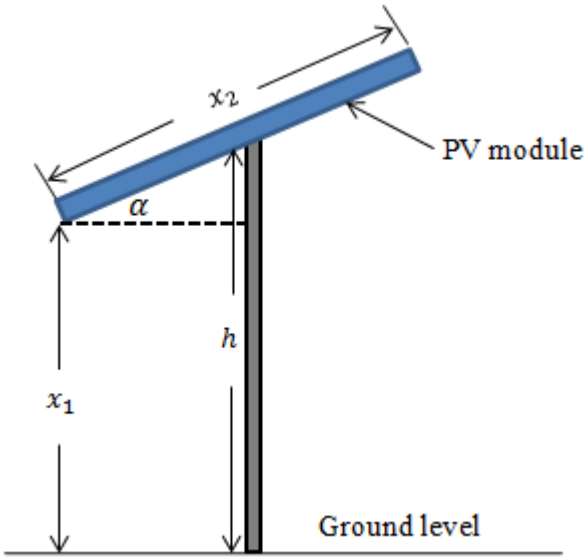

Figure 3.2: Ground Mounted Solar PV System.

The module installation height *h* presented in Figure 3.2 is a factor of module array width and the tilt angle ∝ as illustrated in Eqn. 3.1;

$$h = x_1 + \frac{x_2}{2}\sin \propto \qquad 3.1$$

where x_1 is the height of the lower edge of the module, x_2 is the module array width, determined using a tape measure and α is the module tilt angle.

An azimuth compass graduated with a full circle of 360^o was used to determine the surface azimuth angle (module orientation) of the PV modules. The compass was

firmly held against the installed PV module surface to determine the magnetic north pole. The south pole was aligned with the 0^o mark of the azimuth compass, and the module orientation was determined in a clockwise direction, with 0^o, 90^o, $\pm 180^o$ and -90^o indicating South, West, North, and East facing, respectively. A similar procedure was followed at each site taking into account that the orientation of solar PV systems as well as the inclination was predetermined.

For two weeks, preliminary wind directions and speeds were measured at each site at one-second intervals using a wind vane and a digital anemometer with an accuracy of ±0.1. The data were then correlated with Kenya Meteorological Department (KMD) data that was obtained from KMD stations in Machakos County. Upon observing a strong link between the field data and KMD data, KMD data was utilized to examine wind directions, speeds, and patterns as well as relative humidity for every one of the five sites. Before the actual data collection process began, preliminary data was collected for one month with the aim of monitoring, testing the reliability of the measuring instrument, and rectification of field setups. Data collection for irradiance, module temperature, current-voltage parameters, wind speeds, and ambient temperatures was done every two weeks. The actual data collection period lasted seven months, following which data analysis began.

3.5.2 The Rate of Dust Accumulation and its Effect on the Current and Voltage Parameters of m-Si Solar Modules in the Five Selected Sites

The observed topographical and environmental differences in the selected study sites warranted for a site-specific dust deposition rate analysis. It is obvious that modules exposed to ambient conditions will accumulate dust on their surfaces over time. Since dust is a key factor in PV module soiling, its settlement pattern has a significant impact on the performance of field-installed PV systems.

In order to achieve the goals of the research, the following tools were used. TRI-KA PV analyzer (accuracy of ± 0.01.), TRI-SEN PV analyzer (accuracy of ± 0.01.), Solar power meter (accuracy of ± 1.0 W/m^2), high precision digital electronic beam balance (accuracy of ± 0.01 g), fifteen connecting cords/wires and a data logger. Similarly, five dust deposit glass sheets measuring 100 mm by 50 mm, ten 10 W 18

V Solar Max m-Si PV modules and five 360 mm by 530 mm rectangular soft iron casing for shielding the PV modules from undesired geomagnetic fields were also used.

In the five study sites, ultra-thin glass sheets (100 mm by 50 mm) were fixed alongside cleaned pre-existing modules for dust deposition rate analysis. To avoid irregular deposition patterns accelerated by pre-existing dust particles on the PV surfaces, the PV modules previously installed at the sites were cleaned before data collection began. The glass sheets were installed alongside the PV modules at a site-specific inclination and azimuth angle (depending on the fixed module at the site). The initial masses of the glass sheets were determined as m_o. Subsequent masses of the glass sheets were determined every month for seven months using a high precision digital electronic beam balance, and recorded as m_n where n represents the measurement frequency (n = 1,2,3,4.....). The mass of the dust deposits was obtained from Eqn. 3.2;

$$m_{dust} = m_n - m_o$$

The degradation rate was determined by the quotient of Eqn. 3.2 and the exposure duration. Similarly, real-time data on rainfall patterns over the course of the study were collected from meteorological departments near the study sites.

Concurrently, two 10 W, 18 V (V_{MPP}) mono-crystalline solar modules were installed alongside the existing PV system at the same siting conditions as shown in Figure 3.3 .One module served as the reference module and was regularly cleaned, while the other was left unattended for comparison purposes.

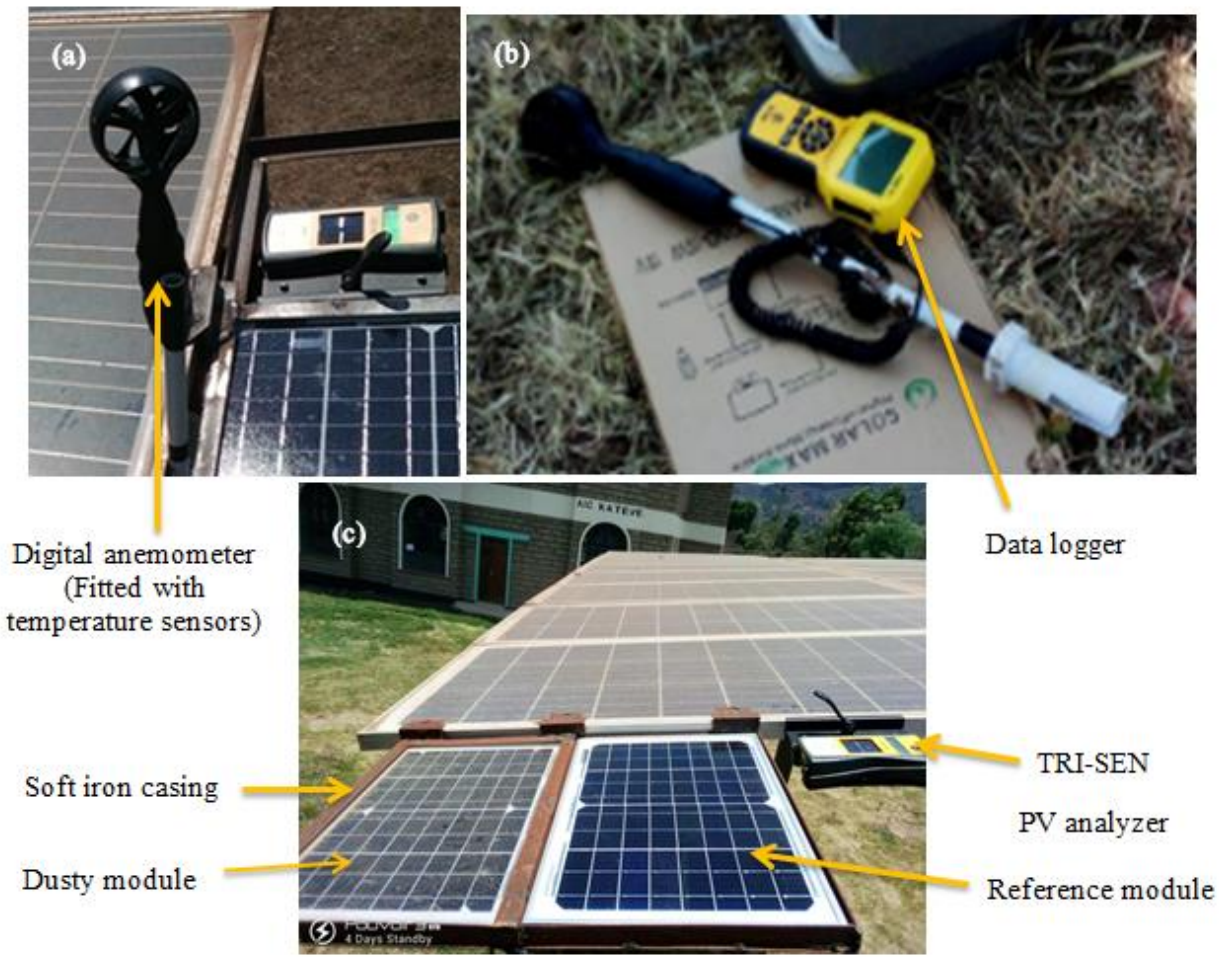

Figure 3.3: Outdoor Experimental Setup: (a) Wind Speeds and Ambient Temperature Sensors, (b) Data Logger and, (c) Shielded PV Module Study Setup alongside Pre-existing PV System.

The initial current and voltage data for the study PV modules were determined by the TRI-KA PV analyzer, on the other hand, the TRI-SEN PV analyser determined the study modules' irradiance, module temperature, and tilt angle during the data collection intervals. Solar irradiance was measured during the study period using a solar power meter which was positioned next to the module and had the same inclination and orientation. The real-time solar irradiance values provided by the solar power meter helped to synchronize the highest irradiance with the TRI-KA PV analyzer's commencement of data collection for 30 seconds per dataset.

The dusty modules' current-voltage parameters were compared to those of regularly cleaned modules installed alongside the dusty ones (Figure 3.3), and the difference was noted for further investigation. The soiling rate, overall effect on PV parameters, and temperature effects on m-Si PV modules were calculated using Eqns. 2.15 - 2.19. As a result, it was ascertained that determining the impact of installation height, tilt, and orientation on dust deposition rates was crucial.

3.5.3 Effect of Module Height, Tilt Angle and Orientation in Southerly Winds to the Overall Dust Deposition Patterns

One of the five sites was chosen for dust deposition rate analysis at various module height, tilt, and orientation. The chosen study site was distinguished by the presence of extensive ground cover and the absence of all-weather roads surrounding the study area. These factors ensured that any field-installed PV system would have the lowest possible dust deposition rates (Sayyah *et al*., 2014), thus assuring the fundamental effects of dust deposition rates at various installation heights, tilts, and orientations. Similarly, the study sites' proximity to the equator provides minimal variation in the effect of orientation (north or south facing) on PV performance at nearly horizontal tilt (Matius *et al*., 2021). On the other hand, the module orientation was of interest in terms of dust deposition rates at specific wind speeds and directions. As a result, there was a need to investigate the deposition rates at different heights, tilts, and orientations (both north and south facing) in relation to wind profile.

Ultra-thin glass sheets measuring 157 mm by 69 mm were installed at three different heights (1.5 m, 2.0 m, and 2.5 m) with tilt angles of 5^{o}, 10^{o}, and 15^{o} at each height. Similarly, because modules are oriented facing either north or south depending on their geographic location in relation to the equator, the glass sheets were also oriented north and south for each study height and tilt angle (Matius *et al*., 2021). Figure 3.4 depicts the installation of the field setup as per the KEBS PV installation guidelines (KEBS, 2018).

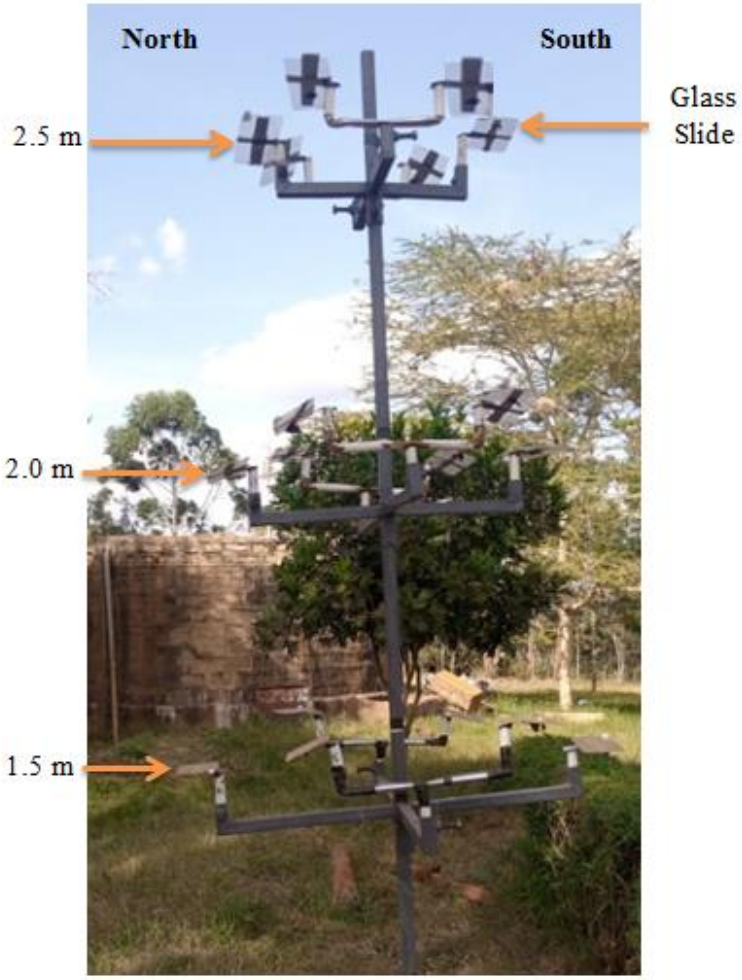

Figure 3.4: Actual Field Dust Deposition Sampling Setup at Varying Height (1.5 m, 2.0 m and 2.5 m), Tilt Angle (5^o, 10^o and 15^o) and Orientation (north or south facing).

To mitigate the impact of wind on the equilibrium position of the glass sheets, the masses of the glass sheets were determined using an external high precision digital scale housed in a glass container. The masses (m_n) of the glass sheets were determined on a weekly basis for duration of 5 weeks. The masses of the dust deposits were then calculated using Eqn. 3.1 from the difference between m_n and m_o.

3.5.4 Characterization of the Accumulated Dust Particles on PV Modules at Site Specific Inclination and Azimuth Angle and Subsequent Effect on the Conversion Efficiency of m-Si PV Modules in the Selected Sites

3.5.4.1 Elemental Analysis of Dust and Soil Samples

Pre-existing PV modules were used as bulk dust collection sites for a larger volume of dust intended for particulate size analysis at the International Centre for Research in Argo-forestry (ICRAF). This was informed by their expanse surfaces which would collect a larger volume of dust particles within a short duration of time. The dust samples were collected on a monthly basis for seven months and thereafter the dust and some background soil samples from each site were presented to ICRAF for elemental analysis.

The International Centre for Research in Agroforestry (ICRAF) received dust and soil samples from the study sites for elemental analysis. The samples were analyzed using Portable X-ray Fluorescence (PXRF) technology, which is based on energy dispersive X-ray fluorescence (EDXRF) technology and employs X-ray tubes as the excitation source, as well as an infrared (IR) spectroscopy technique combined with machine learning (ML). The computer can recognize and study patterns using ML without being explicitly monitored or controlled by humans (Apt, 2003). Similarly, in the X-ray fluorescence process, emitted photons interact with the atoms in the sample, causing an electron to be "knocked out" of the inner shell of a given atom, resulting in an unstable shell. The electron's empty space is filled by another electron from a higher shell, releasing energy (Fluorescence) in the form of photons, which is unique to each element and shell transition. X-ray Fluorescence instruments contain a detector that detects and identifies elements based on their characteristic fluorescent energies. Higher-energy photons generate data that can be used to quantify trace elements. Similarly, vacuum pump technology enables the rapid and simple analysis of uniform and non-uniform materials containing elements ranging from sodium to uranium.

The collected samples were air-dried and ground to pass through a 2-mm sieve before being milled to pass through a 75-micron mesh sieve. For scanning, the milled

samples were presented as loose powder in XRF (X-ray fluorescence) cups lined with Prolene film. The samples' spectral measurements were then obtained using a Bruker Invenio-S FT-IR spectrometer, which performed MIR scanning for soil organic carbon (SOC) and total nitrogen. Similarly, total elemental content was determined using the Bruker Tracer 5i pXRF. The spectra were collected in the range 7498 cm^{-1} to 599 cm^{-1}, and they were further subset during processing to work with the mid-infrared (MIR) region from 4000 cm^{-1} to 600 cm^{-1}. The obtained spectra were then projected into a spectral space for existing models to evaluate how well they were represented within the model's spectral space. The spectral space in this case consisted of 4438 visible samples near infrared spectra obtained from 785 soil profiles selected from the International Soil Reference and Information Centre's (ISRIC) Soil Information System (ISIS). Soil diffuse reflectance spectra from study sites were collected using a FieldSpec FR Spectro-radiometer (Analytical Spectral Devices, Boulder, CO) with a sampling interval of 1 nm. The reflectance readings for each wavelength band were expressed relative to the average of the white reference spectra readings and compared to ISRIC soil property attributes. Figure 3.5 depicts the prediction model using principal components analysis.

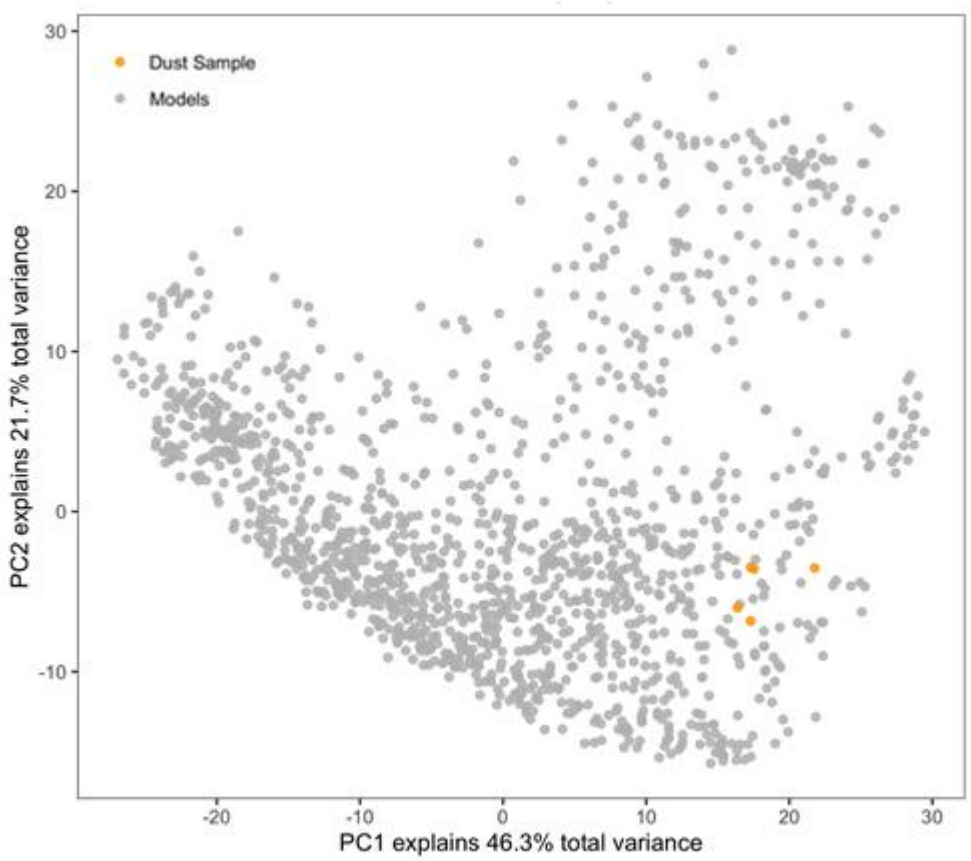

Figure 3.5: Principal Component Analysis (PCA) Scores Plot Overlaying Points from Calibration Models' Spectra and for the new ones.

The orange dust samples points were new points for soil property predictions obtained from the study sites. Approximately three-quarters of the grey points (*n* = 2040) were used to create calibration models, which were then used to predict all of the orange points. The distribution of orange points indicates that they were drawn from the same population as the samples used to construct the updated model. As a result, the predictions were accurate. Of the soil property attributes documented by ISRIC, Principle Component 1 (PC1) captures the most variation, while Principle Component 2 (PC2) captures the second most variation (Vågen *et al.*, 2020).

Finally, all of the samples' soil properties were predicted based on an acceptable high correlation co-efficient (above 0.6) between the study samples and the sample analysis calibration model. MIR predicted sample properties included soil organic carbon (SOC) and total nitrogen, while total elemental content included Na, Mg, Al,

P, S, K, Ca, Ti, Cr, Mn, Fe, Co, Ni, Cu, Zn, As, Se, Cd, and Pb. The net photon counts of detected elements were quantified using empirical calibration equations developed using soil certified reference samples with a wide range of elemental concentrations, in conjunction with appropriate instrument geometry and detector efficiency. Actual total concentration data were obtained and converted to milligrams per kilogram (mg/kg) (Gray, 2011).

Elemental analysis of the dust and soil samples was then subjected to enrichment analysis for a precise classification of the dust samples as biogenic, anthropogenic, or geogenic. Eqn.2.4 was used to calculate the dust sample enrichment factors, with aluminum serving as the reference element due to its abundance in the crustal soil across the study sites. Table 2.1 and Table 2.2 were then used to characterize the dust samples based on their enrichment level. The dust particulate radius was calculated using a range of values between the minimum and maximum particulate radius observed in the ICRAF particulate dust analysis report.

3.5.4.2 Solar PV Output Parameters

The effects of dust deposits on PV modules were determined by analyzing the I-V curves generated by the TRI-KA PV analyzer's data over the course of the study. Two 10 W, 18 V (V_{MPP}) mono-crystalline (m-Si) solar modules were installed alongside cleaned pre-existing solar PV modules at the five study sites to investigate the effect of dust deposits on the PV output parameters. The TRI-KA PV analyzer, which was connected in series with the study modules and synchronized with the TRI-SEN PV analyzer, collected the initial current-voltage data. The TRI-SEN PV analyzer determined the tilt, solar irradiance, and cell temperature of the module, whereas the TRI-KA PV analyzer determined the output current and voltage. For 7 months, current and voltage data were recorded every two weeks. Power and I-V characteristic curves were used to quantify the effects of dust accumulation on PV modules on overall performance of m-Si PV modules.

3.5.5 Design and Economic Analysis of a Model for Self-Cleaning Mechanism

3.5.5.1 Automated Self-Cleaning System

The automated self-cleaning system was designed to provide cleaning services on the dusty modules on pressing of a button. The self-cleaning system consisted of three air jets and two water jets. The air jets were generated by three identical 9 W 12 V DC brushless fans fixed in an aluminium rod. Similarly, the water jets were generated by a 4.8 A 12 V wiper motor fitted in a three-litre storage container supplied from a reservoir. In addition, a soft scouring material aimed at wiping and drying the module surface was fitted in a roller next to the air and water jets. The air and water jets acted normal to the module surface while the soft scoring pad glided on the PV surface. The air jets, water jets and scourer were fitted in a movable roller connected to pulleys attached to a bidirectional 12 V DC, 12 A power window regulator motor with a torque of 0.3 Nm and glided the cleaning components on the surface of dusty modules. The self-cleaning model was powered by a 12 V 100 Ah battery capacity which was charged by the PV module during the day. The layout of the model is presented in Figure 3-6

Figure 3-6: Automated Self-Cleaning Model

The study model was designed as shown in Figure 3.6 and tested on a dusty module before the actual data collection was performed. The study model used a 20 W Solar Gen SLG-20 solar module with a I_{MPP} and V_{MPP} of 1.22 A and 16.4 V. This was informed by the need of a 12 V DC supply to the motors and the fans in use thus the suitability of the 20 W module. The TRIKA PV analyzer recorded the solar module's current and voltage parameters prior to exposure to ambient dust, fortnightly for five months (September 2022 to January 2023) under ambient dust exposure, and immediately following the automated system's cleaning process. The time duration under which the PV module was exposed to dust was informed by favorable average daily global horizontal solar irradiance for the study site and the meteorological department's data which showed low possibility of rainfall over the study period hence maximum dust deposits. The correlation between the current-voltage data under the three conditions was done and the conclusion on the suitability of the automated self-cleaning system made.

3.5.5.1 Economic Viability of the Automated Self-Cleaning System

The assessment criteria tools such as Future Income (FI_n), Present Value (PV_n), Net Present Value (*NPV*), Profitability Index (*PI*), and amortization time can be used to calculate a project's economic viability. In determining a project's lifetime, the amount of time it takes for the majority of its components to deteriorate to the point where replacement is necessary for the project to remain economically viable (Zeraatpisheh *et al*., 2018) was defined. Based on the lifespan of the brushless motors used in the system which is estimated to be in excess of 10000 hours, the economic lifetime of the system can be estimated (Zhao & Yu, 2014). The minimal value of the motors' life expectancy can be approximated by taking into account the length of time required for a cleaning cycle, the number of cycles completed in a month, and the total number of cycles completed annually. An approximate lifespan of 10% of the projected running hours (1000 hours) was also chosen for this study, as most motors are utilized indoors and there is conflicting data regarding the rates of brushless motor degradation outdoors.

The future revenue of a project is computed from Eqn. 3.3 and is determined for each year by adding the sum of the expenses spent and the savings made, where the costs are considered negative and the savings are positive (Bernal-Agustín & Dufo-López, 2006; Rodrigues *et al.*, 2017);

$$FI_n = \sum C_n + \sum S_n \qquad 3.3$$

where FI_n, C_n and S_n represents the future income, costs incurred and savings made in year n, respectively. The costs incurred (C_n), comprises of the cost of assembling the model and the operation and maintenance (O&M) costs which include an induction training course for the staff and annual replacement cost of the scourer pad. The savings/benefits (S_n) are determined using the additional energy derived from the PV system as a result of the energy gain out of the cleaned module factoring in the annual PV module degradation rates. The cost of energy, also known as yearly electricity savings/benefits in this instance, is computed using the utility Kenya Power and Lighting Company's (KPLC) small commercial (SC) tariff, which includes all levies, adjustments, and taxes incurred for the supply of grid power. The future revenue of a given year and the deferred rates, as shown in Eqn. 3.4, are used to calculate the PV_n for year *n* as (Lima *et al.*, 2015);

$$PV_n = \frac{FI_n}{(1 + r_r)^n} \qquad 3.4$$

where FI_n is the future income for year *n* and r_r is the real discount rate determined using Eqn. 3.5 (CBK, 2024).

$$r_r = \left\{\frac{1 + r_n}{1 + I}\right\} - 1 \qquad 3.5$$

where r_n is the nominal discount rate (12.50%) and *I* is the inflation rate (6.63%) as provided by the publication of Central Bank of Kenya (CBK, 2024). The net present value (NPV) of the project is determined using Eqn. 3.6 (Jory *et al.*, 2016);

$$NPV = FI_0 + \sum_{1}^{n} PV_n \qquad 3.6$$

where FI_0 is the future income at year zero (n = 0) and PV_n is the present value of each year. A measure of the relationship between a project's expenses and profits, the profitability index (*PI*), also known as the profit investment ratio, is computed by dividing the net present value by the initial investment, as shown in Eqn. 3.7;

$$PI = -\frac{NPV}{FI_0} \qquad 3.7$$

Positive values are invariably linked to *PI*; an investment yielding a loss is indicated by a *PI* less than one, a profitable one by a *PI* more than one, and the lowest permitted return on an investment is, naturally, indicated by a *PI* equal to one (Alrikabi, 2022). The project pay-back term, or amortization time in this example, is computed using a dynamic quantity (current values) to estimate the number of years needed to achieve the breakeven point. The dynamic amortization time is calculated from Eqn.3.8 (Alrikabi, 2022).

$$Amortized\ time\ (dynamic) = -\left(\frac{FI_0}{\frac{1}{n}\sum_1^n PV_n}\right) \qquad 3.8$$

The NPV, IRR, dynamic amortized time and the *PI* values define the project's viability.

3.6.Research Materials and Equipment

The following research instruments were required for the attainment of the research objectives. Wind speed, direction and temperature sensors, TRI-KA PV analyzer (model no: X0220113242737), TRI-SEN PV analyzer (model no: X0220113242737), Solar power meter (model no: TM-206), fifteen connecting cords/wires, data logger, digital anemometer, tape measure, five dust deposit glass sheets measuring 100 mm by 50 mm, eighteen ultra-thin glass sheets measuring 157 mm by 69 mm, ten 10 W 18 V Solar Max m-Si PV modules and five 360 mm by 530 mm rectangular soft iron casing. Similarly, the automated self-cleaning model required; one 20 W 16.4 V Solar Gen-SLG-20 m-Si PV module, a 450 mm by 450 mm soft iron casing, , Chloride Exide 12 V 100 Ah battery, three 9 W 12 V DC brushless fans, one 4.8 A 12 V suction pump, a bidirectional 12 V DC 12 A power

window regulator motor (Torque of 0.30 Nm), soft scouring material, four pulleys, two 1.5 metre long bicycle chains, 3 litre rectangular storage container (450 mm by 200 mm), a 2 mm diameter pipe (5 metre long), 5 litres of water and connecting wires. Finally, the analysis of the data required Windographer, OriginPro 2018 and Grapher softwares.

3.7.Data Analysis and Processing

The distribution of wind speed and direction at a specific location was represented by a wind rose. A wind rose is made up of concentric circles that represent the various percentage frequencies of time when wind blows from a specific direction. The wind direction was given in degrees measured clockwise, with north taking 0^o, east taking 90^o, and so on. The daily maximum, minimum, and average wind speed values for the sites at different module heights were obtained, averaged, and recorded. Monthly averages of wind speed, temperature, and atmospheric pressure were also calculated and presented. The installed module's height and orientation to the wind direction were measured and recorded. The dust composition on the module, as well as the ground cover, were analyzed and presented for further deductions. The PV modules' short circuit current I_{SC}, open circuit voltage V_{OC}, power at maximum point P_{MPP}, and fill factor FF were determined and recorded. Following that, the conversion efficiency for a module optimized and exposed to soiling conditions were computed and compared to modules optimized but not exposed to soiling conditions. Thereafter, the analysis determined the soiling effect of PV modules on their conversion efficiency. The data collected were treated to a quantitative analysis using OriginPro 2018, Windographer software and Excel to determine the correlation and the effects of the data collected on the performance of m-Si solar modules exposed to ambient conditions

Finally, an automated self-cleaning model was therefore designed based on the inference made to mitigate the effects of soiling on the PV performance. Data were collected daily at the solar noon and recorded for duration of two weeks. The data was analyzed, and the power output values for the PV system were compared to the values obtained for the default PV system before cleaning.

CHAPTER FOUR

RESULTS AND DISCUSSIONS

4.1 Introduction

This chapter analyzes site specific irradiation, wind speeds and direction, modules installation height, tilt angle and orientation for the selected sites. An assessment of the rate of dust accumulation and its effect on the current and voltage parameters of m-Si solar modules is analyzed. Similarly, the effect of module height, tilt angle and orientation in southerly winds to the overall dust deposition patterns is discussed. The characteristics and constituent elements of accumulated dust particles on PV modules across the study sites at site specific inclination and azimuth angle and subsequent effect on the conversion efficiency of m-Si PV is presented. Finally, the design, testing and economic analysis of a model for self-cleaning mechanism is presented and its viability tested.

4.2 Insolation, Wind Profile, Humidity and Module Siting Analysis for the Study Sites

4.2.1 Insolation Analysis

The incident irradiance at the site and the peak rating of the PV module provided at standard testing conditions (STC) defined by AM 1.5, temperature of 25 ^{o}C, and irradiance of 1 kW/m^2, determined the energy generated from a PV module (Ramgolam & Soyjaudah, 2018). The PV module would perform optimally at an irradiance equivalent to the rated one and thus the need for a site-specific irradiance analysis. An analysis of the Daily Global Horizontal Solar Irradiance (DGHI) from the PVGIS database is presented in Table 4.1.

Table 4.1: Average Daily Global Horizontal Solar Irradiance (kW/m^2) for the study sites from the PVGIS database (2010-2017)

	Jan	Feb	March	April	May	June	July	Aug	Sep	Oct	Nov	Dec
Site 1	1.159	1.138	1.144	1.001	0.851	0.715	0.725	0.754	0.944	1.034	0.965	1.046
Site 2	1.117	1.103	1.119	1.012	0.863	0.722	0.737	0.763	0.961	1.057	0.959	1.003
Site 3	1.154	1.119	1.107	1.011	0.922	0.774	0.763	0.830	1.004	1.049	0.948	1.034
Site 4	1.152	1.121	1.110	1.021	0.935	0.761	0.764	0.792	1.000	1.046	0.950	1.025
Site 5	1.145	1.136	1.131	1.006	0.911	0.754	0.764	0.799	0.992	1.055	0.945	1.042

Observe in Table 4.1.that, all the sites received favorable and comparable irradiance levels for optimal PV module performance during the greater part of the year. Furthermore, an average irradiance of greater than 0.8 kW/m^2 would suffice to predict PV module performance under typical module operating conditions (Ramgolam & Soyjaudah, 2018). A further examination of Table 4.1.reveals that, on average, the months of September to May have higher irradiance values (above 0.8 kW/m^2), making this period ideal for analyzing the performance of solar PV modules. Contrary, the months of June, July and August registered low irradiance values owing to the position of the sun at the tropics. This low irradiance is inadequate for the analysis of solar PV modules' performance but can be backed up by battery storage in solar home systems. In general, the study sites' proximity to the equator provides good insolation year-round for PV technology. Furthermore, the study sites are in Machakos County's Arid and Semi-Arid (ASAL) regions, which experienced poor 2020 short rains (October to December) and 2021 long rains (March to May), resulting in a prolonged dry spell, according to the KMD's report.

4.2.2 Wind Profile and Humidity Analysis

The deposition, rebound, and resuspension of dust particles adhering to the PV surface are all highly dependent on wind speeds, as shown in Eqn. 2.14. The magnitude and direction of the wind incident on the PV surface greatly influence the dust deposition patterns. Similarly, surface specific drag and lift forces involved in particulate resuspension during the self-cleaning process are influenced by wind speed. Figure 4.1 depicts the wind profile across the study sites based on an analysis of wind speeds and direction.

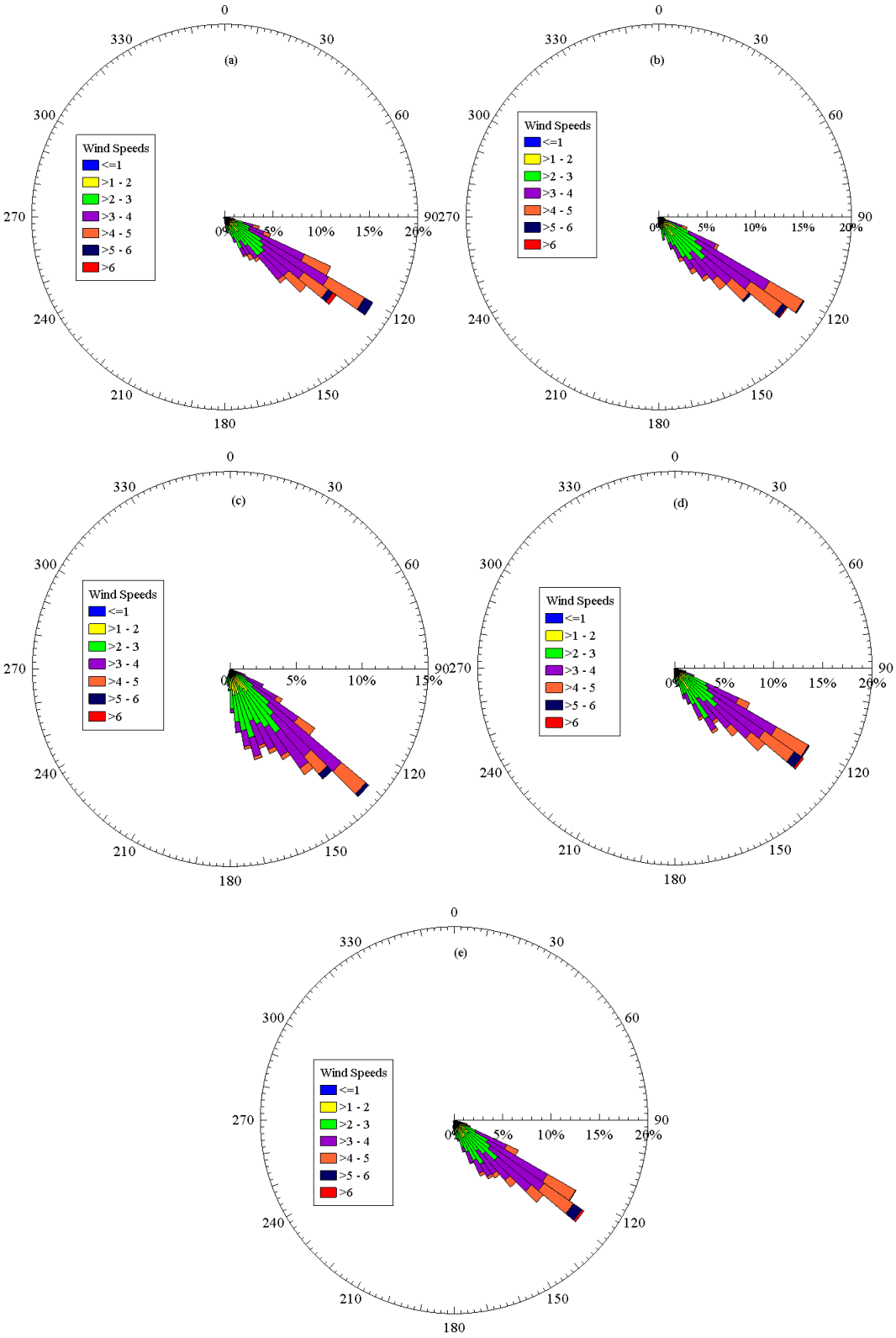

Figure 4.1: Average Wind Speeds and Directional Analysis at a Height of 6 m; (a) Site 1, (b) Site 2, (c) Site 3, (d) Site 4 and (e) Site 5.

Observe in Figure 4.1 that, the wind direction is relatively consistent across the five sites. The average wind direction measured from north (0^o) for the study sites was 133^o, 136^o, 148^o, 137^o, and 138^o for sites 1, 2, 3, 4, and 5, respectively, depicting southerly winds. It is worth noting that for the five sites, an average of 49% of the wind speeds were greater than 3 m/s. Furthermore, wind speeds in sites 1, 2, 4, and 5 exceeded 6 m/s in 0.44%, 0.16%, 0.23%, and 0.25%, respectively. High wind speeds of 6.37 m/s, 6.13 m/s, 6.15 m/s, and 6.15 m/s were recorded at sites 1, 2, 4, and 5. Wind speeds and directions varied due to differences in terrain and module heights at the sites.

Dust deposit resuspension is a function of humidity, as shown in Eqn. 2.12b. Similarly, the magnitude of the adhesive forces involved between the module surface and the dust particles are a factor of relative humidity. As a result, an investigation of humidity and average wind speeds at the study sites is equally important as depicted in Figure 4.2.

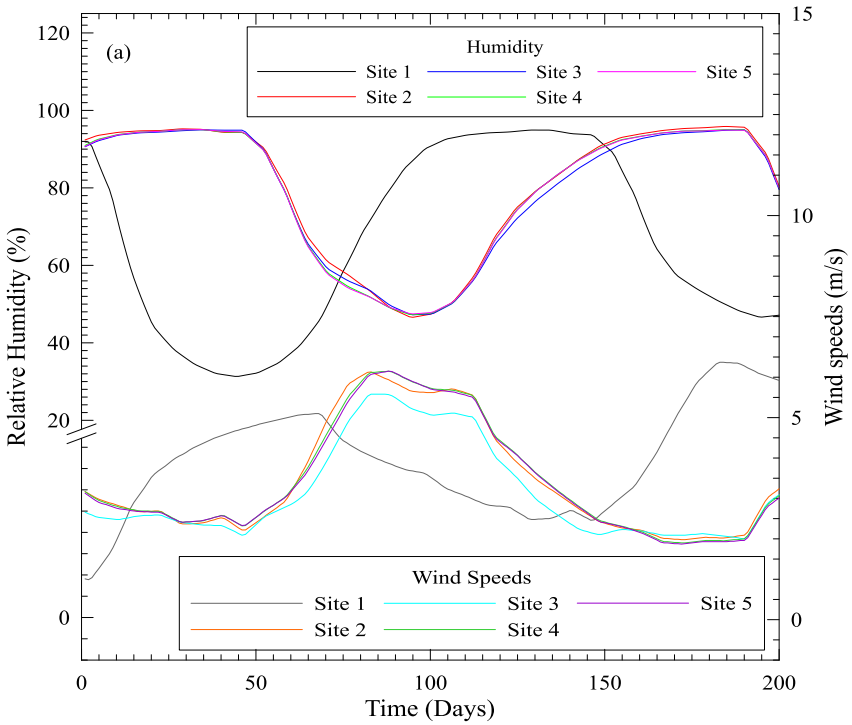

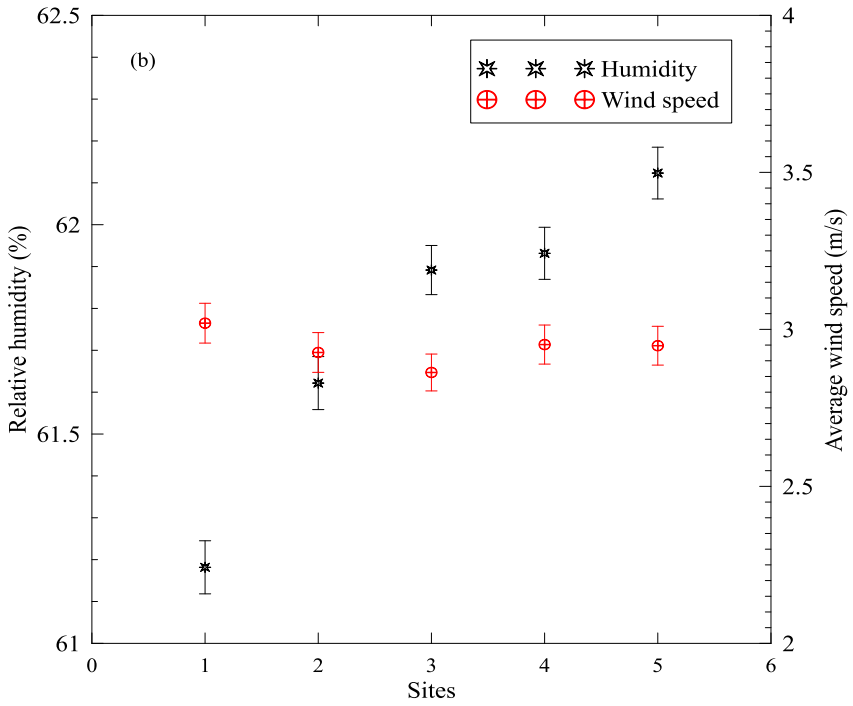

Figure 4.2: Analysis of Relative Humidity and Wind Speeds: (a) Correlation of Relative Humidity and Wind Speeds; (b) Comparison of Average Relative Humidity and Average Wind Speeds across Study Sites.

Figure 4.2(a) depicts the relationship between wind speed and humidity level. Observe that an indirect relationship exists between the wind speed and the relative humidity in which higher wind speeds corresponds to lower relative humidity. Similarly, observe in Figure 4.2(b) that on average, site 5 has higher humidity than site 1 which records higher wind speeds. Hence, this confirms previous research linking dynamic changes in wind speeds to the stochastic regression effect of relative humidity (Mahmud *et al.*, 2020).

4.2.3 Study Modules' Installation Height, Tilt Angle and Orientation Measurements

PV modules are typically installed at a specific orientation and tilt to maximize power output while minimizing environmental effects (i.e., dust effects). Tilt angle and azimuthal orientation (PV installation design) are two of the factors that have a significant impact on dust accumulation rate (Figgis *et al.*, 2019; Menoufi *et al.*,

2017). Table 4.2 presents an analysis of the tilt, orientation, and module height of the study sites.

Table 4.2: Site-Specific Installed Module Height and Tilt Angles

	Installation height (m)	**Tilt Angle (º)**	**Orientation (º) (Surface azimuth)**
Site 1	3.9	13	180
Site 2	3.7	17	0
Site 3	4.1	9	0
Site 4	5.5	8	0
Site 5	5.2	5	180

Table 4.2 shows the variation in module orientation across the study sites. Since the study sites spans latitudes 0° 45' to 1° 31' south and longitudes 36° 45' to 37° 45' east, the north is the preferred optimal orientation across the five sites (azimuth 180°). The variation in module orientation is believed to be attributed to the avoidance of shading from nearby structures and trees around the study site. Furthermore, due to isolated cases of PV module vandalism in the study sites, module installation height variation is acceptable in this study. The maximum and minimum installation heights and tilt angles obtained from site-specific PV system measurements in this study are 5.5 m, 17° and 3.7 m, 5°, respectively. Module siting, as shown in Table 4.2 is critical in the study for analyzing deposition patterns. For an accurate dust deposition analysis at specified module siting, it is critical to match the deposition glass slides with the existing module siting in Table 4.2 at the study sites. The surface of the deposition glass slides is similar to the surface of the PV module, which is made of glazing (Ghosh *et al.*, 2019; Liu *et al*., 2020).

4.3 Dust Deposition Effect on Solar PV Current and Voltage Parameters.

4.3.1 Dust Deposition Rates.

Environmental factors, such as dust, have a significant impact on the degradation of solar cells and the resulting conversion efficiencies. A solar PV module converts incoming radiation that strikes its surface into electrical energy. The output power

produced by the PV module is significantly impacted by a decreased irradiation brought about by dust accumulation on the module surfaces.

The rate of deposition of settled dust particles is highly dependent on particle nature, ground cover, wind speeds, and surface tilt. The adhesive forces also have a significant impact on the fraction of deposited dust particles that remain adhered to surfaces after dust resuspension from the action of natural cleaning agents, such as wind and rain. Furthermore, the study sites' proximity to earthen dusty roads, farm land, and playing fields provides readily available aeolian dust particles for deposition. Figure 4.3 depicts a graphical representation of the ground cover at the research sites.

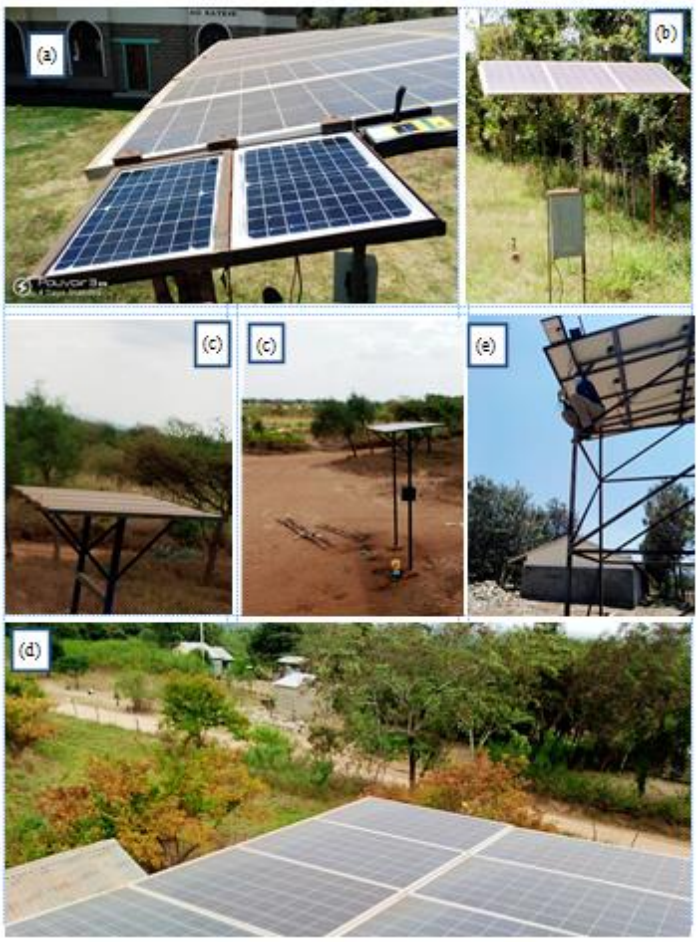

Figure 4.3: Ground Cover Depictions at the Study Sites: (a) Site 1, (b) Site 2, (c) Site 3, (d) Site 4, and (e) Site 5.

Aeolian particles are suspended in the wind as it blows over a surface resulting to irregular bombardment with the ground surface. This results to the generation of additional particles. The morphology of the particles is dictated by the nature of the ground cover. It is anticipated that the ground cover dictates the deposition patterns of the study sites. Figure 4.3 depicts an analysis of dust deposition rates at the selected sites during the study period. It is noteworthy that PV systems have a load-bearing capacity and can be mounted on all types of roofing, but at the same time the static of the roof must not be underestimated. This must be sufficient for permanent installation, taking into account wind loads. A further analysis on the correlation of the dust deposition rates and site-specific wind speeds is presented in Figure 4.4

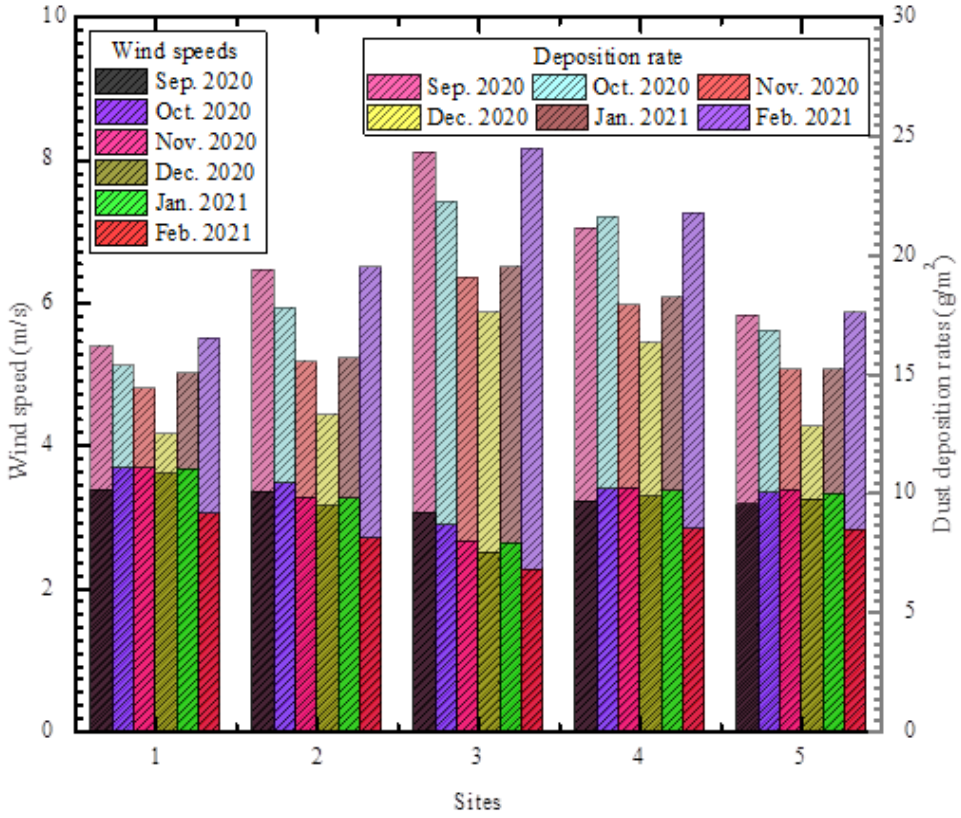

Figure 4.4: Correlation between Dust Deposition Rates and Monthly Average Wind Speeds at the Study Sites.

Figure 4.4 depicts varying dust deposits per month across the sites, with monthly averages of 14.05 g/m^2, 16.692 g/m^2, 19.875 g/m^2, 17.247 g/m^2, and 16.038 g/m^2 for sites 1, 2, 3, 4 and 5, respectively. In general, sites experiencing higher wind speeds

result in lower dust deposits as depicted in Figure 4.4. Due to the short rains in the first few weeks of the months, the deposition rate was lower in November and December. An analysis of the monthly rainfall pattern across the study sites is presented in Figure 4.5.

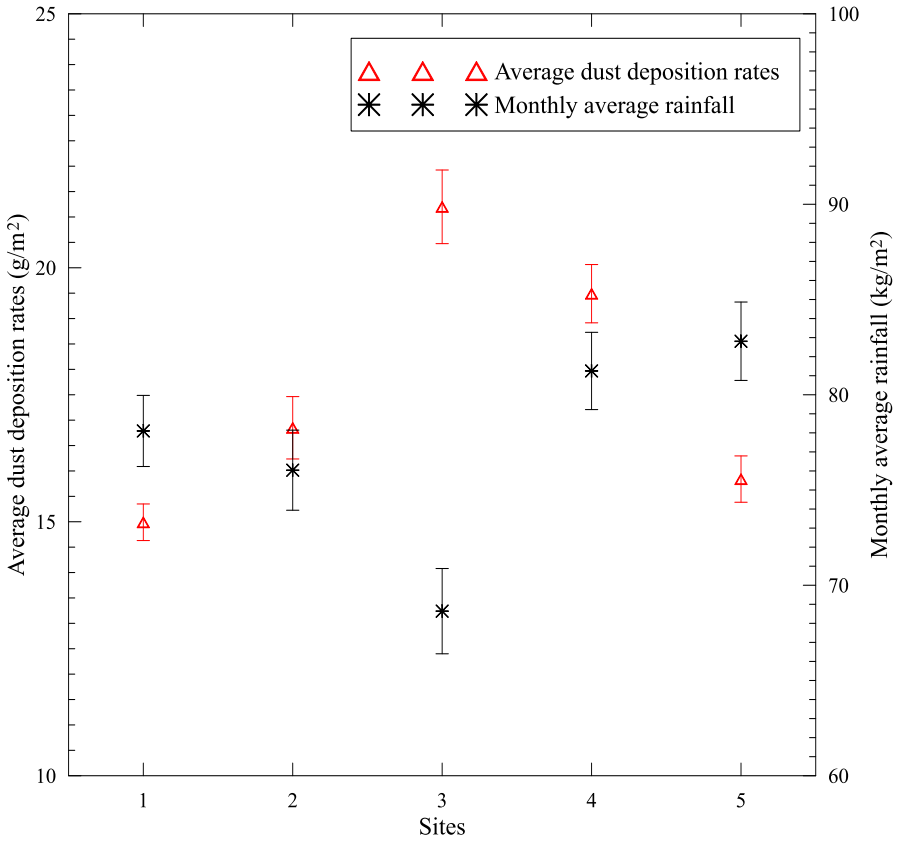

Figure 4-5: Correlation between the Average Dust Deposition Patterns and the Average Monthly Rainfall at the Study Sites.

As shown in Figure 4.5, the average rainfall experienced during the study period had an effect on the masses of accumulated dust particles on the glass slides. Furthermore, sites with higher rainfall experienced low dust deposits on average. It should be noted that the amount of rainfall received during the study period was insufficient to completely clean the glass slides.

In November, data from meteorological stations near the study sites revealed daily averages of 2.02 mm, 2.22 mm, 1.80 mm, 2.00 mm, and 1.96 mm for sites 1, 2, 3, 4, and 5, respectively. Similarly, the daily averages in December were 1.93 mm, 1.77

mm, 1.50 mm, 1.90 mm, and 1.91 mm, for sites 1, 2, 3, 4, and 5, respectively. In contrast, rainfall in the other months (September 2020, October 2020, January 2021, and February 2021) averaged less than 1 mm. Even though the rains couldn't completely clean the glass slides, the rainfall levels recorded in this study were deemed insignificant. Furthermore, no site had a higher variance in the amount of rainfall recorded, implying a negligible contribution to the dust deposition patterns. Similarly, low rainfall increases the adhesive force between dust particles and the surface of the PV module. As a result, dust particle stratification occurs at the lower cells of the PV module, resulting in hard shading (Quan *et al*., 2016). Figure 4.3 and Figure 4.4 show that higher deposition rates are observed in sites with low wind speeds (sites 3, 4 and 5) and no ground cover (site 3) or near an earthen dusty road (site 4). For instance, assuming dust particles trace projectile motion due to their production process; then the particles will exhibit both vertical and horizontal motion. Horizontal motion is dependent on horizontal velocity, which is heavily influenced by wind velocity since it blows incident to the surface. Vertical motion, on the other hand, is entirely dependent on gravitational force. As a result, wind speeds determine how far the particles settle from the source. Low wind speeds and a lack of ground cover increase the likelihood of suspended dust particles settling near the source of emission. Thus, low wind speeds and no ground cover are associated with high deposition rates due to gravity-accelerated free fall deposition patterns.

With reference to Eqn. 2.12b, relative humidity has the effect of increasing the adhesion force that binds dust particles to a surface. This effect also reduces the effectiveness of dust removal over time. The interdependence of wind velocity and the drag and lift forces required to fully dislodge dust particles adhering to the PV modules are shown in Eqns. 2.13a and 2.13b. Increased wind velocity causes an increase in drag and lift forces, resulting in a higher percentage of dislodged and blown particles. These parameters heavily influence PV modules' self-cleaning mechanisms, which rely on natural agents such as wind and rain. The cleaning process's efficiency is also affected by the mode of deposition, which can either be wet or dry. Due to insignificant rainfall during the dust collection period, dry deposition dominated the dust deposit pattern in this study. The increased deposition

rate is caused by a decrease in the magnitude of the force generated by these agents (wind and rainfall) on the PV modules.

The average dust particle sizes determined from dust samples collected from the PV module range from 0 to 150 µm. The wind speeds required to fully dislodge dust particles were calculated using average wind speeds, temperature, relative humidity, and a range of values (between 0 and 500 µm) for the particulate radius. The particulate size specific optimal wind speeds for the study sites were calculated from Eqn. 2.14 where $\alpha = 1.304 \times 10^{-4}\, atom.kg.s^{-2}K^{-1}$, $\beta = 8.289 \times 10^{16}\, m^{-2}$, R is the average radius of the dust particles, $\gamma = 7.12 \times 10^{-2}\, N/m$, Å $= 1.03 \times 10^{-20}\, J$, $\rho = 1.225\, kg/m^3$. Similarly, T is the absolute temperature, C_D and C_L are the force coefficients (which differ depending on the site), and R_H is the relative humidity (Liu *et al.*, 2011; Rastello *et al.*, 2011). Figure 4.6 depicts an analysis of particulate radius in relation to the optimal wind speeds required for particulate resuspension.

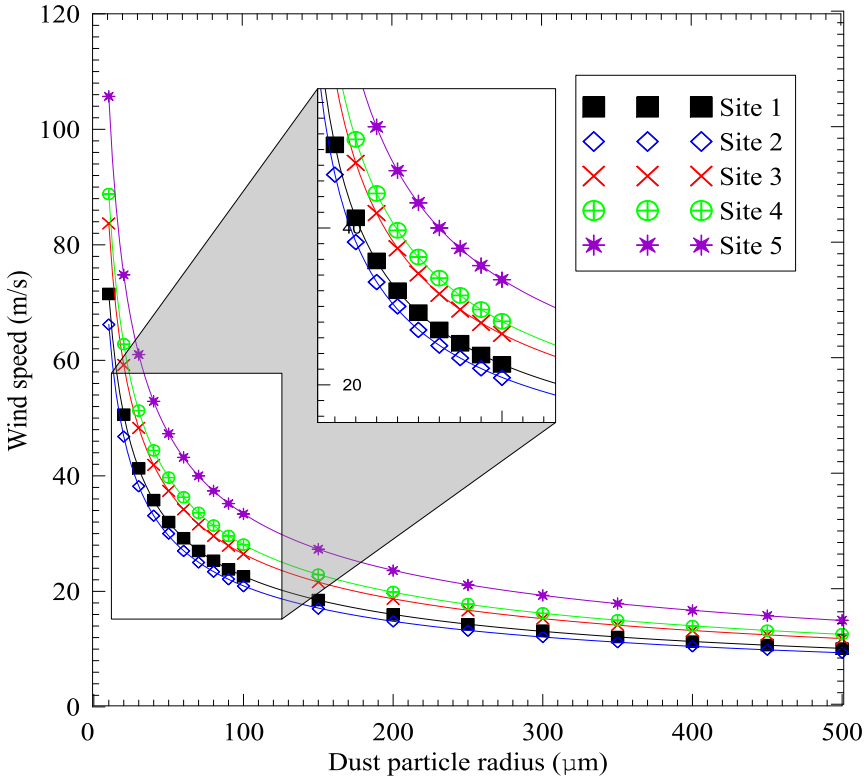

Figure 4.6: Optimal Wind Speeds and Particle Size for Dust Particle Resuspension from PV Surfaces at the Study Sites.

Figure 4.6 depicts the interdependence of optimal wind speeds required to completely dislodge dust particles on the surface of a PV module based on particulate size. Larger particles would require less force to overcome the adhesive forces that keep dust particles stuck to the PV surface. It is worth noting that the analysis presented in Figure 4.6 assumes that larger dust particles are not bombarded on the PV module's surface during the deposition and resuspension processes. The minimum wind speeds required to fully dislodge particles from the PV module surface are 18.5 m/s, 17.01 m/s, 21.6 m/s, 22.9 m/s, and 27.3 m/s for sites 1, 2, 3, 4, and 5, respectively, based on the maximum observed particulate radius (150 μm) as shown in Figure 4.6. However, wind load determination, particularly at the edges of mounting surfaces, must be considered and matched with the manufacturer's load elevation specification.

4.3.2 Dust Effects on Current and Voltage Parameters.

The amount of incident radiation falling on the surfaces of the solar cells for photocurrent generation greatly influences the performance of PV modules. Shade and soiling of PV modules are the primary causes of incident radiation obstruction. The accumulation of dust on the surfaces of PV modules is a major focus of this study. Given the varying deposition rates observed across the study sites, it is critical to examine the performance of dusty PV modules at the Typical Module Operating Temperature (TMOT). The actual operating conditions of PV modules in the field are the TMOT conditions (1061 W/m^2 and 50^{o}C) (Ndeto *et al.,* 2020). Figure 4.7 depicts the I-V characteristic curves for the selected sites over the course of the study.

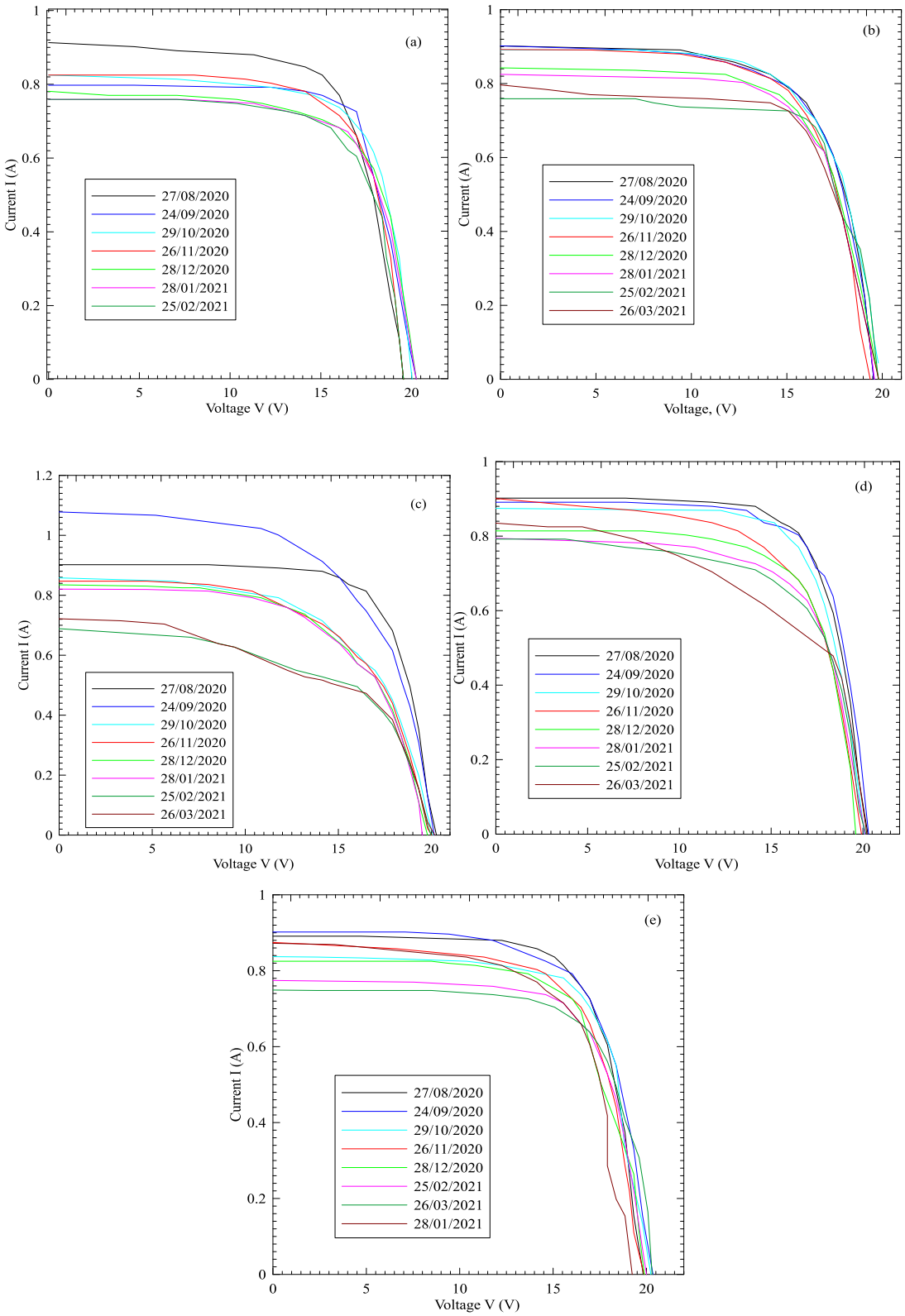

Figure 4.7: I-V Curves for Selected Study Sites over a Duration of 7 Months; (a) Site 1, (b) Site 2, (c) Site 3, (d) Site 4 and (e) Site 5.

According to Figure 4.7, increased exposure of the PV modules to dust and ambient conditions reduces the short circuit current, $\boldsymbol{I}_{SC}$, and maximum power, P_{max}. The consequence of dust exposure on PV modules is reduced photon energy reception. Photocurrent generation from solar cells is dependent on incident radiation falling on a solar cell. The variation in the solar spectrum from sunrise to sunset, spectral content, and average photon energy (APE) all have a significant impact on the photocurrent generated by a solar cell. Similarly, increasing the intensity of light increases the visible component of light. As a result, the photocurrent and APE have an exponential relationship (Ramgolam & Soyjaudah, 2018). After normalizing the data to TMOT, it was expected that there would be little effect because the modules were exposed to the same solar irradiance and thus similar APE.

To determine the extent of soiling on current parameters, this study used the Fountoukis *et al*., (2018) model, which employs the variance in short circuit current, $\boldsymbol{I}_{SC}$, and peak current, $\boldsymbol{I}_{MPP}$. For comparison, the short circuit current density $\boldsymbol{J}_{SC}$ and peak current density $\boldsymbol{J}_{MPP}$ were calculated by taking the quotient of $\boldsymbol{I}_{SC}$ and $\boldsymbol{I}_{MPP}$ and the active area A of the module, respectively. As can be revealed in the I-V curves of Figure 4.7, the $\boldsymbol{I}_{SC}$ and $\boldsymbol{I}_{MPP}$ were obtained from the current intercept and current coordinate of P_{max}, respectively. Similarly, the open circuit voltage V_{OC} and peak voltage V_{MPP} in Figure 4.7 were calculated from the voltage-intercept and voltage coordinate of P_{max}, respectively. Following that, the soiling factors for both the current and voltage parameters were calculated using Eqn. 2.15 and are shown in Figure 4.8(a). Figure 4.8(b) depicts the average percentage change in P_{max}, $\boldsymbol{I}_{MPP}$, and V_{MPP} from no shading to shading obtained from Eqns. 2.16, 2.17, and 2.18.

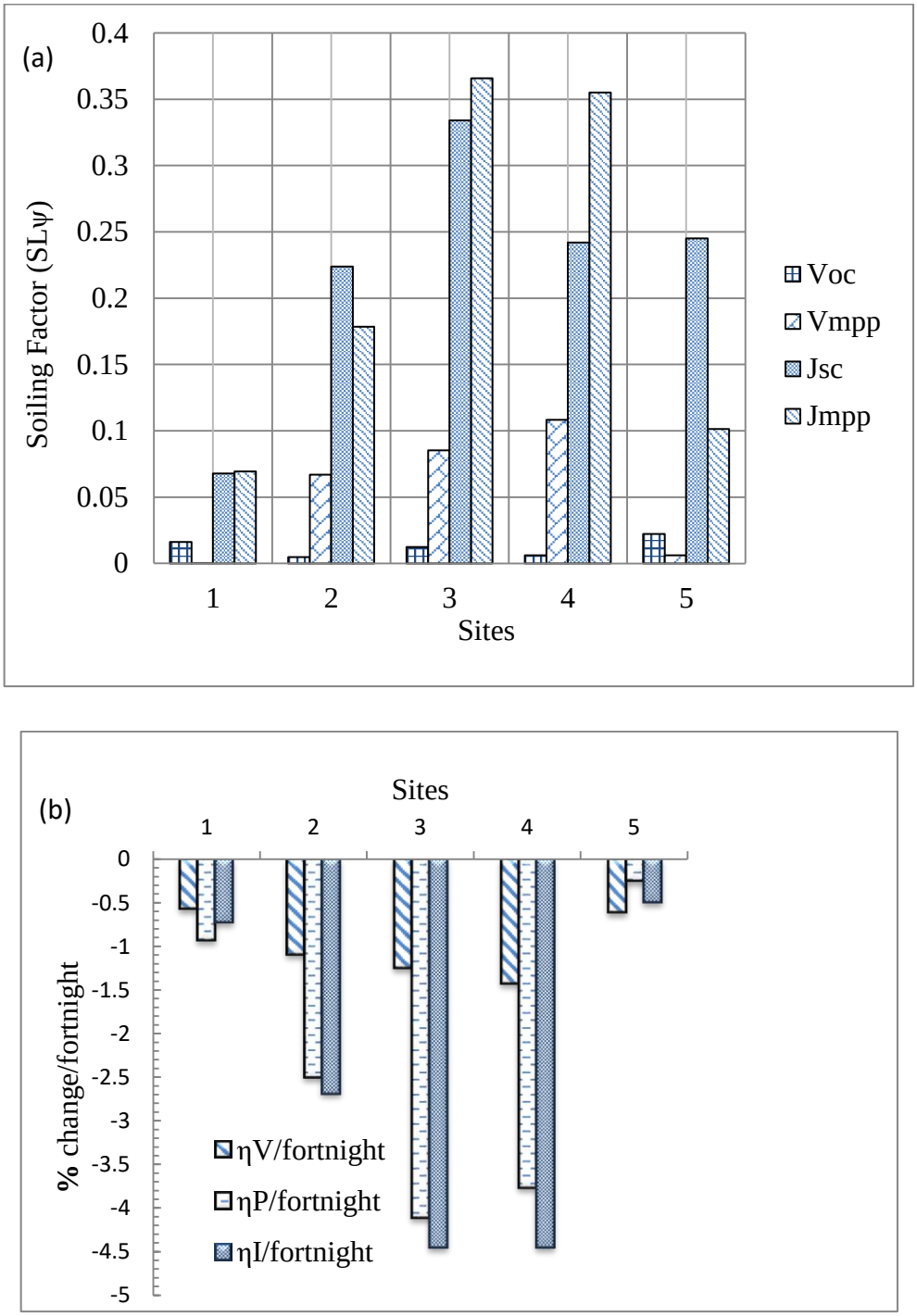

Figure 4.8: Degradation Rates at Study Sites: (a) Average Degradation Rate of Current and Voltage Parameters across Study Sites due to Dust Deposits on PV Modules, (b) Average Percentage Change in Current and Voltage Parameters of PV Modules Exposed to Ambient Dust per Fortnight compared to a Regularly Cleaned PV Module.

According to Figure 4.8(a), significant soiling effect are observed on current parameters in all the sites with major effects being observed in sites 2, 3, 4, and 5. A significant soiling effect on V_{MPP} in sites 2, 3, and 4, and a marginal effect on V_{OC} across all sites are observed. Figure 4.8(b) also shows a decrease in current, voltage, and power across all study sites. On $\boldsymbol{I}_{MPP}$ and P_{max}, the decreasing rate is more rapid, with maximum values of - 4.4%/fortnight and - 4.1%/fortnight in site 3 and – 4.4%/fortnight and - 3.8%/fortnight in site 4, respectively. As previously stated, dust deposition prevents solar radiation from reaching the solar cells, reducing $\boldsymbol{I}_{MPP}$ and, as a result, the decreasing nature of $\boldsymbol{I}_{MPP}$ and P_{max} noted in Figure 4.8(a) (Hegazy, 2001).

Soiling greatly reduces incident radiation falling on solar cells, resulting in a lower photocurrent. Figure 4.4 shows that sites with higher deposition rates, namely sites 3, 4, and 2, have a higher degradation rate of $\boldsymbol{J}_{MPP}$ in the same order (Figure 4.8(a)). Similarly, $\boldsymbol{J}_{SC}$ degradation rates follow the same pattern, with sites 3 and 4 exhibiting the highest degradation rates. Figure 4.4 and 4.8(a) show that there is a positive correlation between the dust deposition rates and the degradation of the current parameters.

The open circuit voltage V_{OC}, on the other hand, is generated by a difference in the quasi-fermi levels between two contacts of an irradiated solar cell at zero current flow. Similarly, at V_{OC}, the only available process is electron-hole recombination, which is completely dependent on concentrations while the generation rate is dependent on photon flux (Azzouzi *et al.*, 2019). The internal energies of the silicon particles increase as the temperature rises. This increases collisions, leading to increased resistance, which leads to a reduced charge recombination process and a decrease in V_{OC}. After normalizing the temperature to TMOT conditions, the effect of soiling on V_{OC} was expected to be minimal, as shown in Figure 4.8(a). The decrease in V_{MPP} is explained by variations in energy losses in the charge recombination process, which is dependent on optical absorption and surface recombination. Due to reduced incident radiation participating in photo-current generation, dust deposits have a greater impact on current parameters than voltage parameters. This is due to the generation rate's dependence on photon flux *(*Maghami

et al., 2016). As a result, modules must be cleaned on a regular basis (depending on location and experience) and as needed (spot contamination) (Ngure *et al.*, 2022). Although the cleaning of spot contamination by dust is now common practice, the economic benefit of regular cleaning for large area contamination by dust is widely debated.

The soiling effect on PV modules can be divided into three categories: shielding effect, temperature effect, and corrosion effect (Azzouzi *et al.*, 2019). After observing some leading effects on the shielding component of soiling, the temperature effect was investigated further. The effect of soiling on the temperature coefficient $T_{C,V_{MPP}}$ for V_{MPP} is shown in Figure 4.9.

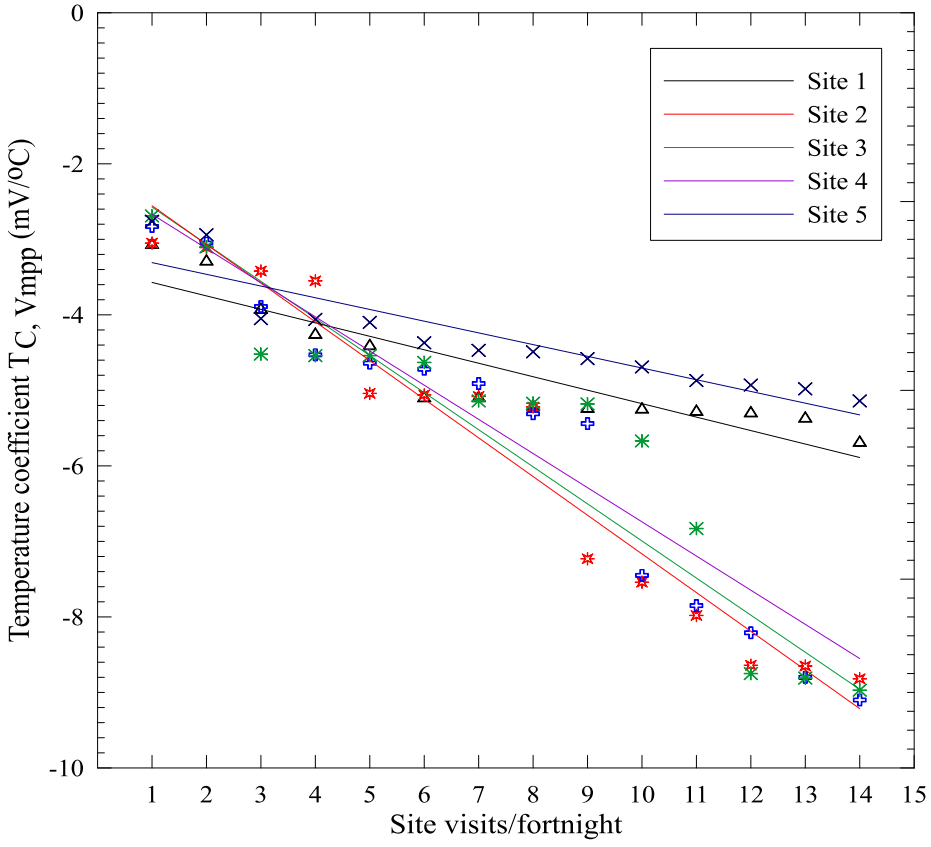

Figure 4.9: Graphical Representation of the Temperature Coefficient $T_{C,V_{MPP}}$ per Fortnight across the Study Sites.

The $T_{C,V_{MPP}}$ values were calculated using Eqn. 2.19. Figure 4.9 shows that as the exposure duration increases, so does the temperature coefficient $T_{C,V_{MPP}}$. This

means that the V_{MPP} of a module exposed to dust would decrease significantly per degree Celsius (ºC) increase in cell temperature compared to a regularly cleaned module over the same duration. It is evident from Figure 4.9 that the temperature coefficient increased significantly in sites 2, 3, and 4 over the study period. Dust deposits on the PV surface form an insulation layer on the module's surface, resulting in a lower rate of temperature loss. This effect increases the randomness and collision of electrons participating in electron-hole recombination as a result of increased kinetic energy. Increased collisions result in lower output voltage, resulting in a significant decrease in the module's power output. This is due to a decrease in the number of electron-hole recombination as a result of collisions, which accounts for the variation in V_{MPP} and $T_{C,V_{MPP}}$ shown in Figure 4.8 and 4.9 (Jaszczur *et al.*, 2018; Kata *et al.*, 2018). The P_{max} degradation rate as a result of shielding and temperature effect of dust deposits obtained from the product of the slopes in Figure 4.9 and the degradation rate of $\boldsymbol{J}_{MPP}$ per fortnight (Figure 4.8) is 8.89 mW/m^2/ºC/fortnight, 40.03 mW/m^2/ºC/fortnight, 136.29 mW/m^2/ºC/fortnight, 94.95 mW/m^2/ºC/fortnight and 8.79 mW/m^2/ºC/fortnight for sites 1, 2, 3, 4, and 5, respectively. The soiling effect alters the performance of the solar modules, causing them to consume energy rather than generate it, resulting in hotspots.

4.4 Dust Deposition Rates as a Factor of Module Height, Tilt and Orientation in Southerly Winds.

Ballistic trajectories of saltating aeolian particles are primarily determined by gravitational and aerodynamic drag. Due to particle spinning and the gradient in wind speeds, airborne particles experience aerodynamic lift forces. Similarly, gravitational forces play a significant role in determining the particulate size distribution of wind-blown sediments, which heavily influences deposition patterns (Premono *et al.*, 2017). Wind speeds increase with vertical wind profile, resulting in an increase in aerodynamic lift force and a decrease in resuspended aerosols' particulate mean diameters. Similarly, variations in the aerodynamic lift force on suspended and settled aeolian particles caused by variations in gravitational forces, wind profile, and surface tilt have a significant impact on dust deposition patterns. Wind, a natural phenomenon, influences deposition patterns significantly, hence its

importance in this study (Pennetta *et al.*, 2016). As a result, additional research on the effects of module height, tilt, and orientation on deposition patterns is required for a conclusive deduction on dust deposition patterns. Figure 4.10 depicts the wind profile of the chosen location.

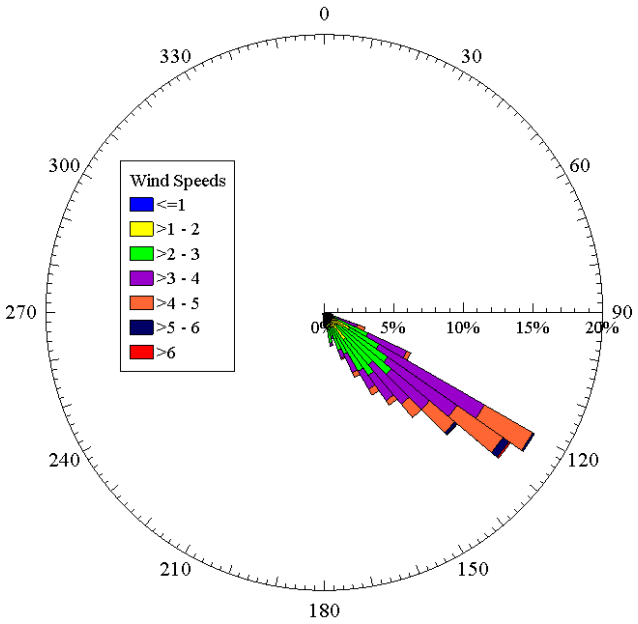

Figure 4.10: Wind Profile for the Selected Research Site.

Figure 4.10 shows that the wind was blowing from the south-east, with a more specific average direction of 120^{o} to 130^{o} from the north (0^{o}). Furthermore, 48.69% of the wind blew at speeds greater than 3 m/s, with only 7% exceeding 6 m/s, with a peak of 6.13 m/s. Wind speeds, for instance, increase logarithmically with height and are affected by surface roughness, which ranges from 2 for forests and town centers to 0.025 for smooth and flat surfaces (Stovern *et al.*, 2016). Based on this analysis, the south-facing glass slides were determined to be on the windward side, while the north-facing glass slides were ascertained to be on the leeward side as illustrated in Figure 4.11. Figure 4.11 depicts an analysis of the deposition patterns at various heights, orientations, and tilts.

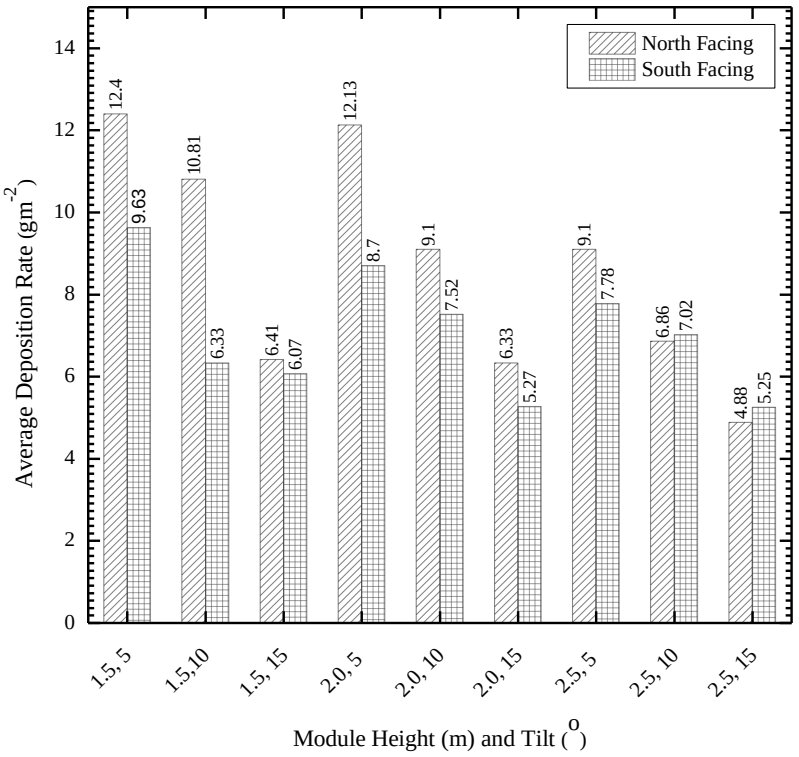

Figure 4.11: Average Dust Deposits per Week at Varying Height (m), Tilt (º) and Orientation

Figure 4.11 show that on average, north facing glass slides experienced higher deposition rates compared to the south facing ones. Similarly, near horizontal tilt angle (5º) experienced higher deposition rates as compared to a tilt angle of 10º and 15º with the exception of elevation height at 2.5 m. The slight variance in the installation heights at the study site presented little changes in the wind speeds near ground level even though significant aerodynamic lift forces were experienced (Kok *et al*., 2012). As previously stated, aerodynamic lift forces and dust particle sizes (height dependent) dictate aeolian particle deposition patterns, resulting in the pattern shown in Figure 4.11 as the height increases. Small-scale stratification was found to be more prominent on the leeward side and at the base of the glass slides in both windward and leeward deposits. Pennetta *et al*. (2016) discovered a link between wind speed and direction and dust deposition patterns, which supports the pattern depicted in Figure 4.11. It is evident from Figure 4.11 that higher deposition rates are

observed on glass slides facing the leeward side rather than the windward side. Wind-facing surfaces experience streamlined flow, which causes dust particles to be resuspended due to increased fluid velocity at reduced fluid pressure. The leeward side, on the other hand, experiences non- streamlined flow, which result to eddies that slow the fluid velocity, resulting in an increased deposition rate. This effect is less pronounced at higher height and tilt angle due to the reduced particle sizes. The observed deposition patterns corresponded to studies on wind-blown dust deposits on mine tailings impoundments in Central Arizona, which revealed that southerly winds had significant deposition rates on north-facing surfaces (Stovern *et al*., 2016).

Finally, it is clear that the orientation effect on deposition patterns decreases as module height increases, with a preferred installation height of 2.5 m and a tilt angle of 15^{o}. Although a module installed at a height of 2.5 m and a tilt angle of 10^{o} show a negligible difference in dust deposits on north and south facing surfaces, a height of 2.5 m and a tilt angle of 15^{o} show an all-time low deposition pattern regardless of orientation. In comparison to previous studies for near-equator locations, each 1^{o} increase in tilt angle resulted in a 12.62% decrease in dust deposition rates (Hachicha *et al.,* 2019). Similarly, the annual solar energy obtainable at a dry season optimum angle of 13.90^{o} was 7.2% higher than at a horizontal tilt (0^{o}) (Kurnianto *et al*., 2017), resulting in higher irradiance and thus higher PV output power.

4.5 Dust Elemental Concentration, Characteristics and Effects on the Conversion Efficiency of m-Si Solar PV Module

4.5.1 Elements Concentration by Mass per Kilogram of Sample

Dust, a natural phenomenon that represents suspended particles in the air, contains varying percentages of elements by mass. The study sites' uniqueness provides an excellent opportunity to quantify the extent of various dust characteristics on PV modules. Similarly, the elemental concentrations of background soils present in the study sites are critical in predicting potential sources of dust accumulated on PV modules. Table 4.3 presents a summary analysis of the samples collected from the study sites. Table 4.3 shows the varying distribution of elements in soil and dust samples across the study sites. Table 4.3(a) and Table 4.3(b) show abundance of

Aluminium (Al), Potassium (K), Calcium (Ca), and Iron (Fe) across the study sites as compared to other elements despite their different concentrations. A similar trend is replicated in the concentrations of the other elements across the study sites. This variation is due to the different soil types encountered in the study sites, as well as the various sources of dust, which will be confirmed at a later stage. The elemental concentrations of different soil types discussed in section 3.5.5 matched the background concentrations of soil samples presented in Table 4.3(a), as documented by Towett *et al.,* (2015). Therefore, each of the five study sites had a distinct soil type and composition.

Table 4.3: Elemental Concentration of Samples Presented to ICRAF for Elemental Analysis (a) Background Soil Sample Concentration and (b) Dust Sample Concentration across the Study Sites

	(a) Background Soil sample concentration in g/kg of soil													
Site	**Na**	**Mg**	**Al**	**P**	**K**	**Ca**	**Ti**	**Cr**	**Mn**	**Fe**	**Ni**	**Cu**	**Zn**	**Pb**
1	1399	8260	37940	228	12619	19068	5959	55	599	29268	23	18	41	28
2	567	5075	19136	43	11508	3467	1343	39	192	5395	5.3	3.9	8.8	10
3	786	4602	13305	48	8484	6312	871	13	180	8365	8.4	7.5	10	14
4	976	3255	40940	47	9145	1918	3640	45	341	23754	21	23	36	23
5	789	5369	42542	210	8717	1440	8564	53	578	34957	21	21	41	36
	(b) Dust sample concentration in g/kg													
Site	**Na**	**Mg**	**Al**	**P**	**K**	**Ca**	**Ti**	**Cr**	**Mn**	**Fe**	**Ni**	**Cu**	**Zn**	**Pb**
1	1689.5	3911	46374.5	1107	7058	4580.5	850.5	33	932.5	33415	28.5	46	309	0
2	647	5325.5	62488.5	848	7431.5	7015.5	685.5	57.5	2061.5	62150.5	48	37.5	339	0
3	876.5	4015	55289	1816.5	5668.5	10848	1151	53	2260	61506.5	42	35	299	0
4	1065	2922	45582.5	620	7240.5	5137.5	1378	153	11040	104907.5	113.5	253	20436	262.5
5	808	3538.5	57433	808	6357	8628.5	1276.5	66	3330.5	62832.5	46.5	10	289	0

Variation in the abundance of elements present in the collected dust samples indicated site-specific emissions. A measure of element dispersion in dust samples collected from study sites provided information on potential enriched elements. A normal concentration of elements was identified across the study sites by a low

deviation from the mean (less than 500 mg/kg). Table 4.4 presents a comprehensive analysis of the element descriptive statistics with the goal of determining the variance in the individual elemental concentration across the five sites.

Table 4.4: Total Element Descriptive Statistics

Statistic	Min (mg/kg)	Max (mg/kg)	Median (mg/kg)	Mean (mg/kg)	S.dev. (mg/kg)
Na	647	1690	876	1017	361.9
Mg	2922	5326	3911	3942	790.4
Al	45582	62488	55289	53434	6525.3
P	620	1816	848	1040	418.2
S	353	535	456	442	60.3
K	5668	7432	7058	6751	651.8
Ca	4580	10848	7016	7242	2301.7
Ti	686	1378	1151	1068	260.8
Cr	33	153	57.5	72	41.7
Mn	932	11040	2260	3925	3638
Fe	33415	104908	62150	64962	22870.2
Co	7	8	7	7	0.4
Ni	28	114	46	56	28.7
Cu	10	253	37.5	76	89.2
Zn	289	20436	309	4334	8050.8

Table 4.4 shows a greater variation in iron (Fe), zinc (Zn), aluminum (Al), manganese (Mn), calcium (Ca), magnesium (Mg), and potassium (K) across the study sites. The variance parameter was used to calculate the degree of deviation from the mean of statistical data. The square of standard deviation is indeed variance (S.dev.). Even though the individual measures of central tendency appeared similar, higher standard deviation indicated enrichment differences (Sprovieri & Pirrone, 2008). This difference is caused by a greater disparity in element concentration between the study sites, resulting in a greater deviation from the mean. Figure 4.12

depicts a further probe into the contribution of elements exhibiting greater variance to the average dust deposition rates.

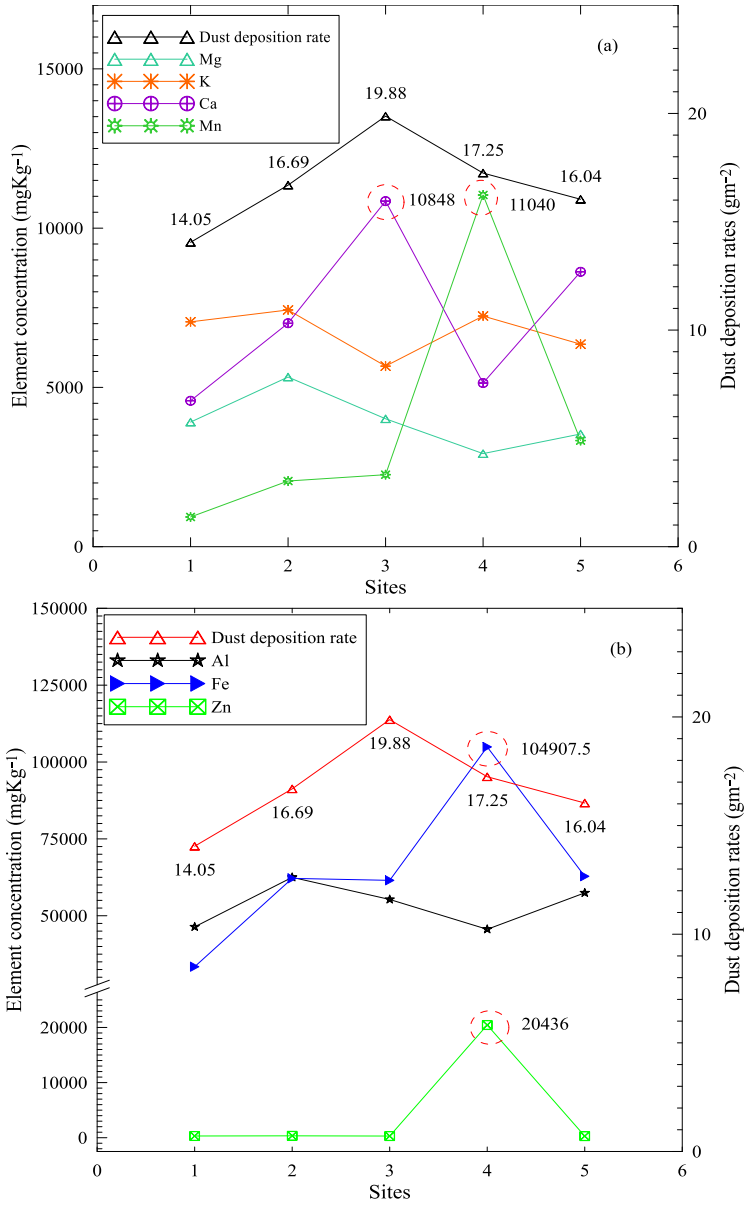

Figure 4.12: High Variant Element Correlation with Average Dust Deposition Rates across Study Sites (a) Magnesium (Mg), Potassium (K), Calcium (Ca), and Manganese (Mn) (b) Aluminium (Al), Iron (Fe), and Zinc (Zn).

Figure 4.12 shows that sites with high concentrations of Ca, Mn, Fe, and Zn have higher deposition rates on average, as shown in sites 3 and 4. Table 4.3 shows that Mn, Fe, Zn, and Pb are abundant at Site 4. In comparison to Table 2.1 the source of

the dust deposits on PV modules at site 4 is considered to be road transport. Similarly, higher calcium concentrations in dust samples at site 3 correspond to a variety of sources, including roadside dust, coal combustion, wood smoke, and re-suspended soil. The presence of multiple potential calcium sources necessitates the determination of an Enrichment Factor (*EF*) in order to accurately classify dust samples to potential emission sources. Similarly, *EF* will identify the primary source of dust deposits at sites 1, 2, and 5.

4.5.2 Dust Enrichment Factors (EF) and Characterization

The variability in the sources of dust deposits accumulated on the surfaces of the study modules hinders accurate identification of the major emission source. The enrichment factor, a parameter used to characterize the degree of elemental enrichment, aided in identifying the major sources of dust emissions across the study sites. Table 4.5 presents an analysis of the enrichment of elements across the study sites calculated from Eqn.4 using Aluminium (Al) as the reference element. A further characterization of the level of enrichment derived from Table 4.5 is also presented.

Table 4.5: Analysis of Enrichment Factors (*EF*)

	Enrichment Factor (EF)													
Site	**Na**	**Mg**	**Al**	**P**	**K**	**Ca**	**Ti**	**Cr**	**Mn**	**Fe**	**Ni**	**Cu**	**Zn**	**Pb**
1	0.22	0.39	1	3.97	0.46	0.20	0.12	0.50	1.27	0.93	1.01	2.15	6.17	0
2	0.09	0.32	1	6.04	0.20	0.62	0.16	0.45	3.29	3.53	2.77	2.94	11.80	0
3	0.09	0.21	1	9.11	0.16	0.41	0.32	0.98	3.02	1.77	1.20	1.12	7.20	0
4	0.08	0.81	1	11.85	0.71	2.41	0.34	3.06	29.08	3.97	4.85	9.88	509.85	10.25
5	0.10	0.49	1	2.85	0.54	4.44	0.11	0.92	4.27	1.33	1.64	0.35	5.22	0

As shown in Table 4.5, majority of elements present in dust samples collected from PV surfaces had minimal to moderate *EF* (<5). Significant *EF* levels in Zinc (Zn) were found at sites 2, 3, 1, and 5, with peaks of 11.8, 7.2, 6.2, and 5.2, respectively. Similarly, Phosphorous (P) enrichment levels were significant in dust samples collected from sites 2, 3, and 4, with highs of 6.0, 9.1, and 11.9, respectively. It is worth noting that some isolated cases of significant, very high, and extremely high

enrichment factors were found in samples collected from site 4. Copper (Cu) and Lead (Pb), for example, had significant EFs of 9.9 and 10.3, respectively, while Manganese (Mn) had a very high EF of 29.1 and Zinc (Zn) had an extremely high EF of 509.9.

The dust samples collected were classified as biogenic, geogenic, or anthropogenic based on the *EF* (Table 4.5) and the elemental concentration of emission sources (Table 2.1). Dust collected from site 1 was classified as biogenic due to moderate and significant enrichment levels in P and Zn, respectively, and low to insignificant enrichment levels in the majority of the elements (Towett *et al*., 2015). Similarly, dust samples collected from site 2 contained biogenic and minor traces of anthropogenic and geogenic particles due to significant levels of Zn and P, as well as moderate enrichment of Mn, Fe, Ni, and Cu. Dust samples collected from site 3 showed significant enrichment levels of P and Zn, with moderate enrichment levels of Mn, indicating that the dust samples were highly biogenic with traces of geogenic and anthropogenic particles. The presence of high concentrations of enriched elements (P, Ca, Cr, Mn, Fe, Ni, Cu, Zn, and Pb) in dust samples from site 4 indicated that the samples were primarily anthropogenic, with traces of geogenic and biogenic origin (Vanegas *et al*., 2021). Finally, the dust samples collected at site 5 contained geogenic particles with significant traces of biogenic particles due to moderate enrichment levels of P, Ca, Mn, and Zn (Karuma *et al.*, 2015). Observe from Table 4.5 that, site 4 has significantly higher enrichment factors than other study sites, indicating a higher level of anthropogenic activity around the study site. Site 4 is, for instance, near a busy highway leading to a nearby town and this forms the primary source of anthropogenic particles.

4.5.3 Dust Effects on m-Si Solar Module's Maximum Power (P_{max}) and Conversion Efficiency (η).

PV module performance is determined by the maximum power delivered and the conversion efficiency of the module (Zeedan *et al.*, 2021). Solar irradiance, module orientation with respect to the solar path, and technology used are the key performance determinants. The variation in the fraction of solar irradiance falling on

the active area of the PV module greatly influences the module's output power (Mustafa *et al.*, 2020). Dust, a component of soiling, obstructs incident radiation that falls on solar cells, reducing the number of photons involved in electron-hole separation. This effect reduces photocurrent and, as a result, the maximum power delivered to an external circuit. Figure 4.13 depicts the extent of dust accumulation on the Maximum power (P_{max}) and Power conversion efficiency (η).

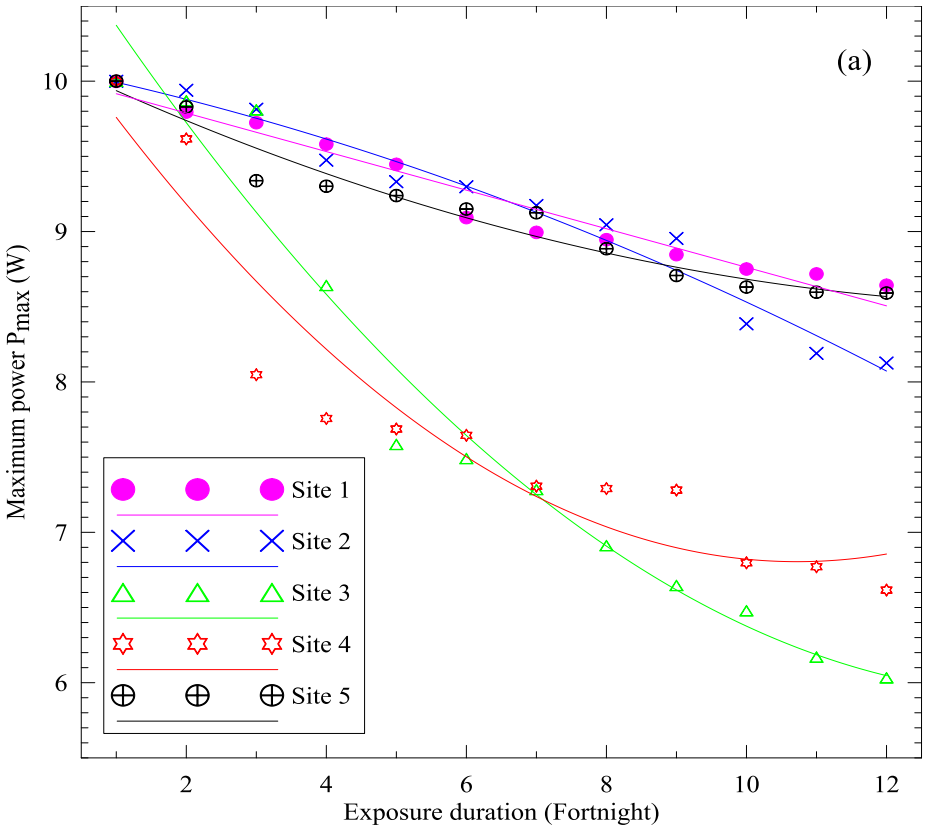

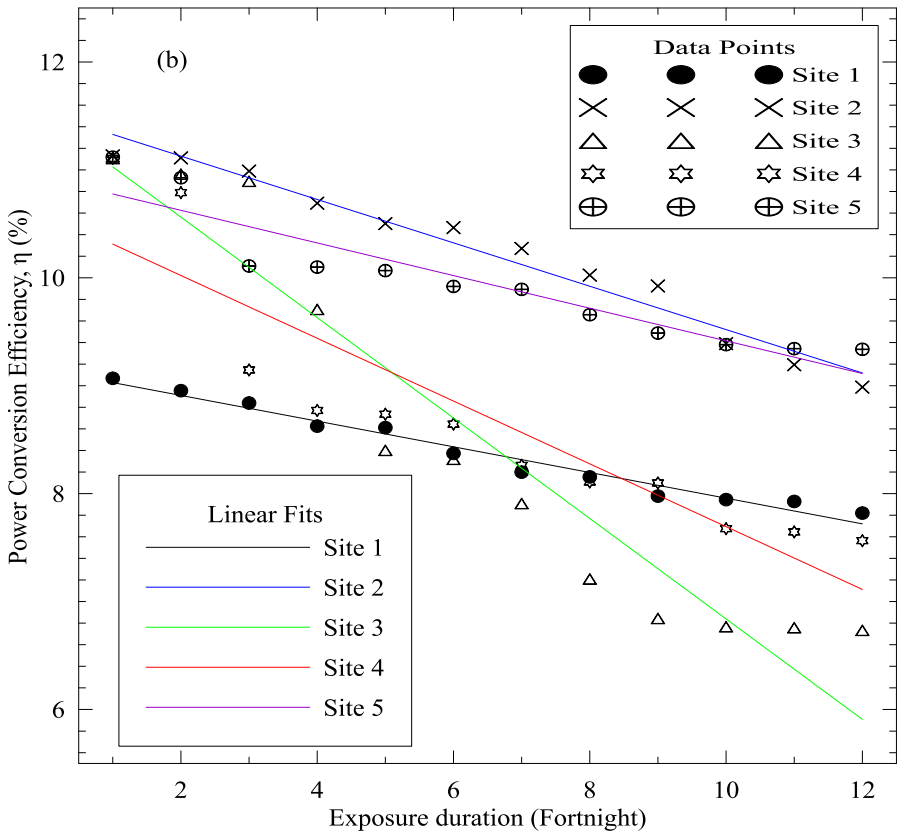

Figure 4.13: Analysis of PV Module Performance Indicators (a) Variation in P_{max} and (b) Change in η as a Result of Dust Exposure.

Figure 4.13(a) depicts an analysis of the P_{max} at Typical Module Operating Temperature (TMOT) conditions of 50^{o}C and soiling. Figure 4.13(a) shows a general decrease in P_{max} across the study sites, with major effects observed in sites 3 and 4. Sites 1, 2, and 5 have minor effects from dust deposition. Similarly, as shown in Figure 4.13(b), the conversion efficiency η of the module is decreasing. The slope of the graphs in Figure 4.13(b) shows a decrease in η of 0.12, 0.20, 0.47, 0.29, and 0.15 on average per fortnight in sites 1, 2, 3, 4, and 5, respectively. Figure 4.4 and Figure 4.13 show a positive correlation between the degradation rates of P_{max} and η with the rates of dust deposition. For instance, over the course of the study, high deposition rates were observed at sites 3, 4, and 2, with the same trend being replicated in P_{max} and η degradation rates. The P_{max} and η degradation rates are clearly related to the rates of dust deposition on the surfaces of PV modules. As earlier alluded to in section 4.3.2, an increase in the temperature coefficient of voltage at maximum

power point (V_{MPP}) is caused by an increased layer of dust on PV surfaces. An increase in the temperature coefficient results to increased randomness and collisions of charge carriers hence reduced electron-hole recombination leading to a lowered V_{MPP} and eventually P_{max}. Similarly, the decrease in P_{max} and η is attributed to a lower amount of incident radiation falling on the solar cells as a consequence of the dust layer tinting the active area of the PV module. As previously stated, the amount of incident radiation participating in the electron-hole separation in the p-n boundary of silicon solar cells determines the photocurrent generated (Rühle, 2016). Similarly, the three sites (3, 4 and 2) with high conversion efficiency degradation rates exhibited varying proportions of anthropogenic dust particles (section 4.5.2). As a result, the abundance of anthropogenic dust particles and high dust deposition rates explain the degradation trends observed in Figure 4.13. According to the analysis, the majority of anthropogenic particles present in dust settled on PV modules are caused by road dust/vehicular emissions. On one hand, large surface deposition by dust reduces PV module output power significantly. Selective dust deposition, on the other hand, causes hotspots and thus the destruction of solar modules. To mitigate the negative effects of dust on PV output parameters, it is highly recommended that PV systems be installed far from roads with minimal cable power losses.

4.6 Automated Self-Cleaning System Analysis

4.6.1 Self-Cleaning Model's Performance

Based on the deleterious effects of dust on PV output parameters as earlier investigated and the short fall of the site-specific wind speeds on resuspension of dust adhered to the PV surfaces, a design of a self-cleaning system based on a denser medium to air was inevitable. Air and water jets of sufficient velocities generate drag and lift forces superseding the PV surface dust adhesive forces leading to the resuspension of the dust particles (Moutinho *et al.*, 2017; Tan *et al.*, 2014). Figure 4.14 represents an analysis of the fluid velocities generated by the air and water jets.

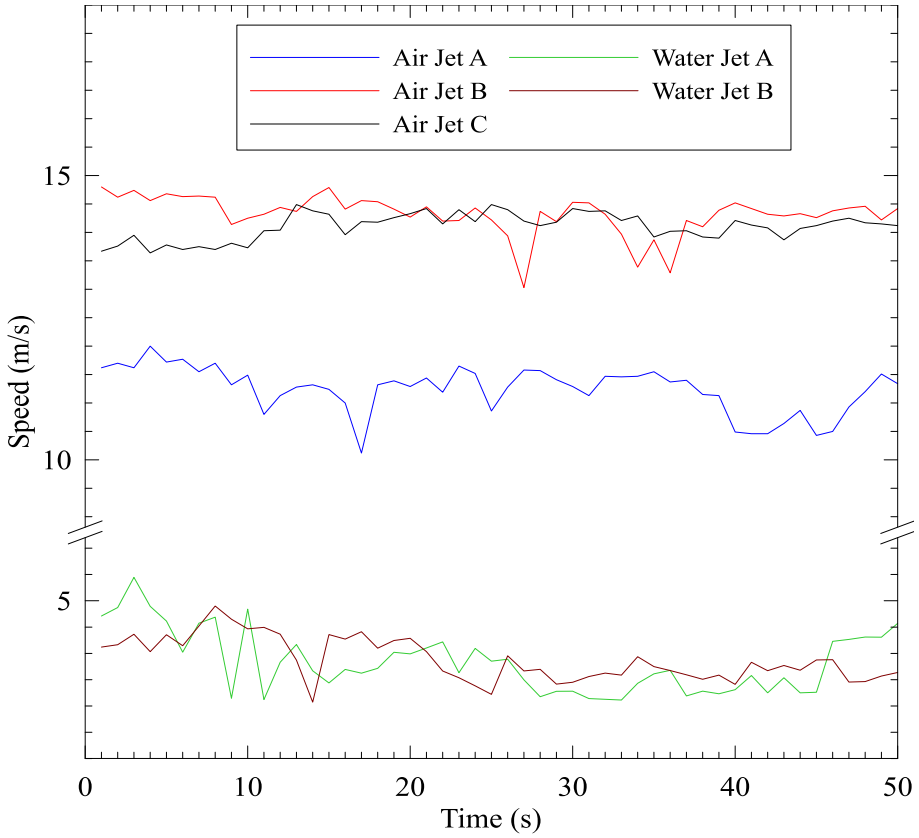

Figure 4.14: Air and Water Jets Velocities

Observe in Figure 4.14 that on average, the speeds of the air jets generated by the three identical 9 W 12 V DC fans are 11.24 m/s, 14.32 m/s and 14.10 m/s. Similarly, the average speeds of the two major water jets are 3.83 m/s and 3.88 m/s. It is evident from Figure 4.14 that the generated jet speeds are higher than the recorded average wind speeds at the study sites (Figure 4.1). The drag and lift forces generated from the jets were calculated from Eqns. 2.13a and 2.13b with the coefficients of drag C_D and lift C_L forces taken as 0.47 and 0.37 for spherical water droplets and 0.42 and 1.755 for free falling non rotating air particles, respectively (Ekanayake *et al.*, 2021; Liu *et al.*, 2011). The densities of water and air were taken as 1000 kg/m^3 and 1.225 kg/m^3, respectively. Figure 4.15 presents the generated lift and drag forces by the air and the water jets.

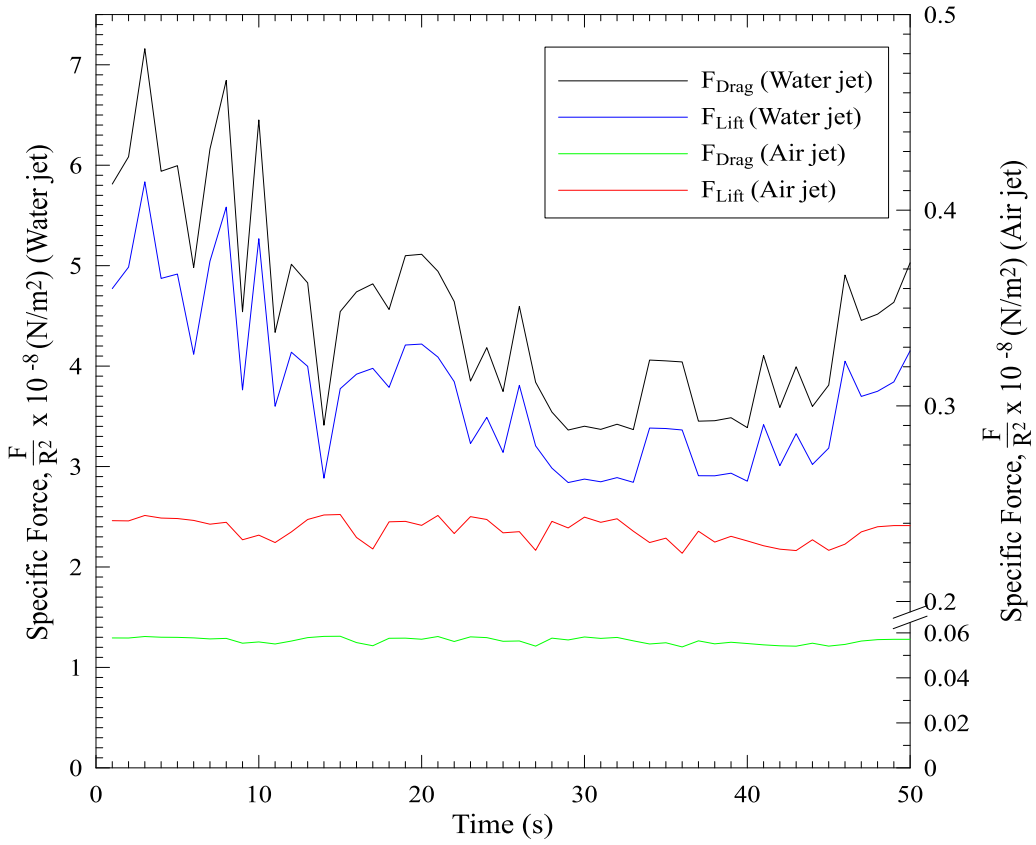

Figure 4.15: Air and Water Jets Generated Drag and Lift Forces (Eqns. 2.13a and 2.13b)

Figure 4.15 shows that despite the air jets having higher velocities (Figure 4.14), they generate lower drag and lift forces per unit area as compared to the water jets. This is attributable to the variance in their densities. Drag forces dominate in denser fluids while lift forces dominate in less dense fluids. The resultant specific drag and lift forces per unit area are 4.51 N/m^2 and 3.74 N/m^2, respectively. A comparison of the average lift and drag forces generated by the air and water jets (Figure 4.15) to the required drag and lift forces for complete resuspension of dust particles adhered to PV surfaces (Figure 4-6) is presented in Figure 4.16.

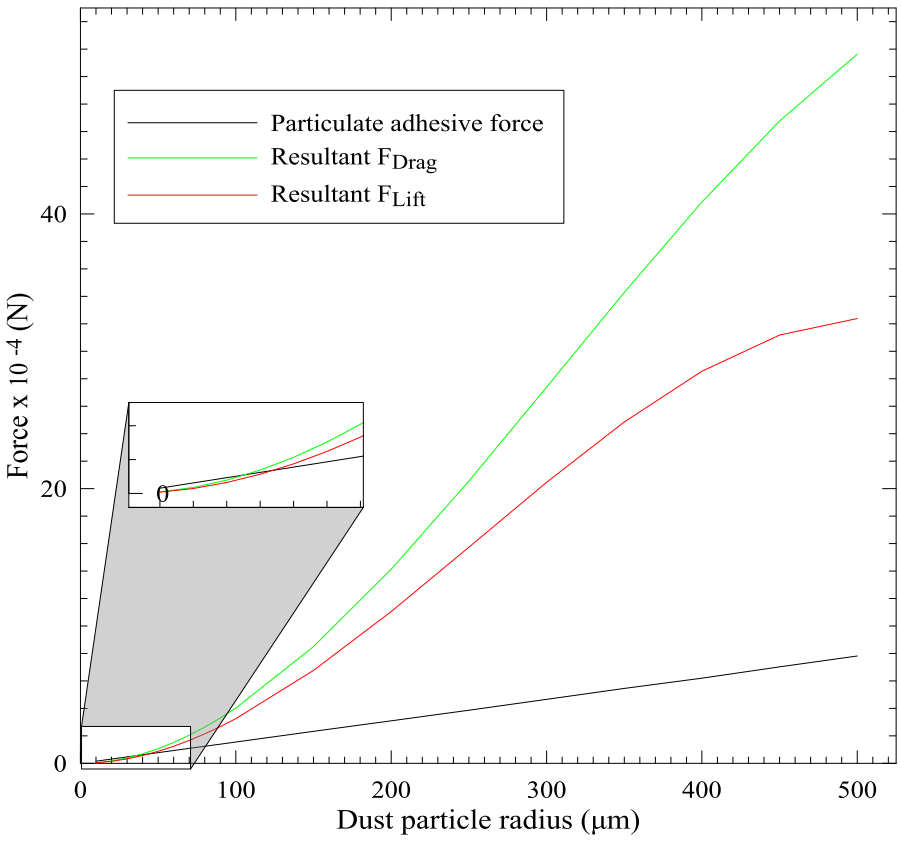

Figure 4.16: Required Forces for Dust Particle Resuspension against the Generated Resultant Force

Observe from Figure 4.16.that, the generated drag and lift forces exceed the particulate specific adhesive force. The required resultant drag and lift forces depend greatly on the particulate radius of the adhered particles. Observe from Figure 4.16.that, smaller particle radius (< 20 μm) requires a greater drag and lift forces than generated to overcome the particulate adhesive force. In order to supplement this short coming, a scouring pad was used (Figure 3.6). A correlation on the performance of the PV module under pre-exposure to soiling conditions, at soiling conditions and after the cleaning process, was done. The comparison between the three conditions quantified the effectiveness of the cleaning process. Figure 4.17 presents the I-V characteristic curves depicting the variance in performance under soiled and cleaned module with respect to pre-exposure performance.

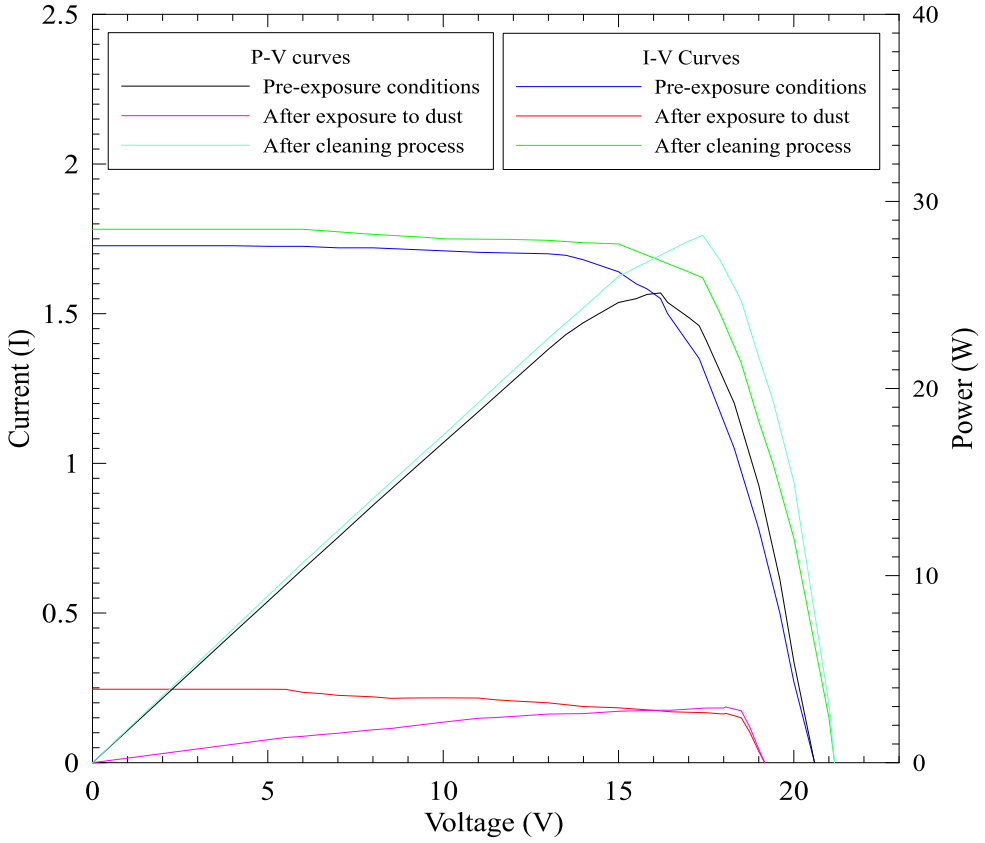

Figure 4.17: Normalized I-V and Power Curves for the Study Module before Exposure to Dust, under Soiling Conditions and after Cleaning by the Automated Self-Cleaning Model.

Upon cleaning, Figure 4.17 shows that the PV module's output voltage and current performance has improved, leading to an increase in output power. In comparison to the module rating prior to exposure to dust, P_{max} decreased by 88.13% as a result of exposure. Dust deposition lowers the photocurrent of solar cells by drastically reducing the incident radiation falling on them. Since dust deposits contribute less to the creation of photo-current due to the decreased incident radiation, they have a higher impact on current parameters than voltage parameters (Maghami *et al.*, 2016). The reason for this is that photon flux affects the generation rate. A prolonged dust exposure lowers the module's surface transmittance significantly, resulting in a lower generated maximum power (P_{max}). Optimal operation of PV system requires regular monitoring of the soiling levels and cleaning to avert deleterious effects. In addition to improved performance, it is worth noting that the performance of the cleaned

module exceeded the rated performance of the module before exposure to the ambient conditions.

Monitoring and cleaning of soiling levels is necessary to minimize negative impacts and ensure optimal operation of solar systems. P_{max} increased by 12.26% in relation to the rated power after the automatic self-cleaning operation, as seen by a leap in the voltage and current parameters in Figure 4.17. Figure 4.18 presents a more thorough examination of the extent of the dust influence on η determined using Eqn. 2.2.

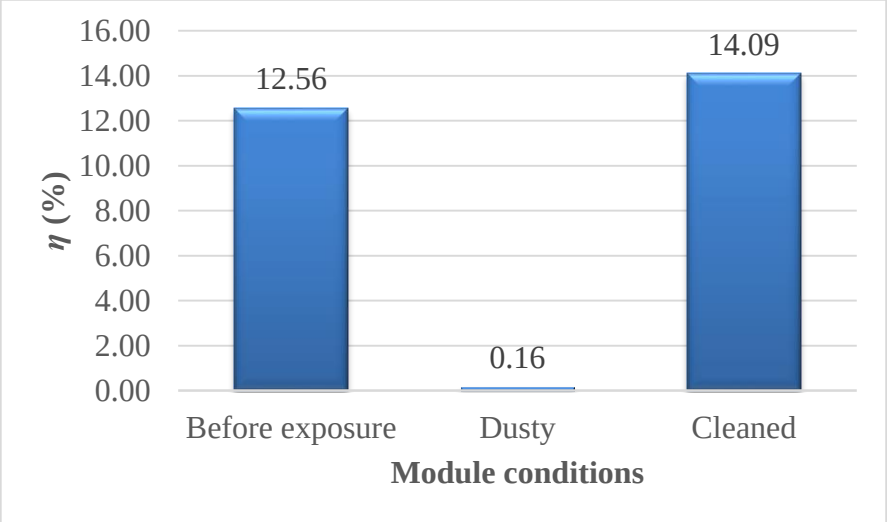

Figure 4.18: Power Conversion Efficiency (η) of the Study PV Module before Exposure to Dust, after Exposure and after Cleaning by the Automated Self-Cleaning Model.

In Figure 4.18, a significant decrease in photocurrent (η) is observed when the PV module is exposed to dust. This decline is attributed to the adhered dust particles obstructing, reflecting, and absorption of incident photon energy, which results in a decreased photo-current. On the other hand, a significant increase in η is observed after the PV module surface has been cleaned. Similarly, a slight increase in η from the reference rating is also noted. This increase is attributed to the cooling effect of the air and then water jets on the module surface, which decreases the bombardment of charge carriers and increases electron-hole recombination. Additionally, a cleaned

PV surface increases the transmission of incident radiation through the glass surface, which increases photon energy (Kata *et al.*, 2018).

4.6.2 The Automated Self-Cleaning Model's Energy Demand

Determining the cleaning model's feasibility requires a thorough examination of the energy requirement. Using the automated self-cleaning model, a cleaning cycle lasts 10 minutes, or 0.167 hours. This cleaning duration is a rough estimate of the longest cleaning cycle time based on field data made prior to the equipment being tested. The automated model's energy consumption is shown in Table 4.6.

Table 4-6: Automated PV Module's Self-Cleaning Model's Energy Demand

Item	Quantity	Voltage (V DC)	Power (W)	Time (hrs)	Demand Wh)
Air fan	3	12	9	0.083	2.25
Motor	1	12	144	0.167	24
Suction pump	1	12	60	0.083	5
TOTAL					31.25

As shown in Table 4.6, the total amount of energy needed for the cleaning procedure is 31.25 Wh. This indicates that every 10-minute (0.167-hour) cleaning session requires 2.604 Ah of battery capacity from a DC supply of 12 V. With a 90% efficiency at 50% D.O.D. and two days of autonomy, a fully charged 12 V 100 Ah battery (optional) may thus comfortably support five, ten-minute PV surface cleaning cycles. As a result, even while this energy can be drawn from the PV system's primary energy storage (batteries), the automatic self-cleaning model with battery storage can easily clean the dusty modules at night with little power outages. The system's economic lifespan can be established by analyzing the amount of time required for the cleaning cycle. Taking into account variations in the degree of soiling, the duration of the cleaning procedure may differ slightly. The time required

for each cycle will be roughly estimated at 0.5 hours in order to determine the system's lifespan. Consequently, assuming a 50% increase in demand, the brushless motors are estimated to run for 18 hours a year, or two cycles per month. This indicates that the brushless motors have a 56-year lifespan (estimated lifespan (1000 hours) / operating hours per year (18 hours)). On the other hand, because of wear and tear brought on by the stresses involved, the chain and the gears cannot tolerate this length of time (Lijesh *et al.*, 2018). For this reason, the minimum anticipated economic life of the system in this study was set at 10% of its lifespan. Therefore, it is anticipated that the automatic self-cleaning model in this study will have an economic life of 5.6 years which is also taken as its estimated project lifetime.

4.6.3 Economic Analysis of the Automated Self-Cleaning System

The viability of a system would be best determined by comparing its costs to an alternative method of solving the problem. For instance, the methods used in the cleaning of PV modules are to some extend manual and require trained staff. These methods pose challenges and enormous risks to the technicians especially when dealing with stand-alone solar PV systems. To avert these risks and costs to the consumer, an automated self -cleaning system would be ideal.

The evaluation of expenses incurred (capital costs) during the model's construction is crucial for ascertaining the system's economic feasibility. The device can easily and affordably clean a 100 Wp solar PV module, even though it was made for a 20 Wp module. Thus, ten of these self-cleaning models would be needed on the higher end of the scale when extrapolating the model's cost from a 100 Wp system to a 1 kWp PV system while accounting for economies of scale. To calculate the cost of a 1 kWp PV system, multiply the fabrication expenses of a unit self-cleaning model by 10, as shown in Table 4.7.

Table 4.7: Annual Economic Analysis of the Self-Cleaning Model for a 1 kWp PV System

Expected life of the self-cleaning system = 5.6 years			$r_n = 12.5\%$,	$I = 6.63\%$,	$r_r = 5.51\%$			
		Year						
	Item	**0**	**1**	**2**	**3**	**4**	**5**	**5.6**
	Air fans ($)	-10.00						
	Motor ($)	-20.00						
	Pulley system ($)	-5.50						
	Suction pump ($)	-5.00						
Costs	12 V 100 Ah Battery storage ($)	-45.00						
in U.S. Dollars ($)	m-Si solar module ($)	-15.00						
	Soft iron casing ($)	-15.00						
	Scourer ($)	-1.50	-1.50	-1.50	-1.50	-1.50	-1.50	-1.50
	2 mm 5 m long pipe ($)	-2.00						
	Installation of new Equipment ($)	-10.00						
	Training Course ($)	-5.00	-5.00					
Benefits/Savings	Increased energy generated (12.26% of 1 kWh) @ $ 0.229/kWh (KPLC)		28.08	27.52	26.71	25.67	24.42	23.10
	Increased energy demand per kWh		-0.43	-0.43	-0.43	-0.43	-0.43	-0.43

	(50% of 0.3125 kWh) @ $ 0.229/kWh* 12 months							
	Annual manual cleaning costs (twice a month) @ $ 0.72/W		720.00	720.00	720.00	720.00	720.00	720.00
	Total Cost ($) for 100 Wp system	-134.00						
	Future income $ per Kw	**-1340.00**	**741.15**	**745.59**	**744.78**	**743.74**	**742.50**	**741.17**
	Present Value $ per Kw		702.47	669.82	634.18	600.25	567.97	549.02
	Net Present Value (NPV)	2383.71						
	Profitability Index (PI)	**1.78**						
Amortization	Payment balance (dynamic)		-637.53	32.29	666.47	1266.72	1834.69	2383.71
	Amortization time (dynamic)	**1.95**	years					

The anticipated costs of cleaning the PV modules using manual cleaning methods on a monthly basis are contrasted with the capital expenses of creating and implementing the automated system in Table 4-7. For a 1 kWp system, the entire cost of designing, manufacturing, and installing the automated self-cleaning system is $1340. Which is computed for a 1 kWh system factoring in the annual m-Si PV module degradation rate of 0.99%, the extra energy output at 12.26% (section 4.6.1) is calculated (Ngure *et al.*, 2022).

The benefits of higher generation as a whole, computed using Kenya Power and Lighting Company's (KPLC) Small Commercial (SC) price of $ 0.229/kWh, come to $ 28.08 in the first year. However, as a result of the annual PV module degradation rate, these benefits decrease in the following years. Likewise, 1.872 kWh/year, or $ 0.43, is the estimated increase in energy demand for upscaling the model as a result of the 50% increase in cleaning time. Furthermore, the anticipated yearly cost of manual cleaning, which includes equipment purchase, comes from the monthly labor expenses incurred by engaging personnel to manually clean the dusty surfaces of solar PV modules twice a month. Comparatively, take note that the project's net present value (NPV) is $ 2383.71 which is more than the installation's entire cost. Based on Eqn. 3.7, the profitability index (PI) is 1.78, indicating that the project is profitable from an economic standpoint (Rodrigues *et al*., 2017; Zeraatpisheh *et al.*, 2018). According to Table 4.7, the project's discounted payback duration (dynamic amortization time) of 1.95 years, derived from Equation 3.8, means that the project will break even in around 1 year and 11 months, with investment earnings making up the remaining project term. Comparing the net present value (*NPV*), profitability index, and discounted payback period makes it evident that the automated self-cleaning system is more financially viable than the manual cleaning methods.

CHAPTER FIVE

CONCLUSIONS AND RECOMMENDATIONS

5.1 Conclusions

Module installation height, tilt angle and orientation with respect to ambient winds on PV module surfaces showed some significant effects on the dust deposition patterns. The observed dust deposit rate on solar PV surfaces was 14.05 g/m^2, 16.69 g/m^2, 19.875 g/m^2, 17.247 g/m^2, and 16.038 g/m^2 for sites 1, 2, 3, 4, and 5, respectively, per month. The deposition patterns were highly dictated by the winds blowing over the PV surfaces. For instance, an average wind speeds of 3.020 m/s, 2.926 m/s, 2.863 m/s, 2.952 m/s, and 2.948 m/s were recorded at sites 1, 2, 3, 4, and 5, respectively. The average wind speeds and ground cover at the sites had a positive effect on dust resuspension, resulting in a lower deposition rate at higher wind speeds and grass covered ground at site 1 and a higher deposition rate at lower wind speeds and bare ground at site 3 (Figure 4-3). The module tilt angle also had a significant impact on the deposition patterns, with site 4 having a higher deposition rate but higher wind speeds than site 2, which had a lower wind speed but a lower deposition rate. This is attributable to differences in tilt angle of 17^o and 8^o for sites 2 and 4, respectively.

In addition, north-facing glass slides in southerly winds at an installation height of less than 2.0 m had a higher dust deposition rate compared to the south-facing counterparts at the same installation height and tilt angle. A higher deposition rate was noted for an almost horizontal tilt (5^o). For ground mounted PV systems, regardless of orientation, an ideal height and tilt angle of 2.5 m and 15^o, respectively, were identified. For installation purposes, an increase in the tilt angle on the PV module installation is advocated but it is very important to note that the solar PV tilt angle is one of the main parameters in determining the amount of solar energy received from the sun. A combination of high wind speeds and the recommended module tilt angle would contribute immensely on the self-cleaning mechanisms for the loosely adhered dust particles. Advertently, the site-specific average wind speeds

were insufficient for resuspension of small particles (less than 500 μm) adhering to the surface of the PV module.

Dust characterization was determined based on elemental concentration, associated origins, and their contribution to overall degradation rates of maximum power (P_{max}) and conversion efficiency (η). Traces of anthropogenic particles on dust accumulated on PV module surfaces were found to have a significant effect on P_{max} and η, though the magnitude varied depending on the particle concentration. Biogenic and geogenic particles, combined with low deposition rates, had little effect on P_{max} and η. Similarly, the temperature coefficient $T_{C,V_{MPP}}$ was significantly affected by module temperature in the presence of dust. $T_{C,V_{MPP}}$ increased by 5.85%, 16.80%, 17.36%, 16.82%, and 5.62% in sites 1, 2, 3, 4, and 5, respectively. Consequently, dust accumulations on the surface of PV modules significantly reduce the current and voltage parameters. Moreover, PV modules should be installed away from potential sources of anthropogenic particles, which are primarily emitted by vehicles on the road.

Air jets corresponding to average speeds of 13.22 m/s were observed to generate on average a specific drag and lift force per unit area of 0.06 N/m^2 and 0.24 N/m^2, respectively. Similarly, water jets having on average, a speed of 3.86 m/s were found to generate a specific drag and lift force per unit area of 4.45 N/m^2 and 3.50 N/m^2, respectively. The resultant drag and lift forces per unit area generated by the automated self-cleaning model were found to be more than the particulate adhesive forces of the adhering dust particles on PV surfaces as observed in the study sites. Finally, the NPV and profitability index of the automated self-cleaning model compared to alternative manual cleaning methods was $ 2383.71 and 1.78, respectively. Similarly, the discounted payback period for the project was 1.95 years symbolizing economic viability of the automated self-cleaning model. The contributions arising and major findings emerging from this thesis can be summarized as follows.

1. The module placement with respect to ambient wind had significant effect on dust deposition patterns.

2. The rate of dust deposition on solar PV module surface had significant effects on the current parameters than voltage parameters, with major effects observed in sites 2, 3 and 4 where higher deposition rates were experienced.
3. Higher deposition rates were observed on leeward facing glass slides at an almost horizontal tilt as opposed to higher tilt angles. Conversely, windward facing glass slides recorded low deposition rates with preferred installation height of 2.5 m and a tilt angle of 15^{o} identified irrespective of the orientation.
4. Traces of anthropogenic particles on dust adhered on solar PV module surfaces were observed to have a higher deleterious effect on P_{max} and η compared to abundance of biogenic and geogenic dust particles, although the magnitude of the effect varied depending on particulate concentration.
5. The NPV and profitability index of the model was $ 2383.71 and 1.78, respectively, with a dynamic payback period of 1.95 years implying that the self-cleaning model's investment is economically viable.

5.2 Recommendations

Despite the promising results generated by aforementioned findings emerging from the study, we observed the following important issues that might be recommended for future work:

1. Further research to be extended to large-scale commercial solar PV projects in different parts of the country and the continent for comparison purposes.
2. Future experimental investigations could be carried out to incorporate machine learning and sensors to automatically initiate the cleaning process once sufficient dust accumulates the solar PV surfaces.
3. One challenge with almost all existing solar PV modules is the inability to incorporate self-cleaning mechanism at the design stage. In future, incorporation of the automated self-cleaning model in the design of PV modules as opposed to its existence as a separate entity incorporated at installation stage of PV modules is recommended. This will provide a tailor-made solution to soiling hence averting the deleterious effects of soiling on PV modules.

Considering the raised concerns, the study findings lend substantially to our understanding of how wind profiles, relative humidity, and module placement affect dust deposition on the surfaces of photovoltaic modules, and their overall performance reflecting realistic outdoor field conditions.

REFERENCES

Abdelaziz, G., Hichem, H., Chiheb, B. R., & Rached, G. (2021). Shading effect on the performance of a photovoltaic panel. *2021 IEEE 2nd International Conference on Signal, Control and Communication (SCC)*, 208–213. https://doi.org/10.1109/SCC53769.2021.9768356

Al-Badra, M. Z., Abd-Elhady, M. S., & Kandil, H. A. (2020). A novel technique for cleaning PV panels using antistatic coating with a mechanical vibrator. *Energy Reports*, *6*, 1633–1637. https://doi.org/10.1016/j.egyr.2020.06.020

Alnasser, T. M. A., Mahdy, A. M. J., Abass, K. I., Chaichan, M. T., & Kazem, H. A. (2020). Impact of dust ingredient on photovoltaic performance: An experimental study. *Solar Energy*, *195*, 651–659. https://doi.org/10.1016/j.solener.2019.12.008

Alrikabi, Dr. N. S. (2022). The profitability index and its impact on sustainable development decisions. *Journal of Economics, Finance and Management Studies*, *05*(10), 2897–2906. https://doi.org/10.47191/jefms/v5-i10-10

Al-Salaymeh, A. S., Al-Mansi, N. N., Muslih, I. M., Altaharwah, Y. A., & Al Smadi, W. Y. (2023). Electrostatic cleaning effect on the performance of PV modules in Jordan. *Cleaner Engineering and Technology*, *13*, 100606. https://doi.org/10.1016/j.clet.2023.100606

Apt, K. R. (2003). *Principles of constraint programming*. Cambridge University Press.

Azzouzi, M., Kirchartz, T., & Nelson, J. (2019). Factors Controlling Open-Circuit Voltage Losses in Organic Solar Cells. *Trends in Chemistry*, *1*(1), 49–62. https://doi.org/10.1016/j.trechm.2019.01.010

Bernal-Agustín, J. L., & Dufo-López, R. (2006). Economical and environmental analysis of grid connected photovoltaic systems in Spain. *Renewable Energy*, *31*(8), 1107–1128. https://doi.org/10.1016/j.renene.2005.06.004

Besson, P., Mu, C., Ram, G., Salgado, M., Escobar, R., & Platzer, W. (2017). *Long-Term Soiling Analysis for Three Photovoltaic Technologies in Santiago Region*. *7*(6), 1755–1760.

Calabokis, O. P., Nuñez de la Rosa, Y., Borges, P. C., & Cousseau, T. (2022). Effect of an Aftermarket Additive in Powertrain Wear and Fuel Consumption of Small-Capacity Motorcycles: A Lab and Field Study. *Lubricants*, *10*(7), 143. https://doi.org/10.3390/lubricants10070143

CBK. (2024). *CBK | Central Bank of Kenya*. https://www.centralbank.go.ke/

Ekanayake, N. I. K., Berry, J. D., & Harvie, D. J. E. (2021). Lift and drag forces acting on a particle moving in the presence of slip and shear near a wall. *Journal of Fluid Mechanics*, *915*, A103. https://doi.org/10.1017/jfm.2021.138

Elminir, H. K., Ghitas, A. E., Hamid, R. H., El-hussainy, F., Beheary, M. M., & Abdel-moneim, K. M. (2006). *Effect of dust on the transparent cover of solar collectors*. *47*, 3192–3203. https://doi.org/10.1016/j.enconman.2006.02.014

EPRA. (2024). *Energy & Petroleum Statistics Report 2023*. https://www.google.com/search?q=epra+2024+report&oq=epra&gs_lcrp=EgZjaHJvbWUqCAgAEEUYJxg7MggIABBFGCcYOzIOCAEQRRgnGDsYgAQYigUyBggCEEUYOzIMCAMQABgUGIcCGIAEMgcIBBAAGIAEMg0IBRAuGK8BGMcBGIAEMgYIBhBFGDwyBggHEEUYPNIBCDM1MTdqMGo0qAIAsAIA&sourceid=chrome&ie=UTF-8

Figgis, B., Goossens, D., Guo, B., & Ilse, K. (2019). Effect of tilt angle on soiling in perpendicular wind. *Solar Energy*, *194*, 294–301. https://doi.org/10.1016/j.solener.2019.10.062

Figgis, B., Guo, B., Javed, W., Ahzi, S., & Rémond, Y. (2018). Dominant environmental parameters for dust deposition and resuspension in desert climates. *Aerosol Science and Technology*, *52*(7), 788–798. https://doi.org/10.1080/02786826.2018.1462473

Fountoukis, C., Figgis, B., Ackermann, L., & Ayoub, M. A. (2018). Effects of atmospheric dust deposition on solar PV energy production in a desert environment. *Solar Energy*, *164*, 94–100. https://doi.org/10.1016/j.solener.2018.02.010

Ghosh, A., Sundaram, S., & Mallick, T. K. (2019). Colour properties and glazing factors evaluation of multicrystalline based semi-transparent Photovoltaic-vacuum glazing for BIPV application. *Renewable Energy*, *131*, 730–736. https://doi.org/10.1016/j.renene.2018.07.088

Gray, J. L. (2011). The Physics of the Solar Cell. In A. Luque & S. Hegedus (Eds.), *Handbook of Photovoltaic Science and Engineering* (pp. 82–129). John Wiley & Sons, Ltd. https://doi.org/10.1002/9780470974704.ch3

Green, M. A., Dunlop, E. D., Siefer, G., Yoshita, M., Kopidakis, N., Bothe, K., & Hao, X. (2023). Solar cell efficiency tables (Version 61). *Progress in Photovoltaics: Research and Applications*, *31*(1), 3–16. https://doi.org/10.1002/pip.3646

Hachicha, A. A., Al-Sawafta, I., & Said, Z. (2019). Impact of dust on the performance of solar photovoltaic (PV) systems under United Arab Emirates weather conditions. *Renewable Energy*, *141*, 287–297. https://doi.org/10.1016/j.renene.2019.04.004

Hanum, F., Desfitri, E., Hayakawa, Y., & Kambara, S. (2018). Preliminary Study on Additives for Controlling As, Se, B, and F Leaching from Coal Fly Ash. *Minerals*, *8*(11), 493. https://doi.org/10.3390/min8110493

Hegazy, A. A. (2001). Effect of dust accumulation on solar transmittance through glass covers of plate-type collectors. *Renewable Energy*, *22*(4), 525–540. https://doi.org/10.1016/S0960-1481(00)00093-8

Henry, C., & Minier, J.-P. (2014). Progress in particle resuspension from rough surfaces by turbulent flows. *Progress in Energy and Combustion Science*, *45*, 1–53. https://doi.org/10.1016/j.pecs.2014.06.001

Hudedmani, M. G., Joshi, G., Umayal, R. M., & Revankar, A. (2017). A Comparative Study of Dust Cleaning Methods for the Solar PV Panels. *Advanced Journal of Graduate Research*, *1*(1), 24–29. https://doi.org/10.21467/ajgr.1.1.24-29

Isaifan, R. J., Johnson, D., Ackermann, L., Figgis, B., & Ayoub, M. (2019). Evaluation of the adhesion forces between dust particles and photovoltaic module surfaces. *Solar Energy Materials and Solar Cells*, *191*, 413–421. https://doi.org/10.1016/j.solmat.2018.11.031

Jaiganesh, K., Bharath Simha Reddy, K., Shobhitha, B. K. D., & Dhanush Goud, B. (2022). Enhancing the efficiency of rooftop solar photovoltaic panel with simple cleaning mechanism. *Materials Today: Proceedings*, *51*, 411–415. https://doi.org/10.1016/j.matpr.2021.05.565

Jaszczur, M., Hassan, Q., Teneta, J., Styszko, K., Nawrot, W., & Hanus, R. (2018). Study of dust deposition and temperature impact on solar photovoltaic module. *MATEC Web of Conferences*, *240*, 04005. https://doi.org/10.1051/matecconf/201824004005

Jiang, Y., Lu, L., Ferro, A. R., & Ahmadi, G. (2017). Analyzing wind cleaning process on the accumulated dust on solar photovoltaic (PV) modules on fl at surfaces. *Solar Energy*, *August*, 0–1. https://doi.org/10.1016/j.solener.2017.08.083

Jiang, Y., Lu, L., Ferro, A. R., & Ahmadi, G. (2018). Analyzing wind cleaning process on the accumulated dust on solar photovoltaic (PV) modules on flat surfaces. *Solar Energy*, *159*, 1031–1036. https://doi.org/10.1016/j.solener.2017.08.083

Jory, S. R., Benamraoui, A., Boojihawon, D. R., & Madichie, N. O. (2016). *Net Present Value Analysis and the Wealth Creation Process: A Case Illustration*.

Karuma, A., Gachene, C., Msanya, B., Mtakwa, P., Amuri, N., & Gicheru, P. (2015). Soil Morphology, Physico—Chemical Properties and Classification of Typical Soils of Mwala District, Kenya. *International Journal of Plant & Soil Science*, *4*(2), 156–170. https://doi.org/10.9734/IJPSS/2015/13467

Kata, N., Soro, Y. M., Diouf, D., Darga, A., & Maiga, A. S. (2018). Temperature impact on dusty and cleaned photovoltaic module exposed in sub-Saharan outdoor conditions. *EPJ Photovoltaics*, *9*, 8. https://doi.org/10.1051/epjpv/2018007

Kazem, H. A., Chaichan, M. T., Al-Waeli, A. H. A., Sopian, K., & Darwish, A. S. K. (2021). Evaluation of Dust Elements on Photovoltaic Module Performance: An Experimental Study. *Renewable Energy and Environmental Sustainability*, *6*, 30. https://doi.org/10.1051/rees/2021027

KEBS. (2018). *KEBS PV Installattion Guidelines*. https://www.google.com/search?q=KEBS+pv+INSTALLATION+GUIDELINES&oq=KEBS+pv+INSTALLATION+GUIDELINES&gs_lcrp=EgZjaHJvbWUyBggAEEUYOTIHCAEQIRigAdIBCTEzNjk4ajBqN6gCALACAA&sourceid=chrome&ie=UTF-8#ip=1

Kok, J. F., Parteli, E. J. R., Michaels, T. I., & Karam, D. B. (2012). The physics of wind-blown sand and dust. *Reports on Progress in Physics*, *75*(10), 106901. https://doi.org/10.1088/0034-4885/75/10/106901

Lijesh, K. P., Khonsari, M. M., & Kailas, S. V. (2018). On the integrated degradation coefficient for adhesive wear: A thermodynamic approach. *Wear*, *408–409*, 138–150. https://doi.org/10.1016/j.wear.2018.05.004

Lima, J. D. D., Trentin, M. G., Oliveira, G. A., Batistus, D. R., & Setti, D. (2015). A systematic approach for the analysis of the economic viability of investment projects. *International Journal of Engineering Management and Economics*, *5*(1/2), 19. https://doi.org/10.1504/IJEME.2015.069887

Liu, C.-N., Chien, C.-L., Lo, C.-C., Lin, G.-Y., Chen, S.-C., & Tsai, C.-J. (2011). Drag Coefficient of a Spherical Particle Attached on the Flat Surface. *Aerosol and Air Quality Research*, *11*(5), 482–486. https://doi.org/10.4209/aaqr.2011.05.0069

Liu, D., Sun, Y., Wilson, R., & Wu, Y. (2020). Comprehensive evaluation of window-integrated semi-transparent PV for building daylight performance. *Renewable Energy*, *145*, 1399–1411. https://doi.org/10.1016/j.renene.2019.04.167

Lu, H., & Zhao, W. (2018). Effects of particle sizes and tilt angles on dust deposition characteristics of a ground-mounted solar photovoltaic system. *Applied Energy*, *220*, 514–526. https://doi.org/10.1016/j.apenergy.2018.03.095

Luque, E. G., Antonanzas-torres, F., & Escobar, R. (2018). E ff ect of soiling in bifacial PV modules and cleaning schedule optimization. *Energy Conversion and Management*, *174*(July), 615–625. https://doi.org/10.1016/j.enconman.2018.08.065

Machakos District Environmental Action Plan 2009-2013. (2013). Retrieved from https://www.nema.go.ke/images/Docs/Awarness%20Materials/NEAPS/machakos.pdf

Maghami, M. R., Hizam, H., Gomes, C., Radzi, M. A., Rezadad, M. I., & Hajighorbani, S. (2016). Power loss due to soiling on solar panel: A review. *Renewable and Sustainable Energy Reviews*, *59*, 1307–1316. https://doi.org/10.1016/j.rser.2016.01.044

Mahmud, S., Al Masum Bhuiyan, M., Sarmin, N., Elahee, S., 1 Department of Computational Science, University of Texas at El Paso, 500 w university avenue, El Paso, TX 79912, USA, 2 Department of Computer Science, University of Texas at El Paso, 500 w university avenue, El Paso, TX 79912, USA, & 3 Department of Chemistry, University of Delaware, Newark, DE 19716, USA. (2020). Study of wind speed and relative humidity using stochastic technique in a semi-arid climate region. *AIMS Environmental Science*, *7*(2), 156–173. https://doi.org/10.3934/environsci.2020010

Mani, M., & Pillai, R. (2010). Impact of dust on solar photovoltaic (PV) performance: Research status, challenges and recommendations. *Renewable and Sustainable Energy Reviews*, *14*(9), 3124–3131. https://doi.org/10.1016/j.rser.2010.07.065

Marques, R. A., Torres, J. P. N., & De Melo Cunha, J. P. (2022). A Photovoltaic Technology Review: History, Fundamentals and Applications. *Energies*, *15*(5), 1823. https://doi.org/10.3390/en15051823

Matius, M. E., Ismail, M. A., Farm, Y. Y., Amaludin, A. E., Radzali, M. A., Fazlizan, A., & Muzammil, W. K. (2021). On the Optimal Tilt Angle and Orientation of an On-Site Solar Photovoltaic Energy Generation System for Sabah's Rural Electrification. *Sustainability*, *13*(10), 5730. https://doi.org/10.3390/su13105730

Memiche, M., Bouzian, C., Benzahia, A., & Moussi, A. (2020). Effects of dust, soiling, aging, and weather conditions on photovoltaic system performances in a Saharan environment—Case study in Algeria. *Global Energy Interconnection*, *3*(1), 60–67. https://doi.org/10.1016/j.gloei.2020.03.004

Menoufi, K., Farghal, H. F. M., Farghali, A. A., & Khedr, M. H. (2017). Dust accumulation on photovoltaic panels: A case study at the East Bank of the Nile (Beni-Suef, Egypt). *Energy Procedia*, *128*, 24–31. https://doi.org/10.1016/j.egypro.2017.09.010

Meral, M., & Din, F. (2010). Critical Factors that Affecting Efficiency of Solar Cells. *Smart Grid and Renewable Energy*, *1*(1), 47. https://doi.org/10.4236/sgre.2010.11007

Mohammad Bagher, A. (2015). Types of Solar Cells and Application. *American Journal of Optics and Photonics*, *3*(5), 94. https://doi.org/10.11648/j.ajop.20150305.17

Moutinho, H. R., Jiang, C.-S., To, B., Perkins, C., Muller, M., Al-Jassim, M. M., & Simpson, L. (2017). Adhesion mechanisms on solar glass: Effects of relative humidity, surface roughness, and particle shape and size. *Solar Energy Materials and Solar Cells*, *172*, 145–153. https://doi.org/10.1016/j.solmat.2017.07.026

Mustafa, R. J., Gomaa, M. R., Al-Dhaifallah, M., & Rezk, H. (2020). Environmental Impacts on the Performance of Solar Photovoltaic Systems. *Sustainability*, *12*(2), 608. https://doi.org/10.3390/su12020608

Ndeto, M. P., Wekesa, D. W., Kinyua, R., & Njoka, F. (2020). Investigation into the effects of the earth's magnetic field on the conversion efficiency of solar cells. *Renewable Energy*, *159*, 184–194. https://doi.org/10.1016/j.renene.2020.05.143

Ngure, S. M., Makokha, A. B., Ataro, E. O., & Adaramola, M. S. (2022). Degradation analysis of Solar photovoltaic module under warm semiarid and tropical savanna climatic conditions of East Africa. *International Journal of Energy and Environmental Engineering*, *13*(2), 431–447. https://doi.org/10.1007/s40095-021-00454-5

Ngwashi, D., & Tsafack, P. (2023). Enhancement of Ready-Made Silicon Photovoltaic Panels' Field Performance—A Review. *American Journal of Electrical Power and Energy Systems*, *12*, 59–67. https://doi.org/10.11648/j.epes.20231204.11

NREL. (2024). *Best Research-Cell Efficiency Chart*. https://www.nrel.gov/pv/cell-efficiency.html

Omuto, C. T. (2013). Major Soil and Data Types in Kenya. In *Developments in Earth Surface Processes* (Vol. 16, pp. 123–132). Elsevier. https://doi.org/10.1016/B978-0-444-59559-1.00011-6

Özönder, Ş., Ünlü, C., Güleryüz, C., & Trabzon, L. (2023). Doped Graphene Quantum Dots UV–vis Absorption Spectrum: A High-Throughput TDDFT

Study. *ACS Omega*, *8*(2), 2112–2118. https://doi.org/10.1021/acsomega.2c06091

Pandey, A., & Singh, D. K. (2016). *Modelling of Photovoltaic Solar Panel for Maximum Power Point Tracking*. *5*(5), 2015–2017.

Pastuszak, J., & Węgierek, P. (2022). Photovoltaic Cell Generations and Current Research Directions for Their Development. *Materials*, *15*(16), 5542. https://doi.org/10.3390/ma15165542

Pennetta, S., Yu, S., Borghesani, P., Cholette, M., Barry, J., & Guan, Z. (2016). *An investigation on factors influencing dust accumulation on CSP mirrors*. 070024. https://doi.org/10.1063/1.4949171

Premono, B. S., Tjahjana, D. D. D. P., & Hadi, S. (2017). *Wind energy potential assessment to estimate performance of selected wind turbine in northern coastal region of Semarang-Indonesia*. 030026. https://doi.org/10.1063/1.4968279

Quan, Y.-Y., Zhang, L.-Z., Qi, R.-H., & Cai, R.-R. (2016). Self-cleaning of Surfaces: The Role of Surface Wettability and Dust Types. *Scientific Reports*, *6*(1), 38239. https://doi.org/10.1038/srep38239

Quansah, D. A., & Adaramola, M. S. (2018). Ageing and degradation in solar photovoltaic modules installed in northern Ghana. *Solar Energy*, *173*, 834–847. https://doi.org/10.1016/j.solener.2018.08.021

Rahman, M. M., Hasanuzzaman, M., & Rahim, N. A. (2015). Effects of various parameters on PV-module power and efficiency. *Energy Conversion and Management*, *103*, 348–358. https://doi.org/10.1016/j.enconman.2015.06.067

Rahman, M. S., Kumar, P., Ullah, M., Jolly, Y. N., Akhter, S., Kabir, J., Begum, B. A., & Salam, A. (2021). Elemental analysis in surface soil and dust of roadside academic institutions in Dhaka city, Bangladesh and their impact on human health. *Environmental Chemistry and Ecotoxicology*, *3*, 197–208. https://doi.org/10.1016/j.enceco.2021.06.001

Ramgolam, Y. K., & Soyjaudah, K. M. S. (2018). Modelling the impact of spectral irradiance and average photon energy on photocurrent of solar modules. *Solar Energy*, *173*, 1058–1064. https://doi.org/10.1016/j.solener.2018.08.055

Rane, Ms. M. S. (2019). A Review on Solar Panel Cleaning Techniques and Systems. *International Journal for Research in Applied Science and Engineering Technology*, *7*(11), 360–365. https://doi.org/10.22214/ijraset.2019.11057

Rastello, M., Marié, J.-L., & Lance, M. (2011). Drag and lift forces on clean spherical and ellipsoidal bubbles in a solid-body rotating flow. *Journal of Fluid Mechanics*, *682*, 434–459. https://doi.org/10.1017/jfm.2011.240

Rehman, F., Syed, I. H., Khanam, S., Ijaz, S., Mehmood, H., Zubair, M., Massoud, Y., & Mehmood, M. Q. (2023). Fourth-generation solar cells: A review. *Energy Advances*, *2*(9), 1239–1262. https://doi.org/10.1039/D3YA00179B

Rodrigues, S., Chen, X., & Morgado-Dias, F. (2017). Economic analysis of photovoltaic systems for the residential market under China's new regulation. *Energy Policy*, *101*, 467–472. https://doi.org/10.1016/j.enpol.2016.10.039

Rühle, S. (2016). Tabulated values of the Shockley–Queisser limit for single junction solar cells. *Solar Energy*, *130*, 139–147. https://doi.org/10.1016/j.solener.2016.02.015

Saradhi, I. V., Sandeep, P., & Pandit, G. G. (2014). Assessment of elemental contamination in road dust using EDXRF. *Journal of Radioanalytical and Nuclear Chemistry*, *302*(3), 1377–1383. https://doi.org/10.1007/s10967-014-3550-y

Sayyah, A., Horenstein, M. N., & Mazumder, M. K. (2014). Energy yield loss caused by dust deposition on photovoltaic panels. *Solar Energy*, *107*, 576–604. https://doi.org/10.1016/j.solener.2014.05.030

Schill, C., Brachmann, S., & Koehl, M. (2015). Impact of soiling on IV-curves and efficiency of PV-modules. *Solar Energy*, *112*, 259–262. https://doi.org/10.1016/j.solener.2014.12.003

Schwela, Lidia Morawska, & Dimitrios Kotzias (Eds.). (2002). *Guidelines for Concentration and Exposure-Response Measurement of Fine and Ultra-Fine Particulate Matter for use in Epidemiological Studies*. World Heath Organization. https://citeseerx.ist.psu.edu/viewdoc/download?doi=10.1.1.385.507&rep=rep1&type=pdf

Shaju, A., & Chacko, R. (2018). Soiling of photovoltaic modules- Review. *IOP Conference Series: Materials Science and Engineering*, *396*, 012050. https://doi.org/10.1088/1757-899X/396/1/012050

Simsek, E., Williams, M. J., & Pilon, L. (2021). Effect of dew and rain on photovoltaic solar cell performances. *Solar Energy Materials and Solar Cells*, *222*, 110908. https://doi.org/10.1016/j.solmat.2020.110908

Sprovieri, F., & Pirrone, N. (2008). Particle Size Distributions and Elemental Composition of Atmospheric Particulate Matter in Southern Italy. *Journal of the Air & Waste Management Association*, *58*(6), 797–805. https://doi.org/10.3155/1047-3289.58.6.797

Stovern, M., Guzmán, H., Rine, K., Felix, O., King, M., Ela, W., Betterton, E., & Sáez, A. (2016). Windblown Dust Deposition Forecasting and Spread of Contamination around Mine Tailings. *Atmosphere*, *7*(2), 16. https://doi.org/10.3390/atmos7020016

Syafiq, A., Pandey, A. K., Adzman, N. N., & Rahim, N. A. (2018). Advances in approaches and methods for self-cleaning of solar photovoltaic panels. *Solar Energy*, *162*, 597–619. https://doi.org/10.1016/j.solener.2017.12.023

Tabatabaei, S. A., Formolo, D., & Treur, J. (2017). ScienceDirect ScienceDirect Analysis of performance degradation of domestic monocrystalline photovoltaic systems for a real-world case. *Energy Procedia*, *128*, 121–129. https://doi.org/10.1016/j.egypro.2017.09.025

Tan, C. L. C., Gao, S., Wee, B. S., Asa-Awuku, A., & Thio, B. J. R. (2014). Adhesion of Dust Particles to Common Indoor Surfaces in an Air-Conditioned Environment. *Aerosol Science and Technology*, *48*(5), 541–551. https://doi.org/10.1080/02786826.2014.898835

Thongsuwan, W., Sroila, W., Kumpika, T., Kantarak, E., & Singjai, P. (2022). Antireflective, photocatalytic, and superhydrophilic coating prepared by facile sparking process for photovoltaic panels. *Scientific Reports*, *12*(1), 1675. https://doi.org/10.1038/s41598-022-05733-7

Towett, E. K., Shepherd, K. D., Tondoh, J. E., Winowiecki, L. A., Lulseged, T., Nyambura, M., Sila, A., Vågen, T.-G., & Cadisch, G. (2015). Total elemental composition of soils in Sub-Saharan Africa and relationship with soil forming

factors. *Geoderma Regional*, *5*, 157–168. https://doi.org/10.1016/j.geodrs.2015.06.002

Traub, L. W. (2012). High-Incidence Airfoil Lift and Drag Estimates. *Journal of Aircraft*, *49*(1), 311–314. https://doi.org/10.2514/1.C031160

Vågen, T.-G., Winowiecki, L. A., Desta, L., Tondoh, E. J., Weullow, E., Shepherd, K., & Sila, A. (2020). *Mid-Infrared Spectra (MIRS) from ICRAF Soil and Plant Spectroscopy Laboratory: Africa Soil Information Service (AfSIS) Phase I 2009-2013* [dataset]. World Agroforestry (ICRAF). https://doi.org/10.34725/DVN/QXCWP1

Vanegas, S., Trejos, E. M., Aristizábal, B. H., Pereira, G. M., Hernández, J. M., Murillo, J. H., Ramírez, O., Amato, F., Silva, L. F. O., Rojas, N. Y., Zafra, C., & Pachón, J. E. (2021). Spatial Distribution and Chemical Composition of Road Dust in Two High-Altitude Latin American Cities. *Atmosphere*, *12*(9), 1109. https://doi.org/10.3390/atmos12091109

Wang, R., Li, Q., Zhou, N., Chang, C., Guo, Z., & Li, J. (2019). Effect of wind speed on aggregate size distribution of windblown sediment. *Aeolian Research*, *36*, 1–8. https://doi.org/10.1016/j.aeolia.2018.10.001

Yilbas, B. S., Abubakar, A. A., Al-Qahtani, H., Mohammed, A. S., & Al-Sharafi, A. (2021). A novel method for dust mitigation from PV cell surfaces. *Solar Energy*, *225*, 708–717. https://doi.org/10.1016/j.solener.2021.07.068

Yosri, M. H., Muhamad, P., Ismail, M. A., & Yatim, N. H. M. (2018). Air ionizer application for electrostatic discharge (ESD) dust removal in automotive painting industry. *IOP Conference Series: Materials Science and Engineering*, *290*, 012051. https://doi.org/10.1088/1757-899X/290/1/012051

Zeedan, A., Barakeh, A., Al-Fakhroo, K., Touati, F., & Gonzales, A. S. P. (2021). Quantification of PV Power and Economic Losses Due to Soiling in Qatar. *Sustainability*, *13*(6), 3364. https://doi.org/10.3390/su13063364

Zeraatpisheh, M., Arababadi, R., & Saffari Pour, M. (2018). Economic Analysis for Residential Solar PV Systems Based on Different Demand Charge Tariffs. *Energies*, *11*(12), 3271. https://doi.org/10.3390/en11123271

Zhao, P. J., & Yu, Y. (2014). Brushless DC Motor Fundamentals Application Note. *Monolithicpower*.

APPENDICES

Appendix I: Contribution of the Thesis

a) **M. Paul Ndeto,** D. Wafula Wekesa, F. Njoka, and R. Kinyua (2022). Correlating dust deposits with wind speeds and relative humidity to overall performance of crystalline silicon solar cells: An experimental study of Machakos County, Kenya, *Solar Energy*, vol. 246, pp. 203–215, Nov. 2022, doi: 10.1016/j.solener.2022.09.050. (Elsevier)

Solar Energy 246 (2022) 203–215

Contents lists available at ScienceDirect

Solar Energy

journal homepage: www.elsevier.com/locate/solener

Correlating dust deposits with wind speeds and relative humidity to overall performance of crystalline silicon solar cells: An experimental study of Machakos County, Kenya

Martin Paul Ndeto [a,*], David Wafula Wekesa [b,c], Francis Njoka [d], Robert Kinyua [e]

[a] Institute of Energy and Environmental Technology, Jomo Kenyatta University of Agriculture and Technology, P.O. Box 62000-00200, Nairobi, Kenya
[b] Department of Physics, Multimedia University of Kenya, P.O BOX 15653- 00503, Nairobi, Kenya
[c] Renewable Energy Research Consortium, Multimedia University of Kenya, P.O BOX 15653- 00503, Nairobi, Kenya
[d] Department of Energy Technology, Kenyatta University, P.O BOX 43844- 00100, Nairobi, Kenya
[e] Department of Physics, Jomo Kenyatta University of Agriculture and Technology, P.O. Box 62000-00200, Nairobi, Kenya

ARTICLE INFO

Keywords:
Photovoltaics
Wind profile
Humidity
Dust deposits
Adhesive forces
PV output parameters

ABSTRACT

Solar Photovoltaics is one of the budding technologies widely acknowledged as a solution to energy poverty. This is due to its high reliability, long life and automatic operation at low maintenance requirements even though handicapped by its low conversion efficiency and high capital costs. This study investigates the influence of wind profiles, relative humidity and module siting on dust deposition on the surfaces of photovoltaic modules hence its overall performance in an outdoor setup. A significant decrease in short circuit current density (J_{SC}), maximum current density (J_{MPP}), and voltage at maximum power point (V_{MPP}) due to dust deposits on the surface of the PV module are observed. The modules peak power (P_{max}) degradation rate after a fortnight is observed to be higher (4.4 %) for sites experiencing a higher temperature coefficient (T_c) for V_{MPP} as a consequence of temperature effects of soiling, lower wind speeds and a higher relative humidity. A lower deposition rate is observed in sites experiencing higher wind speeds and a higher module's tilt angle thus experiencing a lower effect on the reduction of current and voltage parameters. Similarly, the site-specific average wind speeds were inadequate for complete particulate resuspension of small sized particles (less than 500 μm) adhering to PV module surface. Therefore, dust accumulations on the surface of PV modules have significant deleterious effects on the current and voltage parameters.

b) **Ndeto, M. P.**, Wekesa, D. W., Njoka, F., & Kinyua, R. (2023). Aeolian dust distribution, elemental concentration, characteristics and its effects on the conversion efficiency of crystalline silicon solar cells. *Renewable Energy*, *208*, 481–491. https://doi.org/10.1016/j.renene.2023.03.065 (Elsevier)

Renewable Energy 208 (2023) 481–491

Contents lists available at ScienceDirect

Renewable Energy

journal homepage: www.elsevier.com/locate/renene

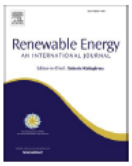

Aeolian dust distribution, elemental concentration, characteristics and its effects on the conversion efficiency of crystalline silicon solar cells

Martin Paul Ndeto [a,*], David Wafula Wekesa [b,c], Francis Njoka [d], Robert Kinyua [e]

[a] Institute of Energy and Environmental Technology, Jomo Kenyatta University of Agriculture and Technology, P.O. Box 62000-00200, Nairobi, Kenya
[b] Department of Physics, Multimedia University of Kenya, P.O BOX 15653-00503, Nairobi, Kenya
[c] Renewable Energy Research Consortium, Multimedia University of Kenya, P.O BOX 15653-00503, Nairobi, Kenya
[d] Department of Energy Technology, Kenyatta University, P.O BOX 43844-00100, Nairobi, Kenya
[e] Department of Physics, Jomo Kenyatta University of Agriculture and Technology, P.O. Box 62000-00200, Nairobi, Kenya

ARTICLE INFO

Keywords:
Anthropogenic particles
Conversion efficiency
Dust deposits
Elemental analysis
Enrichment factor

ABSTRACT

Exposure of PV modules to ambient environmental conditions like dust deposits, has some deleterious effects on peak power (P_{max}) and overall conversion efficiency (η). This study investigates the effect of module height, tilt, and orientation on the rate of dust deposition on the surfaces of PV modules. Consequently, the effect of different dust categories on P_{max} and η are investigated. North facing module surfaces are observed to exhibit higher deposition rates in southerly winds. A significant decrease in conversion efficiency of 1.30%, 1.74%, 4.05%, 2.74% and 1.38% after a fortnight are observed in modules installed in five randomly selected study sites. A higher decrease in efficiency on average after a fortnight is observed in sites having traces of anthropogenic particles on dust samples collected from the PV surfaces with minimal effects observed in sites having biogenic and geogenic particles. Abundance of anthropogenic dust particles coupled with mild tilt and leeward orientation led to a higher maximum power and efficiency degradation rate.

Go to Settings to activate Win

Appendix II: Automated self-cleaning mechanism link https://photos.app.goo.gl/HsWfkVaMDZJ91PXR9

Appendix III: Solar Cells conversion efficiencies

Appendix III-1: Confirmed single-junction terrestrial cell and sub-module efficiencies measured under the global AM1.5 spectrum (1000 W/m2) at 25 (IEC 60904-3: 2008 or ASTM G-173-03 global) (Green et al., 2023)

Classification	Efficiency (%)	Area (cm^2)	V_{oc} (V)	J_{sc} (mA/cm^2)	Fill factor (%)	Test centre (date)	Description
Silicon							
Si (crystalline cell)	**26.8 ± 0.4[a]**	**274.4 (t)**	**0.7514**	**41.45[b]**	**86.1**	**ISFH (10/22)**	**LONGi, n-type HJT[3]**
Si (DS wafer cell)	24.4 ± 0.3[a]	267.5 (t)	0.7132	41.47[c]	82.5	ISFH (8/20)	Jinko Solar, n-type
Si (thin transfer submodule)	21.2 ± 0.4	239.7 (ap)	0.687[d]	38.50[d,e]	80.3	NREL (4/14)	Solexel (35 μm thick)[4]
Si (thin film minimodule)	10.5 ± 0.3	94.0 (ap)	0.492[d]	29.7[d,f]	72.1	FhG-ISE (8/07)	CSG Solar (<2 μm on glass)[5]
III-V Cells							
GaAs (thin film cell)	29.1 ± 0.6	0.998 (ap)	1.1272	29.78[g]	86.7	FhG-ISE (10/18)	Alta Devices[6]
GaAs (multicrystalline)	18.4 ± 0.5	4.011 (t)	0.994	23.2	79.7	NREL (11/95)	RTI, Ge substrate[7]
InP (crystalline cell)	24.2 ± 0.5[h]	1.008 (ap)	0.939	31.15[i]	82.6	NREL (3/13)	NREL[8]
Thin Film Chalcogenide							
CIGS (cell) (Cd-free)	23.35 ± 0.5	1.043 (da)	0.734	39.58[j]	80.4	AIST (11/18)	Solar Frontier[9]
CIGSSe (submodule)	19.8 ± 0.5	665.4 (ap)	0.688	37.96[k]	75.9	NREL (12/21)	Avancis, 110 cells[10]
CdTe (cell)	21.0 ± 0.4	1.0623 (ap)	0.8759	30.25[e]	79.4	Newport (8/14)	First Solar, on glass[11]
CZTSSe (cell)	11.3 ± 0.3	1.1761 (da)	0.5333	33.57[g]	63.0	Newport (10/18)	DGIST, Korea[12]
CZTS (cell)	10.0 ± 0.2	1.113 (da)	0.7083	21.77[i]	65.1	NREL (3/17)	UNSW[13]
Amorphous/Microcrystalline							
Si (amorphous cell)	10.2 ± 0.3[l,h]	1.001 (da)	0.896	16.36[e]	69.8	AIST (7/14)	AIST[14]
Si (microcrystalline cell)	11.9 ± 0.3[h]	1.044 (da)	0.550	29.72[i]	75.0	AIST (2/17)	AIST[15]
Perovskite							
Perovskite (cell)	23.7 ± 0.5[m]	1.062 (da)	1.213	24.99[k]	78.4	NPVM (5/22)	U.Sci.Tech., Hefei[16]
Perovskite (minimodule)	**22.4 ± 0.5[m]**	**26.02 (da)**	**1.127[d]**	**25.61[d,b]**	**77.6**	**NPVM (7/22)**	**EPFLSion/NCEPU, 8 cells[17]**
Dye sensitised							
Dye (cell)	11.9 ± 0.4[n]	1.005 (da)	0.744	22.47[o]	71.2	AIST (9/12)	Sharp[18,19]
Dye (minimodule)	10.7 ± 0.4[n]	26.55 (da)	0.754[d]	20.19[d,p]	69.9	AIST (2/15)	Sharp, 7 serial cells[18,19]
Dye (submodule)	8.8 ± 0.3[n]	398.8 (da)	0.697[d]	18.42[d,q]	68.7	AIST (9/12)	Sharp, 26 serial cells[18,19]
Organic							
Organic (cell)	15.2 ± 0.2[h,r]	1.015 (da)	0.8467	24.24[c]	74.3	FhG-ISE (10/20)	Fraunhofer ISE[20]
Organic (minimodule)	14.5 ± 0.3[r]	19.31 (da)	0.8518[d]	23.51[d,k]	72.5	JET (12/21)	ZJU/Microquanta, 7 cells[21]
Organic (submodule)	11.7 ± 0.2[r]	203.98 (da)	0.8177[d]	20.68[d,s]	69.3	FhG-ISE (10/19)	ZAE Bayern, 33 cells[22]

Abbreviations: (ap), aperture area; AIST, Japanese National Institute of Advanced Industrial Science and Technology; a-Si, amorphous silicon/hydrogen alloy; CIGS, $CuIn_{1-y}Ga_ySe_2$; CZTS, Cu_2ZnSnS_4; CZTSSe, $Cu_2ZnSnS_{4-y}Se_y$; (da), designated illumination area; DS, directionally solidified (including mono cast and

multicrystalline); FhG-ISE, Fraunhofer Institut für Solare Energiesysteme; nc-Si, nanocrystalline or microcrystalline silicon; (t), total area.

Appendix III-2: "Notable exceptions" for single-junction cells and sub-modules: "Top dozen" confirmed results, not class records, measured under the global AM 1.5 spectrum (1000 Wm^{-2}) at 25ºC (IEC 60904-3: 2008 or ASTM G-173-03 global) (Green et al., 2023).

Classification	Efficiency (%)	Area (cm^2)	V_{oc} (V)	J_{sc} (mA/cm^2)	Fill factor (%)	Test centre (date)	Description
Cells (silicon)							
Si (crystalline)	25.0 ± 0.5	4.00 (da)	0.706	42.7[a]	82.8	Sandia (3/99)	UNSW, p-type PERC[29]
Si (crystalline)	25.8 ± 0.5[b]	4.008 (da)	0.7241	42.87	83.1	FhG-ISE (7/17)	FhG-ISE, n-type TOPCon[30]
Si (crystalline)	26.0 ± 0.5[b]	4.015 (da)	0.7323	42.05[d]	84.3	FhG-ISE (11/19)	FhG-ISE, p-type TOPCon
Si (crystalline)	26.7 ± 0.5	79.0 (da)	0.738	42.65[f]	84.9	AIST (3/17)	Kaneka, n-type rear IBC[32]
Si (crystalline)	26.1 ± 0.3[b]	3.9857 (da)	0.7266	42.62[e]	84.3	ISFH (2/18)	ISFH, p-type rear IBC[31]
Si (large crystalline)	24.0 ± 0.3[k]	244.59 (t)	0.6940	41.58[h]	83.3	ISFH (7/19)	LONGi, p-type PERC[33]
Si (large crystalline)	25.3 ± 0.4[i]	268.0 (t)	0.7214	42.07[i]	83.4	ISFH (11/21)	Jinko, n-type TOPCon[34]
Si (large crystalline)	**26.6 ± 0.4[k]**	**274.1 (t)**	**0.7513**	**41.30[j]**	**85.6**	**ISFH (10/22)**	**LONGi, p-type HJT[35]**
Si (large crystalline)	26.6 ± 0.5	179.74 (da)	0.7403	42.5[f]	84.7	FhG-ISE (11/16)	Kaneka, n-type rear IBC[32]
Cells (III-V)							
GaInP	22.0 ± 0.3[b]	0.2502 (ap)	1.4695	16.63[m]	90.2	NREL (1/19)	NREL, rear HJ, strained AlInP[36]
Cells (chalcogenide)							
CdTe (thin-film)	22.1 ± 0.5	0.4798 (da)	0.8872	31.69[n]	78.5	Newport (11/15)	First Solar on glass[37]
CZTSSe (thin-film)	13.0 ± 0.1	0.1072 (ap)	0.5294	33.58[o]	72.9	NREL (6/21)	NJUPT (10% Ag)[38]
CZTS (thin-film)	11.0 ± 0.2	0.2339 (da)	0.7306	21.74[f]	69.3	NREL (3/17)	UNSW on glass[39]
Cells (other)							
Perovskite (thin-film)	25.7 ± 0.8[p,q]	0.09597 (ap)	1.1790	25.80[j]	84.6	Newport (11/21)	UNIST Ulsan[40]
Organic (thin-film)	18.2 ± 0.2[r]	0.0322 (da)	0.8965	25.72[h]	78.9	NREL (10/20)	SJTU Shanghai/Beihang U.
Dye sensitised	12.25 ± 0.4[s]	0.0963 (ap)	1.0203	15.17[d]	79.1	Newport (8/19)	EPFL[41]

Abbreviations: AIST - Japanese National Institute of Advanced Industrial Science and Technology; (ap),aperture area; CIGSSe, CuInGaSSe; CZTSSe, $Cu_2ZnSnS_{4-y}Se_y$; CZTS, Cu_2ZnSnS_4; (da), designated illumination area; DS, directionally solidified (including mono cast and multicrystalline); FhG-ISE, Fraunhofer-Institut für Solare Energiesysteme; ISFH, Institute for Solar Energy Research, Hamelin; NREL, National Renewable Energy Laboratory; (t), total area.

Appendix III-3: Confirmed multiple-junction terrestrial cell and sub-module efficiencies measured under the global AM1.5 spectrum (1000 W/m^2) at 25ºC (IEC 60904-3: 2008 or ASTM G-173-03 global)

Classification	Efficiency (%)	Area (cm^2)	Voc (V)	Jsc (mA/cm^2)	Fill factor (%)	Test centre (date)	Description
III-V Multijunctions							
5 junction cell (bonded) (2.17/1.68/1.40/1.06/.73 eV)	38.8 ± 1.2	1.021 (ap)	4.767	9.564	85.2	NREL (7/13)	Spectrolab, 2-terminal
InGaP/GaAs/InGaAs	37.9 ± 1.2	1.047 (ap)	3.065	14.27[a]	86.7	AIST (2/13)	Sharp, 2 term.[42]
GaInP/GaAs (monolithic)	32.8 ± 1.4	1.000 (ap)	2.568	14.56[b]	87.7	NREL (9/17)	LG Electronics, 2 term.
Multijunctions with c-Si							
GaInP/GaInAsP/Si (wafer bonded)	35.9 ± 1.3[c]	3.987 (ap)	3.248	13.11[d]	84.3	FhG-ISE (4/20)	Fraunhofer ISE, 2-term.[43]
GaInP/GaAs/Si (mech. stack)	35.9 ± 0.5[c]	1.002 (da)	2.52/0.681	13.6/11.0	87.5/78.5	NREL (2/17)	NREL/CSEM/ EPFL, 4-term.[44]
GaInP/GaAs/Si (monolithic)	25.9 ± 0.9[c]	3.987 (ap)	2.647	12.21[e]	80.2	FhG-ISE (6/20)	Fraunhofer ISE, 2-term.[45]
GaAsP/Si (monolithic)	23.4 ± 0.3	1.026 (ap)	1.732	17.34[f]	77.7	NREL (5/20)	OSU/UNSW/ SolAero, 2-term[46]
GaAs/Si (mech. stack)	32.8 ± 0.5[c]	1.003 (da)	1.09/0.683	28.9/11.1[g]	85.0/79.2	NREL (12/16)	NREL/CSEM/ EPFL, 4-term.[44]
Perovskite/Si	**31.3 ± 0.3[h]**	**1.1677 (da)**	**1.9131**	**20.47[i]**	**79.8**	**NREL (6/22)**	**EPFL/CSEM, 2-term.[47]**
GaInP/GaInAs/Ge; Si (spectral split minimodule)	34.5 ± 2.0	27.83 (ap)	2.66/0.65	13.1/9.3	85.6/79.0	NREL (4/16)	UNSW/Azur/ Trina, 4-term.[48]
Other Multijunctions							
Perovskite/CIGS	24.2 ± 0.7[h]	1.045 (da)	1.768	19.24[f]	72.9	FhG-ISE (1/20)	HZB, 2-terminal[49]
Perovskite/perovskite	26.4 ± 0.7[h]	1.044 (da)	2.118	15.22[e]	82.6	JET (3/22)	SichuanU/EMPA, 2-term.[50]
Perovskite/perovskite (minimodule)	**24.5 ± 0.6[h]**	**20.25 (da)**	**2.157**	**14.86[j]**	**77.5**	**JET (6/22)**	**Nanjing/ Renshine, 2-term.[51]**
a-Si/nc-Si/nc-Si (thin-film)	14.0 ± 0.4[j,c]	1.045 (da)	1.922	9.94[k]	73.4	AIST (5/16)	AIST, 2-term.[52]
a-Si/nc-Si (thin-film cell)	12.7 ± 0.4[j,c]	1.000 (da)	1.342	13.45[l]	70.2	AIST (10/14)	AIST, 2-term.[53]

Appendix IV: Site specific outdoor setup data

Appendix IV-1: Site 1 Output parameters

Site Visit	Irradiance (W/m^2)	Cell Temp (^oC)	Voc (stc) (V)	Voc (Raw) (V)	Isc (Stc) (A)	Isc (Raw) (A)	Impp (stc) (A)	Impp (Raw) (A)	Vmpp (stc) (V)	Vmpp (Raw) (V)	FF (stc)	FF (Raw)	Pmpp (stc) (W)	Pmpp (Raw) (W)	Voc (Raw) TMOT (V)	Vmpp (Raw) TMOT (V)	Isc (Norm.) (A)	Impp (Norm) (A)
1	1021	42.2	21.49	20.13	0.801	0.819	0.727	0.721	16.98	15.56	0.71	0.69	12.77	11.22	19.77	14.09	0.882	0.777
2	1036	43.5	21.31	19.89	0.799	0.827	0.725	0.751	17.06	16.21	0.72	0.71	12.4	12.17	19.59	14.68	0.878	0.797
3	1005	49.2	21.66	19.75	0.825	0.830	0.752	0.733	16.98	15.52	0.72	0.71	12.31	11.38	19.71	14.38	0.908	0.802
4	1002	37.8	20.66	19.66	0.819	0.820	0.737	0.738	16.74	15.75	0.71	0.70	12.29	11.62	19.11	14.55	0.900	0.810
5	956	36.5	20.77	19.81	0.831	0.794	0.734	0.701	17.62	16.23	0.72	0.71	12.18	11.38	19.19	14.92	0.914	0.807
6	1002	43.1	21.2	19.77	0.743	0.744	0.672	0.673	17.39	16.02	0.72	0.71	12.09	10.78	19.46	14.66	0.817	0.739
7	976	47.4	21.47	19.68	0.757	0.739	0.693	0.669	16.25	15.21	0.71	0.70	11.98	10.18	19.56	14.13	0.833	0.754
8	999	47.7	21.46	19.68	0.738	0.737	0.668	0.667	16.99	15.37	0.72	0.71	11.77	10.25	19.58	14.17	0.812	0.734
9	857	39.7	21.56	20.19	0.784	0.672	0.691	0.592	17.45	16.36	0.86	0.85	11.66	9.69	19.71	14.97	0.863	0.760
10	851	39.3	21.52	20.17	0.777	0.661	0.695	0.591	17.22	15.41	0.73	0.71	11.5	9.11	19.67	14.10	0.854	0.764
11	719	33.4	21.25	20.17	0.639	0.460	0.668	0.480	17.03	15.58	0.73	0.71	11.44	7.48	19.40	14.29	0.703	0.735
12	728	36.2	21.38	20.1	0.740	0.539	0.644	0.469	17.69	16.26	0.72	0.71	11.39	7.62	19.46	14.88	0.814	0.708
13	562	34.1	21.32	19.9	0.741	0.416	0.644	0.362	17.17	16.36	0.71	0.70	11.38	5.92	19.17	15.04	0.814	0.708
14	555	34.1	21.31	19.89	0.749	0.416	0.663	0.354	17.54	16.24	0.71	0.70	11.3	5.75	19.16	14.93	0.824	0.702

Appendix IV-2: Site 2 Output parameters

Site Visit	Irradiance (W/m^2)	Cell Temp (^oC)	Voc (stc) (V)	Voc (Raw) (V)	Isc (Stc) (A)	Isc (Raw) (A)	Impp (stc) (A)	Impp (Raw) (A)	Vmpp (stc) (V)	Vmpp (Raw) (V)	FF (stc)	FF (Raw)	Pmpp (stc) (W)	Pmpp (Raw) (W)	Voc (Raw) TMOT (V)	Vmpp (Raw) TMOT (V)	Isc (Norm.) (A)	Impp (Norm) (A)
1	1021	42.2	21.49	20.13	0.801	0.819	0.727	0.721	17.06	16.21	0.72	0.71	12.4	11.69	19.77	14.68	0.882	0.777
2	1036	43.5	21.31	19.89	0.799	0.827	0.725	0.751	16.98	15.52	0.72	0.71	12.31	11.66	19.59	14.06	0.878	0.797
3	1014	46.3	20.96	19.33	0.806	0.702	0.692	0.702	16.68	15.02	0.68	0.67	11.54	10.54	19.17	13.98	0.762	0.762
4	903	43.5	21.11	19.54	0.735	0.663	0.686	0.62	16.75	15.16	0.74	0.72	11.49	9.40	19.25	14.04	0.808	0.755
5	877	43.5	21.12	19.52	0.861	0.755	0.693	0.602	16.57	15.1	0.63	0.62	11.48	9.09	19.23	13.95	0.947	0.755
6	857	46.4	21.12	19.29	0.797	0.683	0.686	0.582	16.72	15.04	0.68	0.66	11.47	8.75	19.13	13.97	0.877	0.747
7	848	46.4	21.12	19.28	0.797	0.676	0.688	0.577	16.66	14.97	0.68	0.66	11.46	8.64	19.12	13.90	0.877	0.748
8	1087	51.3	21.46	19.5	0.706	0.767	0.66	0.717	16.79	14.81	0.73	0.71	11.08	10.62	19.56	13.69	0.776	0.726
9	1063	51.8	21.02	19.05	0.766	0.814	0.677	0.72	16.26	14.26	0.68	0.66	11.01	10.27	19.13	13.21	0.842	0.745
10	1050	51.8	20.93	18.95	0.761	0.799	0.687	0.721	16.02	14.01	0.69	0.67	11.01	10.10	19.03	12.98	0.837	0.755
11	1061	51.8	20.98	19.01	0.758	0.804	0.683	0.703	16.03	14.51	0.69	0.67	10.95	10.20	19.09	13.44	0.834	0.729
12	1201	42.8	21.39	20.17	0.627	0.753	0.627	0.753	17.1	15.86	0.73	0.71	10.72	11.94	19.84	14.69	0.690	0.690
13	1293	34.5	21.02	20.55	0.724	0.841	0.65	0.841	16.24	15.75	0.69	0.69	10.58	13.25	19.82	14.55	0.715	0.715
14	1216	52.6	21.34	19.43	0.612	0.744	0.462	0.562	18.51	16.57	0.65	0.64	8.55	9.31	19.55	15.27	0.673	0.508
15	1207	52.6	21.27	19.35	0.612	0.738	0.458	0.553	18.62	16.68	0.66	0.65	8.53	9.22	19.47	15.38	0.673	0.504

Appendix IV-3: Site 3 Output parameters

Site Visit	Irradiance (W/m^2)	Cell Temp (ºC)	Voc (stc) (V)	Voc (Raw) (V)	Isc (Stc) (A)	Isc (Raw) (A)	Impp (stc) (A)	Impp (Raw) (A)	Vmpp (stc) (V)	Vmpp (Raw) (V)	FF (stc)	FF (Raw)	Pmpp (stc) (W)	Pmpp (Raw) (W)	Voc (Raw) TMOT (V)	Vmpp (Raw) TMOT (V)	Isc (Norm.) (A)	Impp (Norm) (A)
1	692	34.8	21.51	20.27	0.978	0.677	0.785	0.543	16.13	14.87	0.60	0.59	12.66	8.07	19.56	13.47	1.076	0.863
2	695	34.8	21.38	20.15	0.980	0.682	0.801	0.539	15.61	14.85	0.60	0.58	12.50	8.00	19.45	13.45	1.079	0.853
3	1021	42.2	21.49	20.13	0.801	0.819	0.727	0.721	17.06	16.21	0.72	0.71	12.40	11.69	19.77	14.68	0.882	0.777
4	1036	43.5	21.31	19.89	0.799	0.827	0.725	0.751	16.98	15.52	0.72	0.71	12.31	11.66	19.59	14.06	0.878	0.797
5	1170	45.3	21.31	19.89	0.779	0.910	0.647	0.732	15.09	14.11	0.59	0.57	9.76	10.33	19.67	12.81	0.856	0.688
6	1111	45.3	21.03	19.56	0.777	0.863	0.638	0.681	15.16	14.26	0.59	0.57	9.67	9.71	19.35	12.92	0.854	0.674
7	1132	45.3	20.92	19.48	0.777	0.880	0.635	0.697	15.02	14.01	0.59	0.57	9.54	9.76	19.27	12.72	0.855	0.677
8	1187	43.6	21.02	19.75	0.768	0.912	0.634	0.752	15.04	13.75	0.59	0.57	9.54	10.34	19.46	12.49	0.845	0.697
9	579	35.1	21.32	19.87	0.677	0.392	0.449	0.260	17.48	16.02	0.54	0.53	7.85	4.16	19.19	14.47	0.745	0.494
10	582	36.2	21.20	19.68	0.680	0.396	0.447	0.260	17.35	15.82	0.54	0.53	7.76	4.12	19.06	14.26	0.749	0.492
11	1019	42.6	21.28	19.90	0.628	0.640	0.455	0.464	17.01	15.62	0.58	0.57	7.74	7.25	19.56	14.11	0.691	0.501
12	1023	42.7	21.20	19.83	0.626	0.640	0.449	0.460	17.20	15.81	0.58	0.57	7.72	7.26	19.50	14.28	0.688	0.494

Appendix 1V-4: Site 4 Output parameters

Site Visit	Irradiance (W/m^2)	Cell Temp (°C)	Voc (stc) (V)	Voc (Raw) (V)	Isc (Stc) (A)	Isc (Raw) (A)	Impp (stc) (A)	Impp (Raw) (A)	Vmpp (stc) (V)	Vmpp (Raw) (V)	FF (stc)	FF (Raw)	Pmpp (stc) (W)	Pmpp (Raw) (W)	Voc (Raw) TMOT (V)	Vmpp (Raw) TMOT (V)	Isc (Norm.) (A)	Impp (Norm) (A)
1	1011	52.9	21.41	19.28	0.777	0.785	0.67	0.67	17.22	15.06	0.69	0.67	11.5	10.14	19.41	13.64	0.854	0.732
2	1012	43.0	20.92	19.52	0.793	0.803	0.68	0.68	16.69	15.27	0.68	0.67	11.3	10.44	19.21	13.97	0.873	0.743
3	866	38.4	21.67	20.40	0.800	0.693	0.46	0.40	19.72	18.44	0.52	0.52	9.09	7.36	19.86	16.49	0.880	0.507
4	968	45.2	21.49	19.87	0.752	0.743	0.45	0.45	19.16	17.52	0.54	0.53	8.70	7.86	19.65	15.67	0.844	0.510
5	582	32.5	21.45	20.19	0.759	0.442	0.54	0.30	16.18	15.52	0.53	0.52	8.70	4.67	19.38	13.95	0.835	0.569
6	788	32.2	21.28	20.40	0.776	0.611	0.45	0.35	19.00	18.11	0.52	0.51	8.55	6.42	19.56	16.28	0.853	0.495
7	1005	44.0	21.41	19.90	0.700	0.703	0.43	0.43	19.14	17.62	0.55	0.54	8.19	7.57	19.63	16.08	0.769	0.470
8	1005	42.9	21.30	19.89	0.700	0.704	0.43	0.43	19.03	17.60	0.55	0.54	8.14	7.56	19.57	16.10	0.771	0.470
9	1297	33.7	20.95	20.55	0.686	0.890	0.43	0.56	18.36	17.94	0.55	0.54	7.86	9.96	19.78	16.12	0.755	0.471
10	1015	45.6	21.07	19.48	0.674	0.684	0.41	0.42	18.78	17.18	0.55	0.54	7.77	7.21	19.28	15.52	0.741	0.455
11	1000	41.7	21.54	20.19	0.676	0.676	0.40	0.39	19.11	18.17	0.53	0.52	7.68	7.13	19.80	16.29	0.744	0.432

Appendix IV-5: Site 5 Output parameters

Site Visit	Irradiance (W/m^2)	Cell Temp (ºC)	Voc (stc) (V)	Voc (Raw) (V)	Isc (Stc) (A)	Isc (Raw) (A)	Impp (stc) (A)	Impp (Raw) (A)	Vmpp (stc) (V)	Vmpp (Raw) (V)	FF (stc)	FF (Raw)	Pmpp (stc) (W)	Pmpp (Raw) (W)	Voc (Raw) TMOT (V)	Vmpp (Raw) TMOT (V)	Isc (Norm.) (A)	Impp (Norm) (A)
1	1177	36.0	20.78	20.10	0.812	0.955	0.695	0.818	16.87	16.15	0.69	0.69	11.72	13.21	19.45	14.59	0.893	0.764
2	1011	52.9	21.41	19.28	0.777	0.785	0.666	0.673	17.22	15.06	0.69	0.67	11.47	10.14	19.41	13.64	0.854	0.732
3	1055	30.8	20.48	20.08	0.735	0.775	0.652	0.688	16.63	16.21	0.72	0.72	10.84	11.15	19.19	14.46	0.808	0.717
4	1148	42.3	21.08	19.87	0.795	0.914	0.688	0.766	16.66	15.90	0.68	0.67	11.46	12.18	19.52	14.18	0.876	0.734
5	1150	41.3	21.40	20.25	0.756	0.870	0.669	0.770	17.31	16.13	0.72	0.71	11.58	12.42	19.84	14.35	0.832	0.737
6	1022	51.4	21.54	19.50	0.679	0.694	0.587	0.600	17.88	15.82	0.72	0.70	10.50	9.49	19.56	14.15	0.747	0.646
7	1019	49.0	21.65	19.77	0.686	0.611	0.613	0.611	17.36	15.82	0.72	0.70	10.64	9.67	19.72	14.18	0.660	0.660
8	1198	39.1	20.41	19.52	0.793	0.950	0.637	0.763	16.82	15.90	0.66	0.65	10.71	12.13	19.03	14.40	0.872	0.701
9	1211	43.2	21.47	20.23	0.702	0.850	0.704	0.852	17.25	15.98	0.81	0.79	12.14	13.61	19.91	14.33	0.772	0.774
10	907	43.2	21.53	19.96	0.765	0.694	0.731	0.634	16.73	15.88	0.74	0.73	12.23	10.07	19.65	14.24	0.842	0.769
11	1101	41.8	21.41	20.17	0.819	0.901	0.649	0.714	17.26	16.00	0.64	0.63	11.20	11.42	19.79	14.34	0.900	0.713

Appendix V: Average ambient conditions and dust deposition rates

Appendix V-1: Average wind speeds and humidity at the study sites

	Average Humidity (%)						**Average Wind speed (m/s)**						**Wind direction (º)**
Site	Sep. 2020	Oct. 2020	Nov. 2020	Dec. 2020	Jan. 2021	Feb. 2021	Sep. 2020	Oct. 2020	Nov. 2020	Dec. 2020	Jan. 2021	Feb. 2021	
1	57.04	54.6	71.09	66.67	59.64	56.79	3.38	3.68	3.68	3.6	3.67	3.04	132.84
2	57.36	55.1	71.48	67.15	60.12	56.89	3.35	3.46	3.27	3.15	3.25	2.7	136.02
3	58.08	55.42	71.34	66.35	59.83	56.11	3.05	2.88	2.65	2.5	2.63	2.26	147.88
4	57.79	55.18	71.65	67.16	60.32	57.05	3.21	3.39	3.4	3.28	3.36	2.82	137.16
5	57.99	55.29	71.79	67.26	60.49	57.13	3.17	3.33	3.38	3.24	3.32	2.81	138.12

Appendix V-2: Average dust deposition rate and average rainfall at the study sites

	Average dust deposition rate (g/m^2)						**Average Rainfall (mm)**					
Site	Sep. 2020	Oct. 2020	Nov. 2020	Dec. 2020	Jan. 2021	Feb. 2021	Sep. 2020	Oct. 2020	Nov. 2020	Dec. 2020	Jan. 2021	Feb. 2021
1	16.16	15.36	14.4	12.48	15.04	16.48	71.00	40.74	146.98	62.62	57.84	89.45
2	19.36	17.76	15.52	13.28	15.68	19.52	64.74	40.39	158.72	68.71	53.23	70.46
3	24.32	22.24	19.04	17.6	19.52	24.48	70.65	36.21	156.78	57.08	44.97	46.16
4	21.12	21.6	17.92	16.32	18.24	21.76	80.61	44.50	157.96	61.87	56.89	85.69
5	17.44	16.8	15.2	12.8	15.2	17.6	85.08	45.97	159.94	60.68	57.41	87.81

Appendix VI: Dust elements concentration

Appendix VI-1: Dust elements concentration by mass (g/kg)

Site	Na	Mg	Al	P	S	K	Ca	Ti	Cr	Mn	Fe	Co	Ni	Cu	Zn	Pb	SOC	Total N
1	1689.5	3911	46374.5	1107	456	7058	4580.5	850.5	33	932.5	33415	8	28.5	46	309	0	0.12	0.01
2	647	5325.5	62488.5	848	535	7431.5	7015.5	685.5	57.5	2061.5	62150.5	7	48	37.5	339	0	0.51	0.01
3	876.5	4015	55289	1816.5	456.5	5668.5	10848	1151	53	2260	61506.5	7	42	35	299	0	0.11	0.01
4	1065	2922	45582.5	620	407	7240.5	5137.5	1378	153	11040	104907.5	7	113.5	253	20436	262.5	0.98	0.04
5	808	3538.5	57433	808	353	6357	8628.5	1276.5	66	3330.5	62832.5	7	46.5	10	289	0	0.9	0.03
Mean	1017.2	3942.4	53433.5	1039.9	441.5	6751.1	7242	1068.3	72.5	3924.9	64962.4	7.2	55.7	76.3	4334.4	52.5	0.524	0.02
S.dev	361.9	790.4	6525.3	418.2	60.3	651.8	2301.7	260.8	41.7	3638	22870.2	0.4	29.7	89.2	8050.8	105	0.4	0

Appendix VI-2: Dust elements concentration by volume (cm^3/kg)

Site	Na	Mg	Al	P	S	K	Ca	Ti	Cr	Mn	Fe	Co	Ni	Cu	Zn	Pb
1	1.742	2.250	17.176	0.608	0.221	7.930	2.974	0.189	0.005	0.128	4.243	0.001	0.003	0.005	0.043	0.000
2	0.667	3.064	23.144	0.466	0.259	8.350	4.556	0.152	0.008	0.282	7.892	0.001	0.005	0.004	0.048	0.000
3	0.904	2.310	20.477	0.998	0.221	6.369	7.044	0.256	0.007	0.310	7.810	0.001	0.005	0.004	0.042	0.000
4	1.098	1.681	16.882	0.341	0.197	8.135	3.336	0.306	0.021	1.512	13.322	0.001	0.013	0.028	2.865	0.023
5	0.833	2.036	21.271	0.444	0.171	7.143	5.603	0.284	0.009	0.456	7.979	0.001	0.005	0.001	0.041	0.000

Appendix VII: Dust deposition rates at varying height, tilt angle and orientation in southerly winds.

Slide no.	Length (cm)	Width (cm)	Area (cm^2)	Installation Height (m)	Tilt angle (^oC)	Orientation	Subsequent masses of glass slides (g)							
							24-Feb 2022	3-Mar 2022	10-Mar 2022	17-Mar 2022	25-Mar-2022	31-Mar-2022	1-Jun-2022	23-Jun 2022
1	15.7	6.9	108.33	2.5	15	South	12.20	12.22	12.25	12.28	12.35	12.21	12.28	12.27
2	15.7	6.9	108.33	2.5	5	South	12.40	12.44	12.46	12.48	12.5	12.41	12.54	12.56
3	15.7	6.9	108.33	2.5	10	South	12.40	12.45	12.47	12.47	12.5	12.42	12.5	12.53
4	15.7	6.9	108.33	2.5	15	North	12.50	12.51	12.53	12.58	12.58	12.52	12.57	12.58
5	15.7	6.9	108.33	2.5	5	North	12.70	12.77	12.78	12.8	12.78	12.73	12.85	12.88
6	15.7	6.9	108.33	2.5	10	North	12.30	12.34	12.36	12.38	12.4	12.32	12.44	12.38
7	15.7	6.9	108.33	2	15	South	12.50	12.54	12.55	12.56	12.57	12.52	12.58	12.58
8	15.7	6.9	108.33	2	5	South	12.50	12.54	12.56	12.58	12.6	12.51	12.6	12.68
9	15.7	6.9	108.33	2	10	South	13.40	13.48	13.48	13.47	13.5	13.41	13.56	13.56
10	15.7	6.9	108.33	2	15	North	13.20	13.26	13.27	13.29	13.3	13.21	13.38	13.38
11	15.7	6.9	108.33	2	5	North	13.00	13.14	13.15	13.16	13.18	13.01	13.1	13.18
12	15.7	6.9	108.33	2	10	North	13.30	13.36	13.36	13.38	13.38	13.31	13.39	13.4
13	15.7	6.9	108.33	1.5	15	South	13.70	13.76	13.78	13.82	13.88	13.71	13.88	13.8
14	15.7	6.9	108.33	1.5	5	South	13.10	13.18	13.18	13.16	13.2	13.12	13.16	13.1
15	15.7	6.9	108.33	1.5	10	South	13.87	13.88	13.96	13.98	13.93	13.88	13.96	13.98
16	15.7	6.9	108.33	1.5	10	North	13.80	13.86	13.88	13.9	13.86	13.82	13.87	13.88
17	15.7	6.9	108.33	1.5	5	North	13.00	13.1	13.12	13.14	13.18	13.06	13.16	13.18
18	15.7	6.9	108.33	1.5	15	North	13.10	13.16	13.18	13.22	13.28	13.18	13.24	13.26

Appendix VIII: Self-cleaning model data

Appendix VIII-1: Generated fluid velocities

Time (s)	**Fluid Velocities (m/s)**									**Generated forces as a factor of the square of the dust particles radius (R^2)(N/m^2)**					
	Fun A	Fun B	Fun C	Water Jet A	Water Jet B	Avg. spray	Air	Avg. spray	Water	Fd/R^2 (Water)	FL/R^2 (Water)	Fd/R^2 (Air)	FL/R^2 (Air)	Fd/R^2	FL/R^2
1	11.62	14.80	13.67	4.71	4.12	13.36		4.414		5.755	4.530	0.058	0.241	5.812	4.772
2	11.70	14.62	13.76	4.87	4.16	13.36		4.517		6.026	4.744	0.058	0.241	6.084	4.985
3	11.62	14.74	13.95	5.44	4.36	13.44		4.903		7.102	5.591	0.058	0.244	7.160	5.835
4	12.00	14.56	13.64	4.89	4.03	13.40		4.462		5.882	4.630	0.058	0.243	5.940	4.873
5	11.72	14.68	13.78	4.61	4.35	13.39		4.483		5.937	4.674	0.058	0.242	5.995	4.916
6	11.77	14.63	13.70	4.02	4.14	13.37		4.083		4.924	3.876	0.058	0.241	4.982	4.118
7	11.55	14.64	13.75	4.57	4.52	13.31		4.546		6.104	4.805	0.057	0.240	6.161	5.045
8	11.70	14.62	13.70	4.69	4.90	13.34		4.793		6.787	5.343	0.058	0.240	6.844	5.583
9	11.32	14.14	13.81	3.15	4.65	13.09		3.897		4.485	3.531	0.055	0.232	4.541	3.763
10	11.49	14.25	13.73	4.84	4.47	13.16		4.653		6.395	5.034	0.056	0.234	6.451	5.268
11	10.80	14.32	14.03	3.12	4.49	13.05		3.807		4.281	3.370	0.055	0.230	4.336	3.600
12	11.13	14.44	14.04	3.83	4.36	13.20		4.097		4.958	3.903	0.056	0.236	5.014	4.138
13	11.28	14.37	14.49	4.17	3.87	13.38		4.019		4.771	3.756	0.058	0.242	4.829	3.998
14	11.32	14.63	14.38	3.67	3.07	13.44		3.369		3.353	2.640	0.058	0.244	3.412	2.884
15	11.24	14.79	14.32	3.44	4.36	13.45		3.896		4.484	3.530	0.059	0.244	4.543	3.775
16	11.00	14.41	13.96	3.69	4.27	13.12		3.982		4.683	3.687	0.056	0.233	4.739	3.920
17	10.12	14.56	14.19	3.62	4.41	12.96		4.016		4.765	3.751	0.054	0.227	4.819	3.978
18	11.32	14.54	14.18	3.71	4.10	13.35		3.906		4.506	3.547	0.058	0.241	4.564	3.788
19	11.39	14.41	14.26	4.02	4.24	13.35		4.131		5.042	3.969	0.058	0.241	5.099	4.210
Time (s)	**Fluid Velocities (m/s)**									**Generated forces as a factor of the square of the dust particles radius (R^2)(N/m^2)**					
	Fun	Fun	Fun	Water Jet	Water Jet	Avg.	Air	Avg.	Water	Fd/R^2 (Water)	FL/R^2	Fd/R^2	FL/R^2 (Air)	Fd/R^2	FL/R^2

	A	B	C	A	B	spray	spray		(Water)	(Air)			
20	11.29	14.27	14.33	3.99	4.29	13.30	4.137	5.056	3.980	0.057	0.239	5.113	4.219
21	11.44	14.45	14.42	4.10	4.03	13.44	4.067	4.885	3.846	0.058	0.244	4.944	4.090
22	11.19	14.20	14.15	4.22	3.66	13.18	3.940	4.586	3.610	0.056	0.235	4.642	3.845
23	11.65	14.21	14.40	3.63	3.54	13.42	3.583	3.793	2.986	0.058	0.243	3.851	3.229
24	11.52	14.43	14.19	4.09	3.38	13.38	3.737	4.126	3.248	0.058	0.242	4.184	3.490
25	10.86	14.22	14.49	3.85	3.22	13.19	3.535	3.691	2.905	0.056	0.235	3.747	3.141
26	11.28	13.94	14.40	3.89	3.95	13.21	3.920	4.539	3.573	0.056	0.236	4.595	3.809
27	11.58	13.03	14.20	3.50	3.66	12.94	3.580	3.785	2.980	0.054	0.226	3.839	3.206
28	11.57	14.37	14.12	3.17	3.70	13.35	3.435	3.485	2.743	0.058	0.241	3.542	2.984
29	11.41	14.19	14.18	3.28	3.41	13.26	3.346	3.307	2.603	0.057	0.238	3.363	2.841
30	11.29	14.53	14.42	3.28	3.45	13.41	3.364	3.343	2.632	0.058	0.243	3.401	2.875
31	11.13	14.52	14.37	3.14	3.56	13.34	3.349	3.312	2.608	0.058	0.240	3.370	2.848
32	11.47	14.32	14.38	3.13	3.62	13.39	3.374	3.363	2.648	0.058	0.242	3.421	2.890
33	11.46	13.97	14.21	3.11	3.59	13.21	3.348	3.311	2.607	0.056	0.236	3.368	2.843
34	11.47	13.39	14.29	3.43	3.94	13.05	3.682	4.005	3.153	0.055	0.230	4.060	3.383
35	11.55	13.87	13.92	3.61	3.75	13.11	3.678	3.996	3.146	0.056	0.232	4.052	3.379
36	11.37	13.29	14.02	3.68	3.67	12.89	3.674	3.988	3.139	0.054	0.225	4.042	3.364
37	11.40	14.21	14.03	3.19	3.59	13.21	3.390	3.395	2.673	0.056	0.236	3.452	2.909
38	11.15	14.10	13.92	3.28	3.51	13.06	3.393	3.401	2.677	0.055	0.230	3.456	2.908
39	11.13	14.39	13.90	3.23	3.59	13.14	3.408	3.430	2.700	0.056	0.233	3.486	2.934
40	10.49	14.52	14.21	3.31	3.41	13.07	3.359	3.332	2.623	0.055	0.231	3.388	2.854
41	10.46	14.42	14.13	3.58	3.83	13.00	3.703	4.051	3.189	0.055	0.228	4.106	3.418

Time (s)	Fluid Velocities (m/s)							Generated forces as a factor of the square of the dust particles radius (R^2)(N/m^2)					
	Fun A	Fun B	Fun C	Water Jet A	Water Jet B	Avg. Air spray	Avg. Water spray	F_d/R^2 (Water)	F_L/R^2 (Water)	F_d/R^2 (Air)	F_L/R^2 (Air)	F_d/R^2	F_L/R^2
42	10.46	14.32	14.08	3.25	3.67	12.95	3.459	3.534	2.782	0.054	0.227	3.588	3.009
43	10.64	14.29	13.87	3.54	3.77	12.93	3.652	3.939	3.101	0.054	0.226	3.993	3.327
44	10.87	14.33	14.07	3.25	3.68	13.09	3.463	3.543	2.789	0.055	0.232	3.598	3.021
45	10.43	14.26	14.12	3.26	3.87	12.94	3.566	3.757	2.957	0.054	0.226	3.811	3.184
46	10.50	14.38	14.20	4.23	3.88	13.03	4.053	4.852	3.819	0.055	0.229	4.907	4.049
47	10.93	14.43	14.25	4.26	3.45	13.20	3.859	4.398	3.463	0.056	0.236	4.455	3.698
48	11.20	14.46	14.17	4.31	3.46	13.28	3.886	4.460	3.511	0.057	0.238	4.517	3.749
49	11.51	14.22	14.15	4.31	3.57	13.29	3.937	4.578	3.604	0.057	0.239	4.635	3.843
50	11.34	14.42	14.12	4.57	3.64	13.29	4.102	4.971	3.913	0.057	0.239	5.028	4.152
Avg.	**11.24**	**14.32**	**14.10**	**3.83**	**3.88**	**13.22**	**3.86**	**4.449**	**3.502**	**0.057**	**0.236**	**4.506**	**3.739**

NB: F_d – Drag force; F_L – Lift force; R- Radius of dust particles

Appendix VIII-2: Particulate radius, associated fluid velocities and Lift and drag forces

Particle size (R) (m)	Required fluid velocities for fluid resuspension (m/s)					Required Forces (N)		Particulate Adhesive Force (N)	Generated Forces (N)		Resultant Forces (N)		
	Site 1	Site 2	Site 3	Site 4	Site 5	F Drag	F lift		F Drag	F lift	Fgrav	F Drag	F lift
10	71.5	66.2	83.7	88.8	105.7	0.036	0.151	0.155	0.045	0.037	0.000	0.045	0.037
20	50.6	46.8	59.2	62.8	74.8	0.072	0.302	0.311	0.180	0.150	0.004	0.176	0.146
30	41.3	38.2	48.3	51.3	61.0	0.108	0.453	0.465	0.406	0.337	0.013	0.393	0.323
40	35.8	33.1	41.9	44.4	52.9	0.145	0.605	0.622	0.722	0.598	0.031	0.690	0.567
50	32.0	30.0	37.4	39.7	47.3	0.181	0.756	0.777	1.128	0.935	0.061	1.066	0.874
60	29.2	27.0	34.2	36.3	43.2	0.217	0.908	0.934	1.624	1.346	0.106	1.518	1.241
70	27.0	25.0	31.6	33.6	40.0	0.254	1.059	1.089	2.210	1.833	0.168	2.042	1.665
80	25.3	23.4	29.6	31.4	37.4	0.290	1.210	1.244	2.886	2.394	0.250	2.636	2.143
90	23.8	22.1	27.9	29.6	35.2	0.325	1.356	1.395	3.653	3.029	0.356	3.297	2.673
100	22.6	20.9	26.5	28.1	33.4	0.361	1.508	1.550	4.510	3.740	0.489	4.021	3.251
150	18.5	17.0	21.6	22.9	27.3	0.542	2.266	2.330	10.148	8.415	1.650	8.497	6.765
200	16.0	14.8	18.7	19.9	23.6	0.720	3.011	3.096	18.040	14.960	3.911	14.129	11.049
250	14.3	13.2	16.7	17.8	21.1	0.900	3.760	3.866	28.188	23.375	7.639	20.548	15.736
300	13.2	12.1	15.3	16.2	19.3	1.084	4.530	4.658	40.590	33.660	13.200	27.390	20.460
350	12.1	11.2	14.2	15.0	17.9	1.269	5.304	5.454	55.248	45.815	20.962	34.286	24.853
400	11.3	10.5	13.2	14.0	16.7	1.443	6.030	6.200	72.160	59.840	31.290	40.870	28.550
450	10.7	9.9	12.5	13.2	15.8	1.635	6.831	7.024	91.328	75.735	44.551	46.777	31.184
500	10.1	9.4	11.8	12.6	15.0	1.819	7.601	7.816	112.750	93.500	61.112	51.638	32.388

Appendix VIII-3: Solar P-V module I-V data under the action of the automated self –cleaning model

Pre-exposure to dust		**Dusty Module**		**Cleaned module**	
Voltage, V (V)	Current, I (A)	Voltage, V (V)	Current, I (A)	Voltage, V (V)	Current, I (A)
0.00	1.727	0.00	0.2454	0.00	1.7820
1.00	1.727	1.00	0.2454	1.00	1.7820
2.00	1.727	2.00	0.2454	1.50	1.7820
3.00	1.727	2.50	0.2454	2.00	1.7820
4.00	1.727	3.00	0.2454	3.00	1.7820
5.00	1.725	4.00	0.2454	3.50	1.7820
6.00	1.725	5.00	0.2454	4.00	1.7820
7.00	1.720	5.50	0.2450	4.50	1.7820
7.50	1.720	6.00	0.2350	5.00	1.7820
8.00	1.720	6.50	0.2310	6.00	1.7820
9.00	1.715	7.00	0.2250	8.00	1.7650
10.00	1.710	7.50	0.2225	9.50	1.7550
11.00	1.705	8.00	0.2200	10.00	1.7500
12.00	1.703	8.50	0.2150	11.00	1.7490
13.00	1.700	9.00	0.2160	11.50	1.7485
13.50	1.695	10.00	0.2167	12.00	1.7480
14.00	1.680	11.00	0.2160	13.00	1.7450
15.00	1.640	11.50	0.2100	14.00	1.7370
15.50	1.600	12.00	0.2063	15.00	1.7330
15.81	1.583	13.00	0.2000	16.95	1.6420
16.20	1.550	14.00	0.1875	17.40	1.6200
16.40	1.500	15.00	0.1833	17.90	1.5000
17.00	1.400	16.00	0.1750	18.50	1.3350
17.30	1.350	16.50	0.1700	19.00	1.1400
17.50	1.290	17.50	0.1670	19.40	1.0000
18.30	1.050	18.00	0.1625	20.00	0.7500

19.00	0.780	18.05	0.1651	21.00	0.1500
19.60	0.500	18.50	0.1500	21.16	0.0000
20.00	0.270	18.75	0.1000		

2.5